Федеральное государственное автономное образовательное учреждение
высшего образования «Уральский федеральный университет
имени первого Президента России Б.Н. Ельцина»

Физико-технологический институт

Кафедра физических методов и приборов контроля качества

Научно-исследовательская лаборатория "Физика функциональных
материалов углеродной микро- и оптоэлектроники

На правах рукописи

Лэй Сюе

МОДЕЛИРОВАНИЕ ВЛИЯНИЯ МОДИФИКАЦИИ СТРУКТУРЫ НИЗКОРАЗМЕРНЫХ МАТЕРИАЛОВ ZnO, β-C_3N_4, InSe и ОДНОСЛОЙНОГО БОРА НА ИХ ФИЗИЧЕСКИЕ СВОЙСТВА

01.04.07 – Физика конденсированного состояния

Диссертация на соискание ученой степени кандидата
физико-математических наук

Научный руководитель
Кандидат технических наук, доцент,
Зацепин Анатолий Федорович

Екатеринбург – 2020

Federal State Autonomous Educational Institution of Higher Education «Ural Federal University
named after the first President of Russia B.N. Yeltsin»
Institute of Physics and Technology
Department of physical methods and quality control devices
Research laboratory "Physics of functional materials of carbon micro- and optoelectronics

As a manuscript

Lei Xue

MODELING THE INFLUENCE OF STRUCTURE MODIFICATION OF LOW-SIZE ZnO, β-C_3N_4, InSe AND SINGLE-LAYER BORON ON THEIR PHYSICAL PROPERTIES

01.04.07 – Condensed matter physics

Dissertation for the degree of candidate of
physical and mathematical sciences

Supervisor
Candidate of Technical Sciences,
Associate Professor,
Zatsepin Anatoly Fedorovich

Yekaterinburg – 2020

TABLE OF CONTENTS

INTRODUCTION

Relevance of the topic. Low-dimensional materials (two-dimensional, one-dimensional and zero-dimensional systems) are at the peak of research in the field of materials science, physics and chemistry. These materials are already finding their first application in various industries such as electronics, energy (batteries, solar panels), chemical technology (catalysis). It also discusses many potential applications for low-dimensional materials ranging from the purification and desalination of water and up to use in medicine (drug delivery). The optical properties of low-dimensional systems are also intensively studied by modern science. The main areas of application of the optical properties of low-dimensional systems under consideration are photochemistry and luminescence. In prototypes of photochemical catalysts, low-dimensional semiconductors generate an electron-hole pair, which is then used for the electrochemical reaction occurring on the metal part of the hybrid system. In the luminescence region, low-dimensional semiconductors emit a photon due to the recombination of an electron-hole pair induced by an electric field. If the adsorption of molecules changes the luminescent properties of the material, then such a material can be used as a sensor. A systematic study, through modeling from first principles, of the effect of the modification of low-dimensional systems on their electronic structure and optical properties is the subject of a dissertation.

One of the main features of low-dimensional systems is the significant contribution of the surface to all the properties of the material. If the electrical, optical and magnetic properties of three-dimensional systems can be considered by the model of an infinite periodic system, while neglecting the contribution of the surface and the environment. In low-dimensional systems the contribution from the surface and the influence of doping of near-surface regions, the shape and defects of the surface, and changes in the surface structure after modification should be taken into account and the contribution from the adsorption of molecules on the surface is inevitable. To study these effects, the most prominent representatives of various classes of low-dimensional materials are considered: ZnO, β-C_3N_4, InSe and borophene. Zinc oxide usually forms large nanoparticles with a structure identical or close to the structure of the array and therefore a small contribution of the surface to physical properties. Carbon nitride forms nanoparticles with an atomic structure close to the array, but with a large contribution from the surface due to the small size of the nanoparticles. Indium selenide (InSe) represents a system of layers connected by weak non-covalent bonds (such systems are called “van der Waals” in modern literature)[1-3], which are easily melted to form a single-layer membrane (that is, that is, we can say that the material consists of one surface). A single-layer boron membrane (borophene), the various allotropes of which have an atomic structure different from boron crystals, and which, unlike the other systems studied, is a conductor. Such a choice of objects of study allows us to study the relationships between the physical and chemical properties of nanomaterials systematically, since the study covers the most common morphological types of low-dimensional materials-large and small nanoparticles, van der Waals systems, conductors and semiconductors.

The main physical property of the materials under study is a change in which with changes in the atomic structure we will investigate will be their photoactivity. There are two main ways to increase the efficiency of photoactive materials. The first method is doping, the second is chemical modification of the surface. Both of these approaches were studied in the course of the work performed. Zinc oxide was chosen as an object for studying the effect of doping on the optical properties of low-dimensional systems, which is considered as a promising material for multiple applications, such as photoelectronics and photochemistry. [4-7] Beryllium was chosen as a dopant for ZnO, which, unlike transition metal impurities, is not prone to clustering in the zinc oxide matrix. [8] Due to the low dimensionality and the large contribution of the surface in nanosystems, it is not always possible to draw a clear line between doping and surface modification. Therefore, most of our work is devoted to this topic. One of the phases of carbon nitride (β-C_3N_4) was chosen to study the effect of surface formation, its chemical modification and photoactive defects. Unlike layered materials such as indium selenide (InSe) or materials with a chemically neutral surface, such as ZnO, the surface of β-C_3N_4 contains chemically active centers. These centers were identified and simulated for their effect on the optical properties of carbon nitride before and after modification by means of hydrogen, oxygen and fluorine. Another way to manipulate optical properties is to mechanically distort the crystal structure. The most famous example of this phenomenon is mechanoluminescence. In low-dimensional systems, such a mechanical action is often unavoidable due to distortion of two-dimensional membranes under the influence of temperature or substrate. To study this phenomenon, we chose one of the most promising materials for nanoelectronics and photochemistry - indium selenide (InSe). This material combines the high mobility of charge carriers, suitable optical properties with the flexibility of single layers. The effect of distortions of a single-layer membrane on the adsorption of molecules and optical properties was considered in our work. Also, using the example of this material, another phenomenon unique to nanosystems was studied - molecular doping, which is realized through the exchange of charge between the surface and molecules adsorbed on it. For a single-layer boron membrane, it was shown that after inevitable oxidation, it turns from a metal into a semiconductor whose optical properties are sensitive to the adsorption of molecules. In other words, another method of manipulating the optical properties of nanomaterials can be implemented in this system.

Another physical property that will be investigated in our work is the so-called d0 magnetism. Many nanomaterials not containing transition metal ions exhibit paramagnetism, and often ferromagnetism in the absence of transition metal ions. As shown in many works devoted to this problem, such magnetism is unstable from a chemical point of view. The search for materials with d0 magnetism stable to chemical influences is an important task not only from an applied, but also from a scientific point of view. As a result of studies carried out in the course of the work, various variants of the implementation of chemically stable d0 magnetism on the modified surface of carbon nitride, in oxidized boron membranes, and in non-covalently modified indium selenide were shown.

Thus, the fundamental scientific problem is the lack of systematic knowledge about the relationship between the features of the atomic structure of a surface, its chemical stability and the optical and magnetic properties of materials, which complicates further progress in the development of new nanomaterials for optical and magnetic applications. The result of this state of affairs is the absence of a clear protocol for modeling nanosystems, which, on the one hand, leads to the fact that modeling of nanosystems sometimes turns out to be redundant and does not provide new information, but more often than not it is insufficient when some of the important properties are unexplored. Our work is a step towards the creation of a protocol guiding the systematic theoretical study of the physical properties of nanomaterials.

The degree of development of the research topic. With the development of faster computing capability and sophisticated computer programs, materials simulation is a very important method for scientists and engineers, ideally and theoretically, the different size of materials can be modeled from first principles. It is well known that almost all matter is made up of materials, so the design and optimization of materials are eternal problems, however, the emerging nanotechnology which changes the distribution and arrangement of atoms to obtain different properties of materials has brought significant changes in the design of materials [9]. Nowadays the nanotechnology has been widely used in energy, medical, aerospace and other fields. [10,11] Computer modeling of nanomaterials can describe the correlation between the material’s microstructure and its macroscopic properties quantitatively. The research is optimizing the design of the material structure through modeling in nanoscale, then calculate the energy of nanomaterials to assist researching on nanomaterials’ structure and properties.

Nanotechnology is becoming one of the main driving forces for the economic development of countries around the world. It is widely used in the fields of information, energy, environmental protection, biotechnology and medicine, various industries, national defense, etc., which leads to new technological changes, promotes the transformation and modernization of traditional industries, and forms a new industry based on nanotechnology. In the field of information, nanodevices, which play a key role in next-generation microcircuits, display and memory devices, which play a key role in the competitiveness of the future information industry. In the field of energy, nanotechnology can be used in new efficient and alternative energy sources and storage (such as lithium-ion batteries, solar cells, fuel cells, hydrogen) and key technologies for efficient use of energy. [12, 13] In the field of environmental protection, nanotechnology can be used to control water, air and soil pollution that were previously difficult to control. [14, 15] In biomedicine, nanotechnology can be used to develop technologies for early diagnosis of diseases. Rapid, low-cost testing of major diseases such as AIDS, hepatitis, tissue and organ repair and low-toxic high-efficiency treatment technologies. [16-18]

Currently, there are many software products for modeling the structure and properties of existing and hypothetical materials. Materials Studio is a relative mature modeling and simulation software for nanomaterials. Nanomaterials can be modeled and their physical properties can be calculated with this software. Recently some researchers use GPU (Graphics Processing Unit) to accelerate the modeling and simulation for nanomaterials. [19] This work is a simulation of nanosystems and a description of their resistance to the environment. Zinc oxide has a polar surface that can form a wide range of nanostructures, in the one-dimensional oxide nano-systems, it is one of the most promising materials for fabrication optoelectronic devices, the nanostructure of zinc oxide has high catalytic efficiency and strong adsorption ability. The electronic structures and optical properties of beryllium doped zinc oxide have been calculated using this software, we recognized that doping can improve the efficiency of photoactive materials, beryllium doped zinc oxide can be used in ultraviolet photoelectric equipment. For the modelling of carbonitride, we use density functional theory-based methods realized in the plane-wave pseudopotential approach in the Cambridge Sequential Total Energy Package codes. In the early research, under the local density approximation by using first pseudopotential band method, the theory predicts that the hardness of C_3N_4 can be comparable to diamond, after the theoretical prediction, the experimenters have the opportunity to use various methods for the directed synthesis of this new covalent compound of high hardness in the laboratory. Various approaches have been developed, such as synthesis of chemical vapor deposition [20,21], synthesis of vapor deposition [22,23], synthesis at high temperature and high pressure [24]. But in the preparation of a carbon-nitrogen film, an amorphous film is obtained in most cases, and it is difficult to obtain a film of a single crystal phase. Due to the serious loss of nitrogen content, it's difficult to obtain the ideal stoichiometry of carbon and nitrogen by using high temperature and high pressure method. So the study of carbon properties is more inclined to computational simulation. Without conducting expensive measurements, modeling the spectrum of electron states of carbonitride makes it possible to obtain important information about the electronic and optical properties, and focus on more specific field of practical application, it can be used in photocatalysts, fuel cell electrodes, lighting equipment, chemical sensors, and other devices. [25] Two-dimensional materials beyond graphene is emerging area of current material sciences. Boron monolayers is the one from this class. we not only demonstrate that borophene (similarly to phosphorene) is unstable at ambient conditions but provide comprehensive study of the physical properties of oxidized borophene sheets and suggest possible applications in the areas of solar energy, sensors, coating and spintronic. Indium Selenide discussed as the one of the most prospective two dimensional materials, we vary not only the adsorbents but also the size of supercell and especially the modes of the optimization, we also check the influence of in-plane and out-of-plane distortions of the substrate, interaction of InSe with environment at some narrow range of conditions and even slight change of these conditions could provide significant change in chemical properties. Two-dimensional materials have ultrathin thickness, the high surface area provides a large number of reactive sites, which makes them efficient adsorbents for gas molecules, these materials efficient in catalysis, sensing, solar energy conversion and storage technologies. [26-29]

Purpose and objectives of the work. The purpose of the thesis is a comprehensive study of the atomic structure of new materials for optics, electronics and photoelectronics based on oxide and low-dimensional systems and the formation of a systematic description of the relationship between the morphology of the material, its chemical stability and the effect of modification in various ways (doping, creating defects, surface oxidation, etc.) on its electronic structure and optical properties. Another goal of the work is to develop a general approach to an adequate description of the physical and chemical properties of nanomaterials with different chemical compositions and morphologies. To achieve the goal of the work, the following tasks were solved:

1. Obtaining information on the relationship between the atomic structure and the optical properties of zinc oxide doped with beryllium ($Zn_{x-1}Be_xO$) for various dopant concentrations.

2. Modeling the atomic structure of carbon nitride (β-C_3N_4) for a system with intrinsic defects (vacancies), surfaces, and nanoclusters. Study of the chemical stability of the surface and identification of the mechanisms of the influence of defects and their chemical passivation on the optical properties of carbon nitride.

3. A systematic study of the step-by-step oxidation process of allotropes of two-dimensional single-layer boron. Analysis of chemical stability and study of the electronic structure of B_xO_y films.

4. Investigation of the effect of distortions of the crystal lattice of a single-layer indium selenide (InSe) membrane on the optical properties and the adsorption characteristics of molecules on its surface. Establishing the relationship between the adsorption properties and flexibility of a single-layer InSe.

5. Study of the formation of chemically stable magnetic centers with the participation of oxidized defects on the surface of β-C_3N_4 and B_xO_y films.

Scientific novelty:

1. For the first time, a systematic study was made of the effect of a stepwise increase in the content of beryllium in zinc oxide on its electronic structure and optical properties.

2. The atomic structure of the β-C_3N_4 surface and its defects, as well as the atomic structure of the nanoclusters of this compound, were modeled for the first

time. The effect of disordering in the atomic structure of β-C_3N_4 on the formation of optical properties is revealed.

3. For the first time, a systematic study of the interactions of two-dimensional boron membranes with the environment was performed.

4. For the first time, chemically stable magnetic centers have been identified in low-demensional materials that do not contain transition metals .

5. For the first time, the role of various methods of modifying the atomic structure in the formation of the adsorption characteristics of molecules on the surface has been established.

6. For the first time, strategies have been developed for modeling the chemical stability of free two-dimensional systems, two-dimensional systems on a substrate and the surface of three-dimensional systems.

7. For the first time, a theoretical assessment of the influence of spatial distortions of the InSe membrane on its electronic structure, optical and chemical properties has been made.

Theoretical and practical significance of the work:

1. The results obtained expand the fundamental understanding of the relationship between the atomic structure and the optical properties of pure and chemically modified low-dimensional systems.

2. The developed approach for assessing chemical stability provides the basis for further theoretical studies in the field of low-dimensional systems. The theoretical calculation protocol developed for InSe can be further used to simulate the electronic structure of similar flexible low-dimensional systems.

3. New methods are proposed to increase the efficiency of photoactive systems.

4. New stable materials for photonics, photochemistry and sensors are proposed.

5. The detected chemically stable magnetic centers on oxidized defects in β-C_3N_4 and B_xO_y films are scientifically interesting as magnetic centers in nonmolecular materials without transition element atoms. The results can be used for further development of magnetic materials without transition elements.

Methodology and research methods. Density functional theory is the most propagated approach in first principles calculations of realistic systems. This method plays an important role in condensed matter theory and material sciences. The electronic structure determines the basic properties of matter such as electric, magnetic, thermal and mechanical.

In adiabatic approximation we exclude dense small size nuclei from consideration and reduce multi-atomic system to multi-electron system. In order to discuss these systems, we make further reduction of multi-electron problem to single-electron by considering of the motion of electron in the field of others. For this approach Hartree-Fock method was developed. The main disadvantage of approximation is ignoring of the spin correlation energy between antiparallel electrons, while density functional theory considering the correlation energy of electrons within exchange-correlation therm. Density functional theory established on Hohenberg-Kohn Theorem, its core idea is to use the density of particles to reflect properties of the ground states of molecules, atoms and solids, so that the corresponding electronic structure and total energy can be obtained. However, Hohenberg-Kohn theorem cannot solve because of the difficulty of the interaction term in kinetic energy functional, so Kohn-Sham equation is proposed.

Calculations were performed within the framework of the density functional theory by using the plane-wave pseudopotential approach in the Cambridge Sequential Total Energy Package codes. We used the generalized gradient approximation of Perdew-Burke-Ernzerhof scheme to describe the exchange-correlation potential. For all systems under study, the following procedure was followed: building a model, choosing parameters for optimization, calculating and analyzing properties.

Thesis to defend:

1.The varying of the optical properties of $Be_xZn_{1-x}O$ is related to the different impurity concentration inducing the changes in the lattice parameter.

2.The main contribution to the change in the optical properties of β-C_3N_4 is made by the deviation of the atomic structure from ideal. The minimum disordering with a standard deviation of 0.3 Å atoms from stoichiometric positions is sufficient to change the absorption spectra of β-C_3N_4.

3.Modification of defects on the β-C_3N_4 surface lead to a significant change in the energy gap between the valence and conduction bands.

4.The two-dimensional boron monolayer (borophene) is a chemically unstable material and, regardless of the initial configuration, will oxidize at room temperature until an amorphous B_xO_y film forms. Oxidation of borophene leads to the transformation of its electronic structure from metal to semiconductor, which makes it a promising material for solar energy, and the influence of adsorption of molecules on the electronic structure of oxidized borophene makes it possible to use it as a sensor.

5.The calculated adsorption energies of various gases on the surface of a single-layer indium selenide (InSe) depend on whether optimization has been made only of atomic positions (which corresponds to a monolayer on a substrate) or of atomic positions and lattice parameters (which corresponds to the case of a free membrane). The obtained results remove the contradictions between the experimental data and previous calculations.

6.Oxidation of borophene, as well as defects on the surface of β-C_3N_4, can lead to the appearance of a magnetic moment in these structures due to the presence of broken bonds. The passivation of these broken bonds is difficult, which makes d0 magnetism chemically stable in these systems.

The degree of reliability of the work results is determined by the use of modern certified computer programs for molecular dynamics and quantum chemical modeling. The results obtained during the work correspond to the known literature data.

Approbation of work

The main results of the dissertation were presented and discussed at 7 international conferences, congresses, symposia.

Scanning Probe Microscopy (Yekaterinburg, 2017), Master class from Springer Nature magazine - Publishing Academy (Yekaterinburg, 2017), Scanning Probe

Microscopy (SPM-2018) (Yekaterinburg, 2018), XVII International Feofilov Symposium on Spectroscopy of Crystals Doped with Rare Earth and Transition Metal Ions (Yekaterinburg, 2018), XIX All-Russian Workshop on the Problems of Condensed Matter Physics (SPFCS-19) in Memory of Tankeev A.P. (Yekaterinburg, 2018), Sino-Russian ASRTU Conference Alternative Energy: Materials, Technologies and Devices (Yekaterinburg, 2018), The Sixth International Young Researchers' Conference Physics. Technologies. Innovation. (Yekaterinburg, 2019).

Personal contribution of the author. The purpose of the work was formulated by the supervisor. The selection of research objects and the formulation of problems were carried out by the supervisor and scientific consultant D.V. Boukhvalov in cooperation with the author of the thesis.

The author has carried out the whole complex of calculations, including the choice of the appropriate mode, pseudopotentials and approximations, building models and visualization. The author took a decisive part in the preparation of scientific publications and reports at conferences.

Discussion and analysis of the results obtained were carried out with the participation of Ph.D. Boukhvalov D.W.

Publications. On the topic of the dissertation work, the author published 7 articles indexed in the international databases WoS, Scopus and included in the list of the Higher Attestation Commission, 2 theses of reports at international conferences.

The structure and scope of the dissertation. The dissertation consists of an introduction, 6 chapters, a conclusion and a list of references. The volume of the dissertation is 143 pages, including 55 figures, 7 tables and a bibliographic list of 239 items.

CHAPTER 1. LITERATURE REVIEW

1.The application of density functional theory

1.1.1 Applications in solid state physics

Density functional theory has been used in many fields of the physics and chemistry, but none so successfully as in the solid state physics. Modern DFT simulation codes can calculate a broad range of structural, chemical, optical, spectroscopic, elastic, vibrational and thermodynamic properties of materials. In semiconductors physics great progress has been made in the modeling of electronic structure of bulk and defect states despite the severe challenges related with description of excited states. Studies are no longer restricted to known crystallographic structures. DFT is increasingly used as an exploratory tool for materials discovery and computational experiments.

1.1.2 Applications in quantum chemistry

Atomization energies: the most common way of testing the performance of new functionals is the comparison with the experimental atomization energies of well-studied sets of small molecules. These comparisons have established the following hierarchy of functionals:

LDA < GGA < hybrid functionals

Hybrid functionals are progressively approaching the desired accuracy in the atomization energies, and in many cases they deliver results comparable with highly sophisticated post-HF methods.

Table 1.1.2.1 – Deviations [kcal/mol] between computed atomization energies and experiment

Molecule	LDA	BLYP
CH	7	0
CH_3	31	-2
CH_4	44	-3
C_2H_2	50	-6

C_2H_4	86	-6
F_2	47	18
O_2	57	19
N_2	32	6
CO	37	1
CO_2	82	11

Ionization and affinity energies: the hybrid functionals can determined these energies with an average error of around 0.2 eV for a large variety of molecules.

1.1.3 Applications in molecular electronics

We were able to attribute distinctive features of the current-voltage of the symmetric and asymmetric molecule to their individual molecular levels obtained from ab initio calculations. Three subsystems: central cluster and leads [30],

$$\hat{H} = \hat{H}_L + \hat{H}_R + \hat{H}_C + \hat{V}$$

Central cluster: Density functional calculation (DFT),

$$\hat{H}_C = \sum_i \varepsilon_i \hat{d}^+ \hat{d}$$

(a) Basis set: LANL2DZ (relativistic core pseudopotentials)

(b) DFT calculations: B3LYP hybrid functional.

Leads: The reservoirs are modeled as two perfect semi-infinite crystals using a tight-binding parameterization, coupling:

$$\hat{V} = \sum_{ij} v_{ij} (\hat{d}^+ \hat{c}_j + h.c.)$$

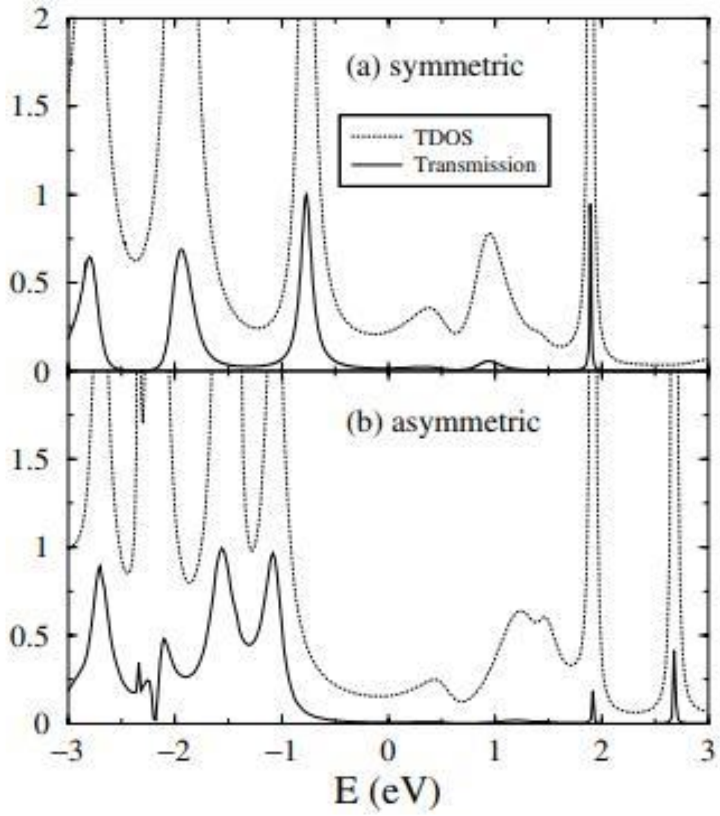

Figure 1.1.3.1 – Total density of states of the molecule and zero-bias total transmission as a function of the energy for both molecules. The Fermi energy is set to zero.

Let us start by analyzing the linear response regime, in fig. 1.1.3.1 the total density of states of the molecule and zero-bias total transmission as a function of the energy for both molecules. The Fermi energy is set to zero. As can be seen in the TDOS, in both cases the covalent bond between Au and S results in a strong hybridization between the molecular orbitals and the extended states of the metallic electrodes. The formation of wide energy bands suggests the absence of Coulomb blockade in this type of molecular junction.

The zero-bias total transmission as a $\hat{t}\hat{t}^{\dagger}$ function of energy follows closely the TDOS. The transmission is dominated overwhelmingly by a single channel in the energy window shown in the figure, and the corresponding eigenvalues of at the Fermi energy are T_{sym}=0.014 and T_{asym}=0.006. The decomposition of this channel into molecular orbitals provides us information on the relevance of the different molecular levels.

1.1.4 Applications in molecular systems modeling

Present trends in the miniaturization of electronic devices suggest that ultimately single atoms and molecules may be used as electronically active elements in a variety of applications. Here a candidate to such a theory, which based on the combination of quantum chemistry methods and Green functions techniques. The main goal is to show how the electronic structure of single atoms and molecules controls the macroscopic electrical properties of the circuits in which they are used as building blocks.

Making the model more realistic [31]: account for proper charge transfer DFT predicts ~ 0.1 e^-, E_F is shifted down ~ 6 eV, replace the flat DOS by the proper bulk Pt-Green's function.

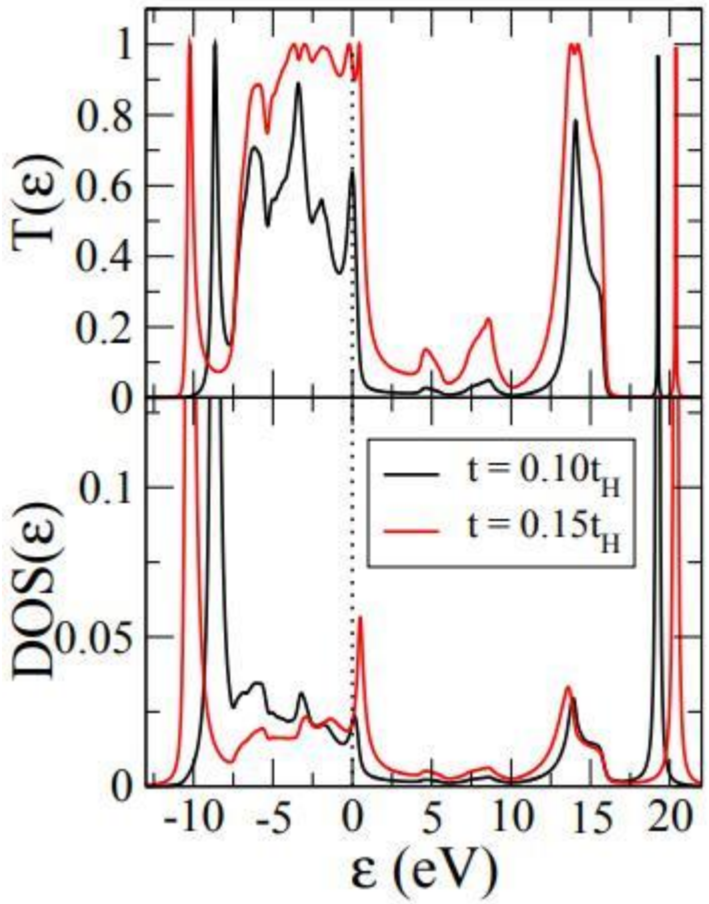

Figure 1.1.4.1 – Transmission and LDOS projected into one of the H atoms for two values of the hopping t. Fermi energy is set to zero.

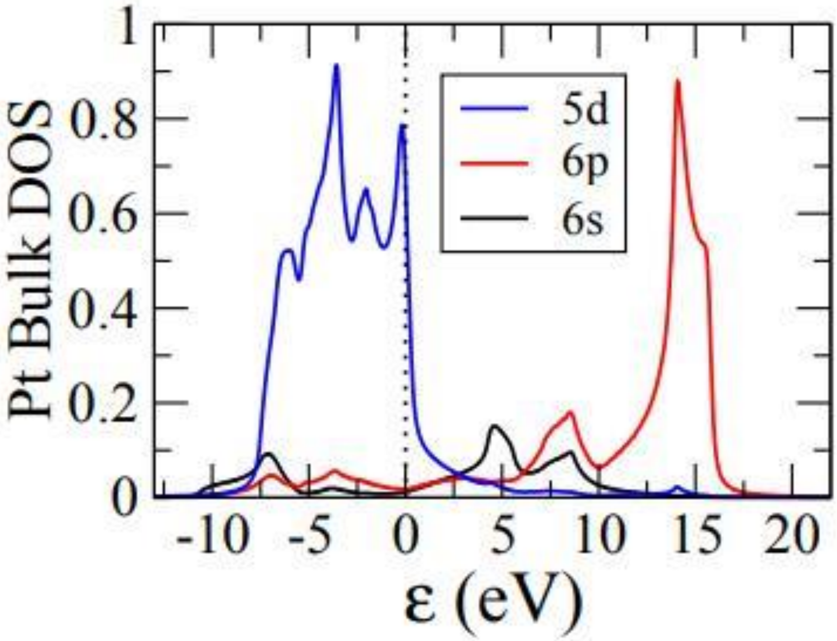

Figure 1.1.4.2 – Bulk DOS of the Pt reservoirs

The Pt bulk DOS is shown in Figures 1.1.4.1 and 1.1.4.2. We also show the transmission and the LDOS projected into one of the H atoms for two values of the coupling to the leads t. One can see that for realistic values of t ≈1-2 eV, the transmission at E_F can now indeed reach values close to one. Therefore, we conclude that the high conductance of H_2 is due to the charge transfer between H_2 and the Pt leads and the strong hybridization between the bonding state and the d band of Pt. This mechanism is not exclusive of Pt and it must also operate in other transition metals, as it was shown experimentally for Pd, the simple model shows a transmission compatible with the experiment, the value of transferred charge and the strong hybridization with the Pt d-band make H_2 a good conductor.

The conduction mechanism consists of two main ingredients. First, the catalytic activity of platinum is responsible for a significant charge transfer between H_2 and the Pt contacts, which moves the bonding state of the molecule towards the Fermi energy. Then, the strong hybridization with the d band of the Pt leads provides a large broadening of the bonding state, finally allowing for a high transmission. charge transfer and the electronic structure of the metallic contacts are essential for the proper description of the electrical conduction in single-molecule devices.

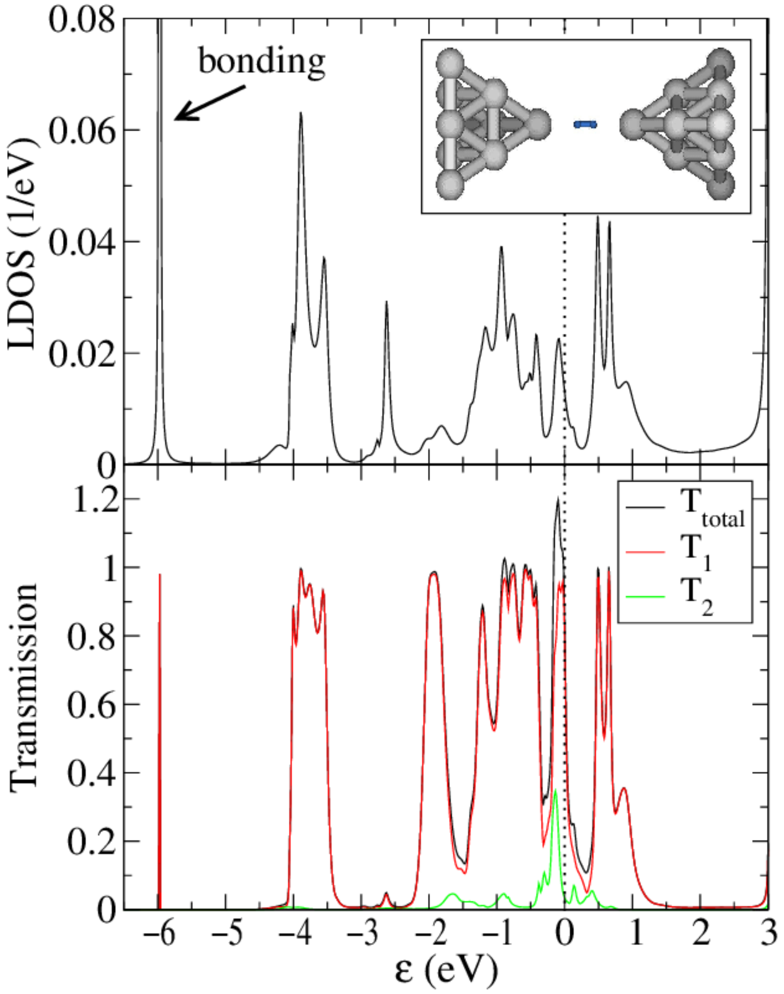

Figure 1.1.4.3 – Transmission and LDOS projected onto one of the H atoms as a function of energy for the Pt-H_2-Pt structure, the central cluster of which is shown in the inset.

The most probable configuration [32] is shown in the fig. 1.1.4.3, where the H_2 is coupled to a single Pt atom on either side (top position). In this geometry the vibrational mode of the center of mass motion of H_2, which is the one seen in the experiment, has an energy of 55.6 meV, lying in the range of the experimental values. We also can see that the transmission and the LDOS projected into the orbitals of one of the H atoms. The total transmission at the Fermi energy is T_{total} =0.86 and it is largely dominated by a single channel, in agreement with experimental results. In the LDOS: the bonding state of the molecule appears as a peak at ~ 6 eV below E_F and the antibonding state, not shown, is located at ~18 eV above E_F; around the Fermi energy the gap between the molecular states is filled due to the strong hybridization with the Pt leads, which is indeed the mechanism behind the high conductance of this molecule. The DFT calculations confirm the conduction mechanism through hydrogen and provide a good description of the experimental results.

1.1.5 Current problems of the methodology of basic principles of calculation

DFT cannot be used to find every single property. Here are some key areas in which DFT cannot predict properties.

Band Gap: Absolute value of band gap cannot be predicted. GW method is describe many-body interactions, in practice for computational reasons, some codes implement this method. This greatly simplifies the calculations, but also makes important approximations.

High temperature properties: it is not possible to predict various high temperature properties close to melting point of the material. But a very recently published paper have improved the formalism which can even account for high temperature properties [33]. Even after this improvement it would not be possible to predict various properties close to and above melting point.

Superconductivity and lattice vibrations: superconductivity is attributed to the formation of Cooper pairs, pairs of electrons interacting through the exchange of phonon. One way to implement the theory of crystal vibrations in a practical way is to explicitly calculate the forces between every atom in the crystal and construct the force constant matrix of the crystal. This force constant matrix then allows us to calculate the normal modes of at any particular wavevector, q. To calculate the forces caused by an atom i, we displace atom i, and then use DFT to calculate the forces on every atom using the Hellman-Feynman theorem. This method of calculating the force constant matrix by explicitly displacing atoms is called the frozen-phonon method, phonons calculations usually implemented in codes by frozen phonons methods. Since it is long distance interaction which is not taken into account in DFT hence DFT cannot accurately predict superconductivity.

1.1.6 New approaches in first-principle calculations

In addition to DFT, DFT + DMFT is actively developing: Ab initio approach to correlated electron materials, powerful tool to study/predict properties of correlated materials, Hamiltonian from DFT could be inserted in many-body calculations (depending from atomic structure of the compound).

First-principles calculations have also been extensively applied to interpret electron energy loss spectra measurements - many (scanning) transmission electron microscopes are fitted with an electron energy loss spectrum. Electron energy loss spectra provide a method of probing the bonding within a material. Depending on the energy range examined the processes involved include excitations of core electrons into the conduction states, and plasma excitations of the valence electrons. DFT has been shown to be sufficient to interpret electron energy loss spectra of a wide range of materials. It is a particularly important technique for the study of nanomaterials as the latest generation of scanning transmission electron microscopy can obtain high-energy resolution electron energy loss spectra at atomic-level spatial resolution.

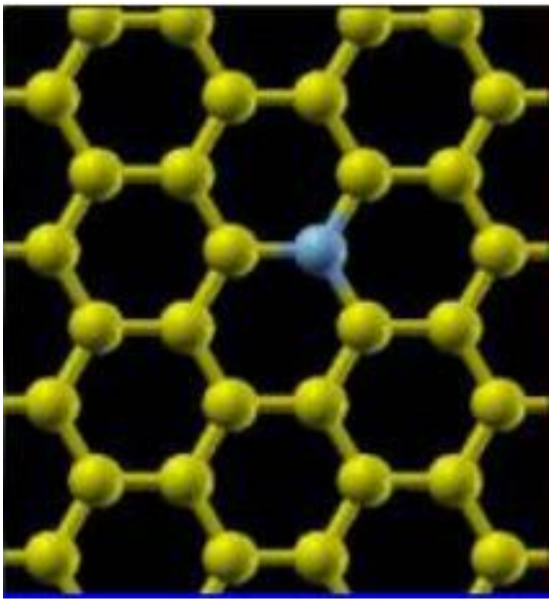

(a)

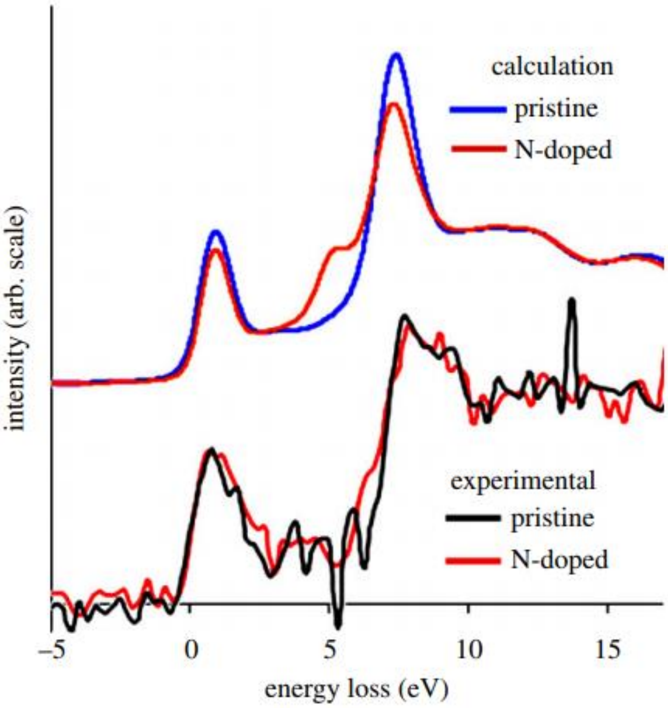

(b)

Figure 1.1.6.1 – A nitrogen substitutional dopant atom in graphene (a) model used for simulations, (b) experimental and calculated electron energy loss spectra data

Fig. 1.1.6.1, as an illustration, (a) model used for simulations and (b) experimental and calculated electron energy loss spectra data [34], CASTEP was recently used to predict the change in the carbon K-edge spectrum (an excitation of the 1s electron) owing to the presence of a substitutional nitrogen defect in graphene. The calculations predicted a pronounced shoulder to the σ peak for the carbon atom directly bonded to the nitrogen. Carbon atoms greater than three bonds from the defect were shown to have spectra essentially identical to pristine graphene. These subtle changes were subsequently observed in scanning transmission electron microscopy electron energy loss spectra measurements on N-doped graphene, providing direct evidence of the N-C bond.

Example: Below, the spin susceptibility of alkali metals χ/χ_0, where χ_0 is the Pauli susceptibility of a free electron gas.

Table 1.1.6.1 – The spin susceptibility of alkali metals

Metal	DFT result (LDA)	Experiment
Li	2.66	2.57
Na	1.62	1.65
K	1.79	1.70
Rb	1.78	1.72
Cs	2.20	2.24

S. H. Vosko, et al. (1975) [35] make a priori calculations of χ for the alkalis using new variational-principle, density-functional theory of the spin susceptibility χ. Crystalline effects are calculated by the spherical-cell method and the local spin-density approximation is used for the exchange-correlation functionals.

As seen in Table 1.1.6.1, its agreement with experiment worsens progressively as we consider larger core systems, to account simultaneously for band effects and the influence of the core on exchange and correlation, a model Hamiltonian can be introduced DFT result. This leads to

$$x/x_0(r_s)=(m_b/m)[x_h(r_s^*)/x_0(r_s^*)]$$

It indicates the importance of the influence of the core electrons on exchange-correlation. DFT describes very accurately alkali metals. The excellent agreement between the results and recent experiments establishes the validity of this new theory and the correctness of the theoretical values for the exchange-correlation enhancement of χ for a homogeneous electron gas for $r_s \leq 5$.

The underestimation of the band gap with LDA or GGAs causes a complete closing of the computed minority-spin band gap in $CoFe_{0.5}Mn_{0.5}Si$, predicting the material to be an ordinary metal and consequently of no use in spintronics applications. However, the inclusion of a small Hubbard U term (typically around 2 eV) on the Fe and Mn d-states recovers the localization, and opens up the minority-spin band-gap while preserving, correctly, the metallic character of the majority spins.

DFT simulations are increasingly important in the field of device technologies, and used to study everything from conventional complementary metal oxide semiconductor (CMOS) devices to future devices based on half-metals, thermoelectrics or multiferroics. Obtaining the correct band-gap for the constituent (doped/defect) materials is essential to describe the functionality of these devices.

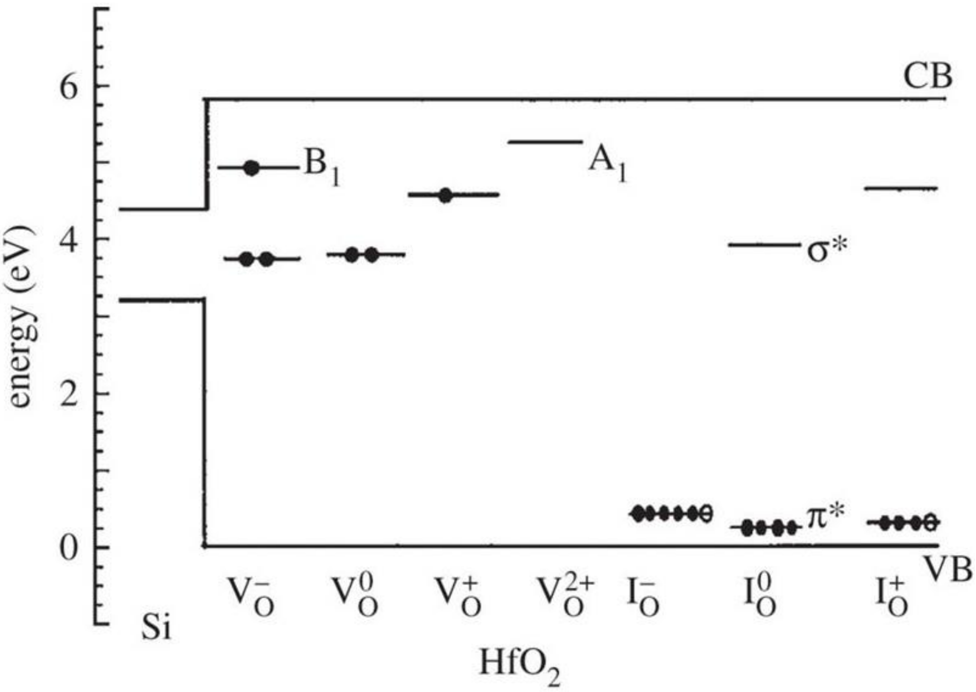

Figure 1.1.6.2 – Defect levels in HfO_2 arising from oxygen vacancied and interstitials in a variety of charge states

In the case of HfO_2 [36], defect levels in HfO_2 arising from oxygen vacancies(V) and interstitials(I) in a variety of charge states shown in fig. 1.1.6.2. The top valence band (VB) and bottom conduction band (CB) are shown for reference. The short lines show the energy level position within the gap and the dots show electron occupancies. On the x-axis, V indicates vacancy and I interstitial with the superscripts showing the defect charge state. Screened-exchange calculations showed that the oxygen vacancy gives rise to defect levels near the conduction-band edge of silicon, so it was determined that this defect was the main charge trap in HfO_2-Si interfaces. For HfO_2 to be used successfully in new devices, such defects must be passivated using an oxygen-rich processing technique (we will discuss it below in the chapter 4 about the chemical properties of surface and nanocluster of C_3N_4 and unavoidably passivated at ambient conditions.).

The high-k dielectric refers to a material with a high dielectric constant (k, kappa), as compared to silicon dioxide. High-k dielectrics are used in semiconductor manufacturing processes where they are usually used to replace a silicon dioxide gate dielectric or another dielectric layer of a device. For the high-k materials have a higher defect concentration leading to large electron/hole trapping, lower mobility, changes in threshold voltages and other sources of instability. Therefore, it is crucial to understand the electronic structure of the defects and the processing conditions required to minimize their concentration. This requires accurate, predictive electronic structure calculations, including excited states and semiconductor defect energy levels, for which screened exchange is well suited.

The electronic band-gap of a material may be defined as the difference between the electron affinity (the energy of adding an electron to the system) and the first ionization energy (the energy of removing an electron from the system); each of these can be calculated using conventional DFT. But these calculations provide underestimation of the value of the band-gap because use of exchange-correlation functional. For providing values of the bandgap closer to experimental, DFT+U is a popular method for treating the effects of self-interaction and it has been applied to a wide range of materials.

The example, native vacancy defects in typical strongly correlated oxides NiO have been investigated using the GGA+U method [37]. First-principles computations were performed using the Vienna Ab initio Simulation Package (VASP) code in the calculations, electronic correlations were also included in a simple rotationally invariant DFT+U version, in this method, the optimal combination of U = 6.3 eV and J = 1 eV was found to improve the prediction of the electronic structure and magnetic properties.

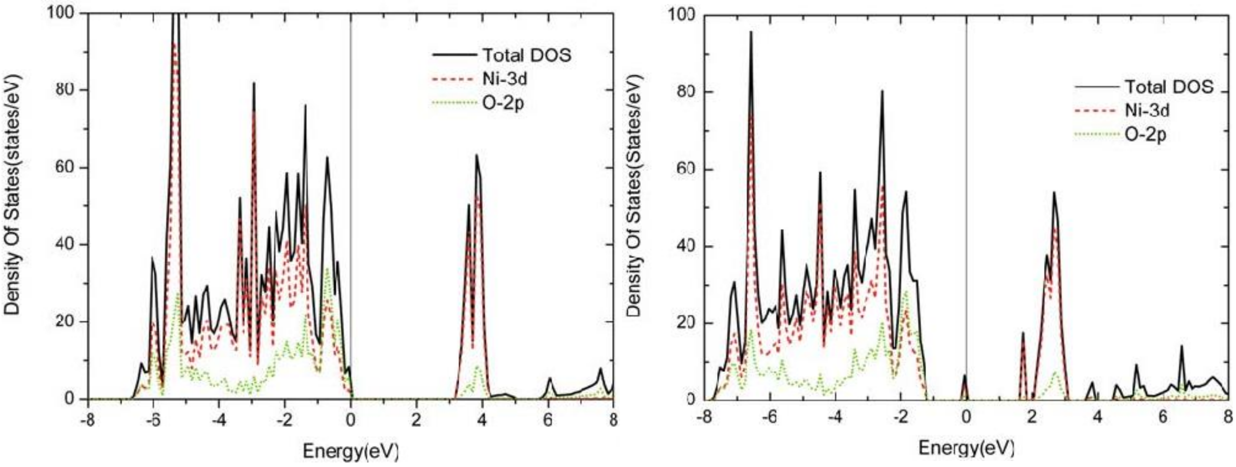

Figure 1.1.6.3 – The Total and partial density of states (spin up) of perfect NiO calculated using 64-atom supercell (a) and oxygen vacancy in a 2 × 2 × 2 NiO supercell (b). The Fermi energy is set to 0.0 eV.

The above fig. 1.1.6.3 are respectively total and partial density of states of perfect NiO calculated using 64-atom supercell and total and partial DOS of oxygen vacancy in a 2×2×2 NiO supercell. It shows the density of states of perfect NiO with 64 atoms supercell. It can be seen that the system exhibits a typical insulator character with bandgap of about 3.1 eV, O 2*p* is mixed with Ni 3d at the top of the valence band, NiO thus is a mixture of charge-transfer and Mott-Hubbard type.

Now, we turn our attention to the DOS of NiO with oxygen defect. As shown in the figure, an oxygen vacancy leads to formation of a set of impurity levels, with a low-lying level in band gap and higher lying levels just below the conduction band, which indicates that electronic structure exhibits a clear donor character. The 3*d* states of Ni atoms dominate the impurity states, where as O-2*p* states contribute little to it. These impurity levels are formed from the dangling *3d* orbital of Ni atoms coordinating the vacancy site. As shown in the density of states, the bandgap is narrowing largely and the system becomes semi-conducting. From the calculation, we also find that the magnetic moment of the system is zero and this nonmagnetic behavior does not change with ionized state of vacancy. These results indicate that oxygen vacancy cannot induce half-metal ferromagnetism.

This is example of $CoFe_{0.5}Mn_{0.5}Si$ [38], which is a half-metal, meaning that the states at the Fermi level are completely spin-polarized. Half-metals are of great interest for spintronics applications because an applied voltage causes a spin current to flow. The density of states around the Fermi level (dashed line) for the half-metal Heusler alloy $CoFe_{0.5}Mn_{0.5}Si$ calculated using PBE (a) and PBE + U (b) (Fig. 1.1.6.4). With the PBE exchange-correlation functional the system is predicted to be fully metallic, where inclusion of a modest Hubbard U (U = 2.1 eV) opens up a band gap for the minority spins.

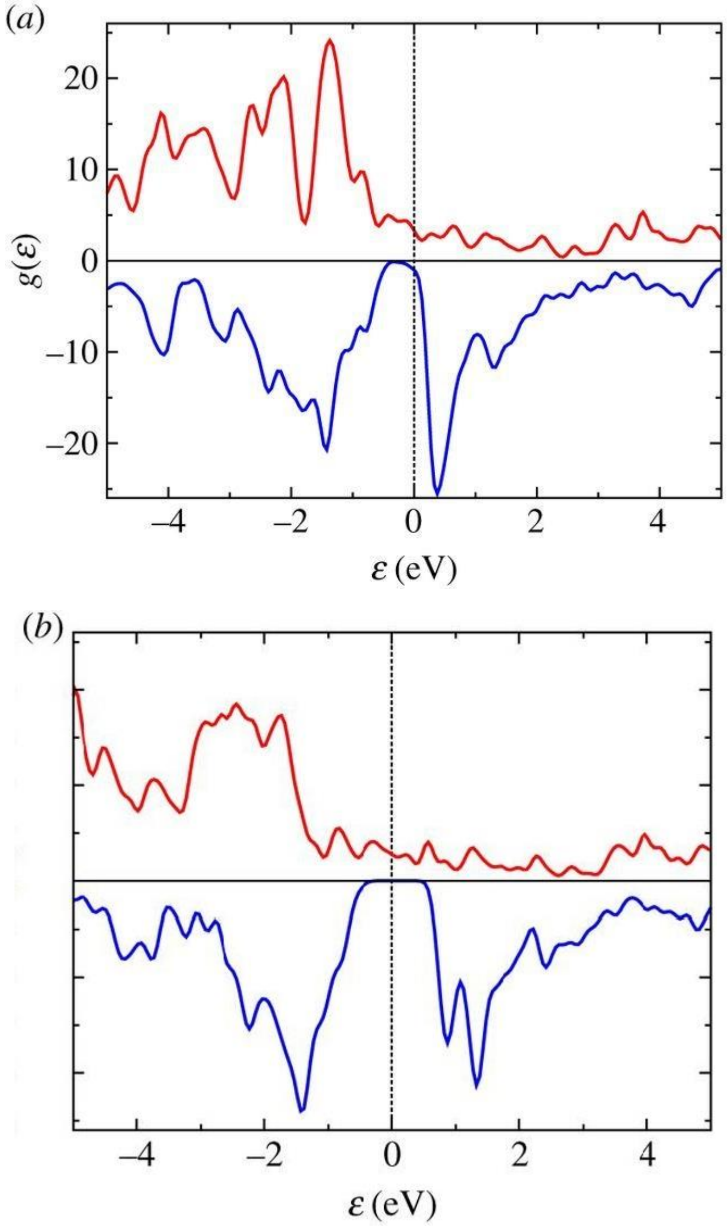

Figure 1.1.6.4 – The DOS around the Fermi level for the half-metal Heusler alloy $CoFe_{0.5}Mn_{0.5}Si$ computed using PBE (a) and PBE+U (b).

1.2From methods to materials

1.2.1 Investigation of the condition of defects according to the properties of materials

Having described the history of the creation and development of methods for calculations within the framework of the photomultiplier, we will proceed to describe the features of the methods associated with the materials selected for study in our work. Zinc oxide was chosen as an object for studying the effect of doping on the optical properties of low-dimensional systems, which is considered as a promising material for multiple applications, such as photoelectronics and photochemistry. [4-7] Beryllium was chosen as a dopant for ZnO, which, unlike transition metal impurities, is not prone to clustering in the zinc oxide matrix. [8] To begin with, we will look at previous achievements in the field of modeling zinc oxide and other similar objects.

We can predict various phase transformations that takes place under mechanical strain. Crystal structure changes even when dimension of the system is altered for example ZnO have wurtzite structure in bulk but it is graphitic in nanowire this can be predicted by DFT. Calculated cohesive energy per atom of the system we can be used to predict the phase transformations. Phase transformation are determined using X-ray and neutron diffraction.

Here we illustrate how phase transformation can be estimated using DFT in ZnS. ZnS exist in the B3 (zinc blende) at equilibrium and B1 (rocksalt) crystal structures at high pressure. Transformation takes place when pressure of both crystal structure is same. Now to calculated pressure at what pressure zinc blend structure of ZnS changes to rocksalt we use Birch–Murnaghan equation of state that relates pressure to volume and energy [39].

$P=-(\partial E/\partial V)$, where P is pressure, E is energy of the system (in our case energy per unit cell) and V is volume of system (in our case volume of unit cell).

To calculate pressure at various volume of unit cell, calculate energy per unit volume at various volume of unit cell of both zinc blend and rocksalt crystal structure. Energy per unit cell can be easily calculated using DFT to very high degree of accuracy by choosing suitable input parameters. Figure below shows energy per unit cell vs volume of unit cell of two crystal structure [40].

Slope of the curve give pressure at various volume of unit cell. Common tangent to two curves give the pressure of phase transformation since at that point pressure is same for two crystal structure. Thus calculated value of phase transformation is 16.1 Gpa. Experimental value of pressure of phase transformation is 15-18 Gpa [41].

It can predict the best possible crystal structure without any input of experimental data what so ever. Geometries of various organics molecules can be determined. Defect structure as vacancy, grain boundary etc. can be estimated. Surface structures and adsorption can be predicted for variety of systems. Diffusion rate of vacancy, interstitial etc. can be quantified by calculating migration barrier to diffusion of these species.

Experimentally structural properties are determined using X-ray and neutron diffraction. Various types of microscopy can also determine structural properties of the surfaces. Vacancy and interstitial defects have to be measured with various composition to get diffusion rate.

By the means of DFT we can predict various mechanical properties of given material such as Elastic Modulus, Compressibility, Thermal expansion coefficients. Experimentally mechanical properties can be determined using tensile test, hardness test (Vicker and Rockwell) [42,43]. Thermal expansion can be determined using X-ray diffraction. By calculating which is phase is stable at various composition and various temperatures we can plot phase diagram. Phase diagram can be made by finding crystal structure at various composition and temperature. Various alloy composition has to be made and crystal structure could be predicted and compared with experimental phase diagrams.

Band structure and electronic density of states can be calculated of almost any given system. Dipole moment of molecule, interface can be calculated. Conductivity and transport properties of materials can be estimated. Ionization energies and electron affinity can be estimated. Band offset can be calculated at hetero-junctions.

Experimentally electronic structure of valence can be measured X-ray photoemission spectroscopy (XES). Conduction band can be studied by the means of X-ray adsorption spectroscopy (XAS). Band structure on the surface is measured by angle-resolved photoemission spectroscopy (ARPES). Though band gap is underestimated by DFT. But change in band gap (trend in band gap) with strain can be very well approximated. Hence optical spectra can be estimated. Luminescence and fluorescence of materials can be found using DFT. Band gap, luminescence and fluorescence can be measured using UV-Visible spectroscopy.

In the early 1990s, p-type thin film preparation of wide bandgap semiconductor GaN was proposed by Nakamura and other researchers, GaN is used in short wavelength light-emitting diodes, lasers, and other devices, it is characterized by wide band gap, high thermal conductivity and excellent chemical stability [44]. But later it was found that the material of Ga is scarce and costly, highfrequency performance of GaN is poor and due to its p-type doping is not good, the obtained hole concentration and mobility are small, which is 0.1%-1% doping efficiency [45], these factors have led to GaN being affected by photoelectric devices. Therefore, people hope to find suitable materials to replace GaN. However, room temperature optically pumping ultraviolet laser of ZnO thin film was first reported at the end of the 20th century, and it was drawn attention from researchers [46]. So far, ZnO materials are still being studied, and it has made great achievements in the field of short wavelength photoelectricity. In comparison to GaN, ZnO is a promising material with low cost, the same crystal structure as GaN, and their lattice constants are close. ZnO has a large melting point, it’s easy to doping and non-toxic, its characteristics include radiation resistance, thermal stability, chemical stability and electromechanical coupling [47]. The conditions of the zinc oxide film can be less than 500℃ and can grow at low temperatures so that the substrate can be selected from a single crystal substrate or an amorphous substrate [48]. II-VI wide-gap semiconductor zinc oxide has become a great importance to the photoelectric materials, and it was widely used in ultraviolet light photoelectric devices [49,50].

The band gap of zinc oxide is about 3.37eV, the binding energy of exciton can reach as high as 60meV, which is much larger than the thermal energy 26meV at room temperature. As a result, the exciton is stimulated above room temperature. When compared to the luminescence of the electron-hole pair, the luminous efficiency of exciton is higher. It has a wide range of applications, including lasers, light-emitting diodes, gas sensors, ultraviolet detectors, transparent conductive films, solar cells, blue light, and blue-green light devices [51]. Liu et al. have reported on the fabrication and characterization of ZnO based metal-semiconductor-metal ultraviolet sensitive photodetectors and the growth of 1μm thick N-doped ZnO on the surface of sapphire [52]. They used organic chemical vapor deposition method, the detector's cutoff wavelength is 373 nm, the resistivity of ntype ZnO was improved by N-doped ZnO and the photoresponse is very high, reaching 400A/W at 5V bias. ZnO is also regarded as the starting material for white light emission, its luminescence properties are related to the selection of doping elements, preparation conditions, preparation methods and excitation conditions.

Experimental [53-55] studies have found that magnesium doped zinc oxide form $Mg_xZn_{1-x}O$ ternary mixed crystal, as Mg concentrations ($x \leq 0.33$) increases, the band gap of $Mg_xZn_{1-x}O$ ternary mixed crystal increases from 3.3 to 3.99eV, but because of the different crystal structures and large lattice mismatch between ZnO (3.25Å, hexagonal) and MgO (4.22Å, cubic) observed crystal phase segregation between ZnO and MgO as Mg concentrations ($x \geq 0.36$) [56]. Recently used Be instead of Mg in order to expand the band gap, the band gap of BeO is 10.6eV, the lattice structure of BeO as the same as ZnO. Ryu et al. have investigated $Be_xZn_{1-x}O$ ternary mixed crystal, they synthesized BeZnO films on c-Al_2O_3 substrates by the method of hybrid beam deposition [57, 58]. The experimental results indicated that the concentration of Be varied over the entire range from 0% to 100% and no phase segregation between ZnO and BeO was detected. After that, they got ZnO-based ultraviolet light emitting diodes that employ BeZnO/ ZnO [59]. Recent experimental works discussed the methods of the synthesis of BeZnO ternary alloys and stability of the crystal structure [60-63]. In all experimental works [60-65] was detected a gradual increase of bandage with an increase of Be-content. Theoretical works about BeZnO systems mainly considered changes of lattice constants and the band gap [66,67], quantum wheel behavior [68,69] piezoelectricity [70] or impurities in BeZnO systems [71,72]. Electronic structure and optical properties of these systems remain out of focus of current theoretical works.

1.2.2 Modeling of nanosystems and their stability

After mastering the features of the calculation procedure based on doped zinc oxide, we proceed to review systems in which the features of the nano-state play an important role. The first object of our study is β-C_3N_4 or carbonitride. Carbonitride is currently considered as a prospective material for various applications, such as photocatalysts, fuel cell electrodes, light-emitting equipment, chemical sensors, and other devices[73]. Initially, theory has predicted that the hardness of C_3N_4 with Si_3N_4 crystal structure can be comparable to diamond [74]. This prediction will be soon confirmed experimentally [75-80]. All experimental works demonstrate sensitivity of chemical and optical properties to the method of fabrication [76-81]. The next step was development of the carbonitride nanostructures, which demonstrate outstanding fluorescence and luminescence [82-89]. Because formation of C_3N_4 films occurs at high pressures and temperatures, unavoidable loss of nitrogen results in lack of crystallinity in these materials, so the study of carbon properties is more inclined to computational simulation.

Theoretical modelling of various structural phases of C_3N_4 reveals the presence of indirect gap in β, α, and cubic phases and direct gap in graphitic phase. The latter phase also has the lowest total energy. The cause of the decreasing of the bandgap in graphitic phase is sp^2 hybridization of carbon atoms. [90] The phase with the highest density is the cubic one, while the graphitic one has the lowest. The largest difference between these structures involves the hybridization of nitrogen and carbon. There are sp^2 and sp^3 hybridizations on carbon and nitrogen in α-C_3N_4 and β-C_3N_4, respectively. In pseudocubic C_3N_4 or cubic C_3N_4, both carbon and nitrogen is in sp^3 hybridization [90]. Theoretical modeling reports dependence of optical properties of β-C_3N_4 on pressure [91]. Bandgap values of α-, β-, cubic-, pseudocubic-C_3N_4, g-h-triazine, g-o-triazine, and g-h-heptazine were calculated by GW method [92]. The pseudocubic phase and g-h-triazine phase had direct band gaps, while others had indirect band gaps. M. L. Cohen predicted that if copious amounts of $B_xC_yN_z$ and C nanotubes can be synthesized they may provide new forms of tough coatings [93]. The study of the structural and electronic properties of Si_3N_4 and the hypothetical compound C_3N_4, demonstrates the sound velocity in C_3N_4 is estimated to be over 20% larger than that in Si_3N_4. This large sound velocity could lead to useful thermal properties in C_3N_4, such as a high thermal conductivity. [94]

In aforementioned works, only the systems with perfect crystal structure were considered. Recent progress in carbon-based plasmonics [94-100] also requires consideration of the surface and nano-phases of carbonitride. Taking into account effect of disorder, surface, and defects is the further logical step toward understanding electronic structure and optical properties of realistic carbonitride structures [69-89].

Since the successful isolation of graphene, two-dimensional (2D) materials have been a focus of research in electronic devices due to their unique physical properties and potential applications. [101-103] Successful production of multiple new 2D compounds stimulates theoretical design of future members of this class. There two main approaches to the theoretical predicting of novel 2D materials. The first is consideration of the layers as naturally layered structures as separate monolayer (for example graphene and graphite, phosphorene and black phosphorous). The second approach is varying of the chemical composition of already synthesized 2D structures with keeping of geometrical structure (for example multiple layered dichalcogenides beyond $MoSe_2$). The third approachis theoretical design of completely new compounds (for example silicene and germanene). Recent synthesis of silicene [104] demonstrate efficacy of latter approach.

The next material to be studied in the framework of our work was borophene, a two-dimensional boron. Boron is the neighbor of carbon in the periodic table and similarly to carbon has a multiple valence. These facts stimulate modeling of boron analogous of carbon low dimensional structures. Initially was discussed stability of boron-based materials with fullerene-like boron structures [105], boron nanotubes [106] and further 2D boron. [107] Dozens of simulated allotropes of 2D boron with similar atomic structure and almost the same total energy per boron atoms were reported. The nature of this multiplicity of 2D boron allotropes was also discussed. [108] Successful synthesis of silicene on metallic substrate [109] stimulate the modelling of the grown of 2D boron over the most used for the grown of 2D systems metallic substrates. [110].

Another two-dimensional system for studying the stability and properties of which was produced is indium selenide. Recently, indium selenide (InSe) with a hexagonal structure and a typical layered semiconductor [111-113] characteristic has gained increasing attention owing to its intriguing electronic properties. [114-118] The experimental results evidence that the thinner InSe films rapid oxidative degradation. [114] At ambient conditions some small molecules (O_2, CO, H_2O and NO_2) are always interact with the surface of two-dimensional nanomaterials. These small molecules can modify the electronic and optical properties of two-dimensional nanomaterials. [119-123] Another work [124] provides experimental and theoretical evidences of chemical stability of InSe-monolayers.

1.3 Conclusion

The purpose of this review was to view the trends in study of the effect of the modification of low-dimensional systems on their electronic structure and optical properties and see how the study on theoretical and experimental have changed and are still changing. It is clear from the research reviewed that the greatly favors applications of low-dimensional materials in electronics, optoelectronics and other fields due to their physical and chemical properties. Along with this, these materials were used in catalysis, sensing, solar energy conversion and storage technologies. Based on the studies and analyzes of literature review, this thesis include more systematic studies on the electronic structure, optical and chemical properties of oxide and low-dimensional systems in order to more effective application in photonics, photochemistry, sensors and other fields.

CHAPTER 2. THEORETICAL AND METHODOLOGICAL BASIS OF THIS STUDY

2.1 Density functional theory

Density functional theory [125-128] is the most propagated and used approach in first-principles calculation. The method has been the dominant technique for the quantum mechanical simulation of periodic systems in the past. Because of the development of science and technology, recently density functional theory has also been adopted by quantum chemists, now it is widely used for the simulation of energy surfaces in molecules.

As we all know, atoms are made up of nuclei and electrons and the structure of electronic clouds determines interatomic interactions and the basic properties of matter. First-principle methods usually apply to studies the electronic structure of matter. To increase the size of considered systems we must use a certain approximate method to simplify description of the multi-particle system. At the first step, we separate the motion of the nucleus from the electron. In other words, the transformation of a multi-particle system to a multi-electron system, known as the adiabatic approximation [129].

In order to solve the systems beyond hydrogen atom, the multi-electron problem is transformed into a single-electron problem when each electron considered as existing in effective field created by nuclei and other electrons (Hartree–Fock equation) [130]. But the serious disadvantage of this approximation is to ignore the correlation energy between electrons with antiparallel spins. Various approximation used for take into account exchange-correlation energy.

The next step in development of density functional theory is Hohenberg-Kohn theorem [131]. The core idea of the approach is to use the density of particles to reflect the properties of the ground state of molecules, atoms and solids, so that the corresponding electronic structure and total energy can be obtained. However, the Hohenberg-Kohn theorem cannot solve the difficulty of kinetic energy functional in the interaction, so the Kohn-Sham equation [132] is proposed.

The density functional theory is presently the most successful approach to compute the electronic structure of matter. Its applicability ranges from atoms, molecules and solids to nuclei and quantum and classical fluids. In its original formulation, the density functional theory provides properties of a systems in the ground state and the description of the electron density plays a key role.

Density functional theory predicts a large variety of molecular properties: molecular structures, vibrational frequencies, atomization energies, electric and magnetic properties, reaction paths, etc. The original density functional theory has been generalized to deal with many different situations: spin polarized systems, multicomponent systems such as nuclei and electron hole droplets, free energy at finite temperatures, superconductors with electronic pairing mechanisms, relativistic electrons, time-dependent phenomena and excited states, bosons, molecular dynamics, etc.

The Schrödinger equation:

The ultimate goal of most approaches in solid state physics and quantum chemistry is the solution of the time-independent, non-relativistic Schrödinger equation

$$\hat{H}\Psi_i(\vec{x}_1,\vec{x}_2,\ldots,\vec{x}_N,\vec{R}_1,\vec{R}_2,\ldots,\vec{R}_M) = E_i\Psi_i(\vec{x}_1,\vec{x}_2,\ldots,\vec{x}_N,\vec{R}_1,\vec{R}_2,\ldots,\vec{R}_M) \tag{2.1.1}$$

$\hat{H}$ is the Hamiltonian for a system consisting of M nuclei and N electrons:

$$\hat{H} = -\frac{1}{2}\sum_{i=1}^{N}\nabla_i^2 - \frac{1}{2}\sum_{A=1}^{M}\frac{1}{M_A}\nabla_A^2 - \sum_{i=1}^{N}\sum_{A=1}^{M}\frac{Z_A}{r_{iA}} + \sum_{i=1}^{N}\sum_{j>i}^{N}\frac{1}{r_{ij}} + \sum_{A=1}^{M}\sum_{B>A}^{M}\frac{Z_A Z_B}{R_{AB}} \tag{2.1.2}$$

where A and B run over the M nuclei while i and j denote the N electrons in the system.

The first two terms describe the kinetic energy of the electrons and nuclei. The other three terms represent the attractive electrostatic interaction between the nuclei and the electrons and repulsive potential due to the electron-electron and nucleus-nucleus interactions.

Born-Oppenheimer approximation: due to their masses the nuclei move much slower than the electrons, we can consider the electrons as moving in the field of fixed nuclei, the nuclear kinetic energy is zero and their potential energy is merely a constant. Thus, the electronic Hamiltonian reduces to

$$\hat{H}_{elec} = -\frac{1}{2}\sum_{i=1}^{N}\nabla_i^2 - \sum_{i=1}^{N}\sum_{A=1}^{M}\frac{Z_A}{r_{iA}} + \sum_{i=1}^{N}\sum_{j>i}^{N}\frac{1}{r_{ij}} = \hat{T} + \hat{V}_{Ne} + \hat{V}_{ee} \tag{2.1.3}$$

The solution of the Schrödinger equation with $\hat{H}_{elec}$ is the electronic wave function $\hat{\Psi}_{elec}$ and the electronic energy E_{elec}. The total energy E_{tot} is the sum of E_{elec} and the constant nuclear repulsion term E_{nuc}.

$$\hat{H}_{elec}\Psi_{elec} = E_{elec}\Psi_{elec} \tag{2.1.4}$$

$$E_{tot} = E_{elec} + E_{nuc} \tag{2.1.5}$$

$$E_{nuc} = \sum_{A=1}^{M}\sum_{B>A}^{M}\frac{Z_A Z_B}{R_{AB}} \tag{2.1.6}$$

The Hartree-Fock approximation:

Suppose that Ψ_0 (the ground state wave function) is approximated as an antisymmetrized product of N orthonormal spin orbitals $\Psi_i(\vec{x}_1)$, each a product of a spatial orbital $\Phi_k(\vec{r})$ and a spin function $\sigma(s) = \alpha(s)$ or $\beta(s)$, the Slater determinant

$$\Psi_o \approx \Psi_{HF} = \frac{1}{\sqrt{N!}}\begin{vmatrix} \Psi_1(\vec{x}_1) & \Psi_2(\vec{x}_1) & \cdots & \Psi_N(\vec{x}_1) \\ \Psi_1(\vec{x}_2) & \Psi_2(\vec{x}_2) & \cdots & \Psi_N(\vec{x}_2) \\ \vdots & \vdots & & \vdots \\ \Psi_1(\vec{x}_N) & \Psi_2(\vec{x}_N) & \cdots & \Psi_N(\vec{x}_N) \end{vmatrix} \tag{2.1.7}$$

The Hartree-Fock approximation is the method whereby the orthogonal orbitals Ψ_i are found that minimize the energy for this determinantal form of Ψ_0:

$$E_{HF} = min_{(\Psi_{HF} \to N)} E[\Psi_{HF}] \tag{2.1.8}$$

The expectation value of the Hamiltonian operator with Ψ_{HF} is given by

$$E_{HF} = \langle \Psi_{HF} | \hat{H} | \Psi_{HF} \rangle = \sum_{i=1}^{N} H_i + \frac{1}{2} \sum_{i,j=1}^{N} (J_{ij} - K_{ij}) \tag{2.1.9}$$

$$H_i \equiv \int \Psi_i^*(\vec{x}) \left[-\frac{1}{2} \nabla^2 - V_{ext}(\vec{x}) \right] \Psi_i(\vec{x}) d\vec{x} \tag{2.1.10}$$

defines the contribution due to the kinetic energy and the electron-nucleus attraction and

$$J_{ij} = \iint \Psi_i(\vec{x}_1) \Psi_i^*(\vec{x}_1) \frac{1}{r_{12}} \Psi_j^*(\vec{x}_2) \Psi_j(\vec{x}_2) d\vec{x}_1 d\vec{x}_2 \tag{2.1.11}$$

$$K_{ij} = \iint \Psi_i^*(\vec{x}_1) \Psi_j(\vec{x}_1) \frac{1}{r_{12}} \Psi_i(\vec{x}_2) \Psi_j^*(\vec{x}_2) d\vec{x}_1 d\vec{x}_2 \tag{2.1.12}$$

The integrals are all real, and $J_{ij} \geq K_{ij} \geq 0$. The J_{ij} are called Coulomb integrals, the K_{ij} are called exchange integrals. We have the property $J_{ii} = K_{ii}$. The minimization of the energy functional with the normalization conditions leads to the Hartree-Fock differential equations:

$$\hat{f} \Psi_i = \varepsilon_i \Psi_i, i = 1,2,\ldots,N \tag{2.1.13}$$

These N equations have the appearance of eigenvalue equations, where the Lagrangian multipliers are the eigenvalues of the operator $\hat{f}$. The Fock operator $\hat{f}$ is an effective one-electron operator defined as

$$\hat{f} = -\frac{1}{2} \nabla_i^2 - \sum_{A}^{M} \frac{Z_A}{r_{iA}} + V_{HF}(i) \tag{2.1.14}$$

The first two terms are the kinetic energy and the potential energy due to the electron-nucleus attraction. $V_{HF}(i)$ is the Hartree-Fock potential, the average repulsive potential experience by the i^{th} electron due to the remaining N-1 electrons, and it is given by

$$V_{HF}(\vec{x}_1) = \sum_{j}^{N} (\hat{J}_j(\vec{x}_1) - \hat{K}_j(\vec{x}_1))$$

(2.1.15)

$$\hat{J}_j(\vec{x}_1) = \int |\Psi_j(\vec{x}_2)|^2 \frac{1}{r_{12}} d\vec{x}_2 \tag{2.1.16}$$

The Coulomb operator $\hat{J}$ represents the potential that an electron at position $\vec{x}_1$ experiences due to the average charge distribution of another electron in spin orbital Ψ_j. The second term is the exchange contribution to the HF potential. It has no classical analog and it is defined through its effect when operating on a spin orbital:

$$\hat{K}_j(\vec{x}_1)\Psi_i(\vec{x}_1) = \int \Psi_j^*(\vec{x}_2) \frac{1}{r_{12}} \Psi_i(\vec{x}_2) d\vec{x}_2 \Psi_j(\vec{x}_1)$$

(2.1.17)

The HF potential is non-local and it depends on the spin orbitals. Thus, the HF equations must be solved self-consistently. The Koopman's theorem [133] provides a physical interpretation of the orbital energies: it states that the orbital energy is an approximation of minus the ionization energy associated with the removal of an electron from the orbital.

The Hohenberg-Kohn theorem:

Hohenberg-Kohn theorem considered heterogeneous electron gas, one of its core elements: The ground state of interacting multibody system is determined by the density function $\rho(r)$ of particle number. In the adiabatic approximation, it is usually described that multi-electron multibody problems correspond to the Hamiltonian H is

$$H = -\frac{\hbar^2}{2m_e} \sum_i \nabla_i^2 + \frac{1}{2} \sum_{i \neq j} \frac{e^2}{|r_i - r_j|} - \sum_{i,l} \frac{Ze^2}{|r_i - R_l|}$$

(2.1.18)

Transform H into:

$$H = T + V_{ee} + V_{ext}$$

(2.1.19)

Where T is the kinetic energy of the system, V_{ee} is Coulomb interaction between electrons, V_{ext} as an external disturbance potential.

$$T+V_{ee}=-\frac{\hbar^2}{2m_e}\sum_i \nabla_i^2+\frac{1}{2}\sum_{i\neq j}\frac{e^2}{\left|r_i-r_j\right|}$$

(2.1.20)

$$V_{ext}=\sum_i V(r_i)=\sum_i\int d^3rV(r)\delta(r-r_i)$$

(2.1.21)

Here the $V(r)$ stands for a single electron defined extraterritorial potential, it is compared with the ground state electron density $\rho(r)$ of the system.

When $V(r)$ is a given, the ground state wave function of the corresponding system can be obtained, and because $V(r)$ and $\rho(r)$ correspond to each other, so the ground state energy, the kinetic energy and electron interaction can be expressed as $E[\rho]$, $T[\rho]$ and $V_{ee}[\rho]$. In this way, we usually describe the basic variables of all the physical properties of the ground state of the multielectron system as the density of the ground state.

The second of its core contents is when the number of particles is constant, the ground state energy of system can be obtained by the energy functional $E[\rho]$ to the variation of the density function. The ground state energy (energy functional) of the system is as follows:

$$\begin{aligned}E[\rho,V]&=<\psi[\rho]\left|T+V_{ee}+V_{ext}\right|\psi[\rho]>\\&=T[\rho]+V_{ee}[\rho]+\int d^3rV(r)\rho(r)\\&=F[\rho]+\int d^3rV(r)\rho(r)\end{aligned}$$

(2.1.22)

In the upper formula, the physical quantity $F[\rho]$ varies with the ground state electron number density, is only functional of the ground state electron number density, and $F[\rho]$ is an unknown quantity,

$$F[\rho]=T[\rho]+\frac{1}{2}\iint drdr'\frac{\rho(r)\rho(r')}{\left|r-r'\right|}+E_{xc}[\rho]$$

(2.1.23)

Which $E_{xc}[\rho]$ is exchange correlation interaction, combining the particle number density function $\rho(r)$, kinetic energy $T[\rho]$ and the exchange correlation energy functional $E_{xc}[\rho]$, we can work out the ground state energy. In order to solve these quantities, the Kohn-Sham equation and the local density approximation [134] are used to solve them.

The Kohn-Sham equations:

Since the interaction between electrons, it is still not easy to solve the Schrödinger equation of the system strictly. We can only make the corresponding approximation and correction in the calculation. W. Kohn and L. J. Sham suppose that kinetic energy functional $T[\rho]$ is replaced by the particle kinetic energy functional $T_s[\rho]$, and the density function ρ is the same, Then ρ can be represented:

$$\rho(r) = \sum_{i=1}^{N} |\psi_i(r)|^2 \tag{2.1.24}$$

Where $T_s[\rho]$ is expressed as

$$T_s[\rho] = \sum_{i=1}^{N} dr\psi(r)(-\nabla^2)\psi_i(r) \tag{2.1.25}$$

And then, according to $E[\rho]$, the variation of $\rho(r)$ can be replaced by the variation of $\psi_i(r)$

$$\delta\{E[\rho(r)] - \sum_{i=1}^{N} E_i[\int dr\psi_i^*(r)\psi_i(r) - 1]\}/\delta\psi_i(r) = 0 \tag{2.1.26}$$

$$\{-\nabla^2 + V_{KS}[\rho(r)]\}\psi_i(r) = E_i\psi_i(r) \tag{2.1.27}$$

V_{KS} corresponds to the effective potential in HF equation.

$$\begin{aligned} V_{KS}[\rho(r)] &\equiv v(r) + V_{Coul}[\rho(r)] + V_{xc}[\rho(r)] \\ &= v(r) + \int dr \frac{\rho(r)}{|r - r'|} + \frac{\delta E_{xc}[\rho]}{\delta\rho(r)} \end{aligned} \tag{2.1.28}$$

Solution of the problem of $\rho(r)$ and $T[\rho]$, $V_{xc}(\rho)$ is expressed as an exchange correlation potential. We must use the local density approximation to calculate $V_{xc}(\rho)$, and then we will focus on the local density approximation.

The Local density approximation and generalized gradient approximation:

As mentioned above, the key step in density functional theory is how to select and solve the exchange correlation energy, the essence is the calculation of $V_{xc}(\rho)$. Because the theoretical functional of this paper is dependent on all density distributions, so $E_{xc}[\rho]$ is non-localized to ρ. Under the condition of very slow change of electron density space, energy density functional $g_r[\rho]$ becomes

$$g_r[\rho] = g_0[\rho(r)] + g_1[\rho(r)]\nabla\rho(r) + \ldots \tag{2.1.29}$$

Coefficient g_0 and g_1 representative electron density localization function. If we look at the first case, we get the local density approximation,

$$V_{xc}^{LDA}(r) = \frac{\delta E_{xc}^{(LDA)}[\rho]}{\delta\rho(r)} = \varepsilon_{xc}(\rho(r)) + \rho(r)\frac{d\varepsilon_{xc}(\rho(r))}{d\rho(r)} \tag{2.1.30}$$

$\varepsilon_{xc}(\rho(r))$ means the average electron gas $E_{xc}[\rho]$ by using the particle $\rho(r)$ as a function. As above, the ground state of the system can be obtained from the relation between $\varepsilon_{xc}(\rho(r))$.

According to the method of LDA approximation, the ground state energy of multibody system can be transformed into:

$$E^{LDA} = \sum_i \varepsilon_i - \frac{1}{2}\int d^3r d^3r' \rho(r)\frac{e^2}{|r-r'|}\rho(r') - \int d^3r \rho(r)\frac{d\varepsilon_{xc}(\rho(r))}{d\rho(r)}\rho(r) \tag{2.1.31}$$

The LDA approximation method is relatively uncomplicated, however, it is only used in the average electron gas, and the experiment also shows that it ignores the interaction between electrons, which makes the material research and prediction become inaccurate. With the further development of science, there are also generalized gradient approximations [135], this approximation has the following advantages: it can solve the inhomogeneous system, and the accuracy of the results is very high, because the generalized gradient approximation considers the charge density in the whole space. GGA is represented as：

$$E_{xc}^{GGA}[\rho(r)] = \int d^3r \rho(r)\varepsilon_{xc}(\rho(r)\nabla\rho(r)) \tag{2.1.32}$$

GGA has expressions such as RPBE, WC, PBEsol or PW91, in my calculations, I can choose the appropriate approximation according to the need. An Example of GGA's, exchange: PW86, B88 ("B"), PW91, correlation: LYP,

$$E_x^{B88}[\rho] = E_x^{LDA}[\rho] - \beta\rho^{1/3}\frac{x^2}{1+6\beta x\sinh^{-1}x}, x = \frac{|\nabla\rho|}{\rho^{4/3}} \tag{2.1.33}$$

GGA's improve over L(S)DA but are still not necessarily very accurate; one reason is the exchange potential doesn't necessarily have the correct qualitative behavior, B88 has the correct -1/r asymptotic behavior of the energy density but not the overall exchange potential.

The Pseudopotential plane wave method:

According to the above contents, the total energy of the corresponding system and the number of ground state particles can be obtained by solving the kohn-sham equation, and in order to converge accurately and rapidly for the system in the process of self-consistent, we must find an appropriate basis function. In specific problems, different basis functions can be used according to different objects of study, for example, the tight-binding method, pseudopotential method, affixing method and orthonormal plane wave method.

The maximum frequency pseudopotential plane wave method [136] is divided into the following categories: the first is semi-empirical model pseudopotential method, the second is empirical pseudopotential method, the third is the first principle ab initio method for modulus conservation pseudopotential calculation. The second pseudopotential is an important method for studying the electrical and optical properties of semiconductors, the first and the third pseudopotential are the most widely used self-consistent to calculate atomic pseudopotential. The model pseudopotential is local semi-empirical pseudopotential, while the modular conserved pseudopotential has no other empirical pseudopotential.

We use computer simulation to design materials. It is hoped that the force between atoms and the physical properties of the material can be achieved through the first principle method. For example, in Fig. 2.1.1 super-cell geometry, it is convenient to have periodic systems such as crystals or surfaces, but for aperiodic systems, large enough super cell is needed to separate them.

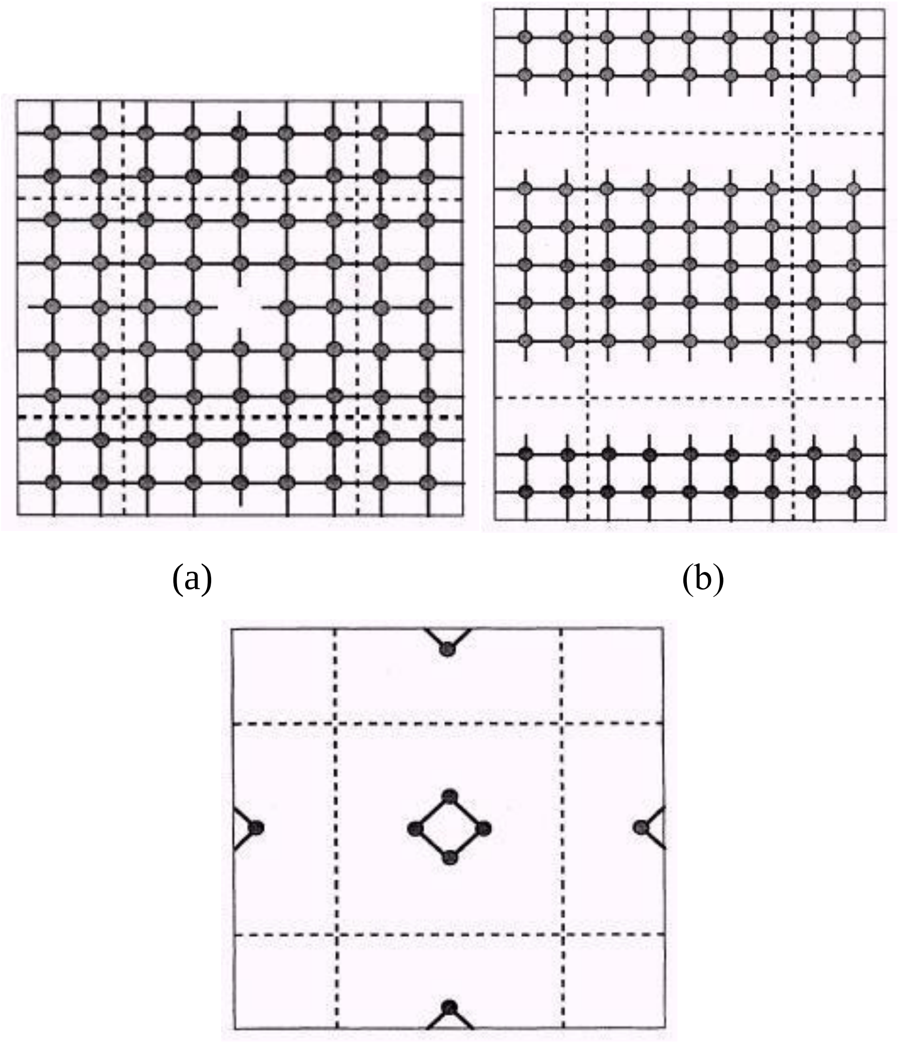

(a) (b)

(c)

Figure 2.1.1 – Schematic illustration of a supercell geometry for a vacancy in a bulk solid (a), a surface of a bulk solid (b) and a molecule (c)

Periodic boundary condition, the time independent Schrodinger equation can be written as

$$H\Psi = [T + V]\Psi = E\Psi \tag{2.1.34}$$

When the potential is periodic, such as for every translation vector *R*, the potential is invariant.

$$V(\vec{r} + \vec{R}) = V(\vec{r}) \tag{2.1.35}$$

Then the Bloch theorem tells us that the solutions of the original Schrodinger equation must satisfy the following simpler forms

$$\Psi(\vec{r}) = u(\vec{r})e^{i\vec{k}\cdot\vec{r}}$$

(2.1.36)

This is an emerging parameter, and different k leads to different solutions, so it should be fully defined as

$$\Psi_{\vec{k}}(\vec{r}) = u_{\vec{k}}(\vec{r})e^{i\vec{k}\cdot\vec{r}}$$

(2.1.37)

Where $u_{\vec{k}}(\vec{r})$ is a periodic function

$$u_{\vec{k}}(\vec{r}+\vec{R}) = u_{\vec{k}}(\vec{r})$$

(2.1.38)

The important result here is that we only need to calculate the atoms and electrons in the range of a unit cell (unit cell vector *R*). It is naturally convenient to have periodic systems such as crystals or surfaces. For aperiodic systems, large enough super cell is needed to separate them. The basic requirement of the size of super-cell is that the simulated independent object should be separated from the periodic images in other super-cell without the interaction and non-physical results.

So we just have to solve the part $u_{\vec{k}}(\vec{r})$ of super-cell wave function $\Psi_{\vec{k}}(\vec{r}) = u_{\vec{k}}(\vec{r})e^{i\vec{k}\cdot\vec{r}}$, because $u_{\vec{k}}(\vec{r})$ is a periodic function, it can be easily expanded by Fourier series,

$$u_{\vec{k}}(\vec{r}) = \sum_{G} C_{KG}e^{i\vec{G}\vec{r}}$$

(2.1.39)

it only takes a few base functions to reproduce the features of the original function. In general, the demand for the number of plane-wave bases is determined by the pseudopotential of the simulated object.

In this work, calculations were performed within the framework of the density functional theory by using the plane-wave pseudopotential approach in the

Cambridge Sequential Total Energy Package codes [100]. We used the generalized gradient approximation of Perdew-Burke-Ernzerhof scheme to describe the exchange-correlation potential [142]. Energy cutoff of plane-wave was set to be 450 eV, the tolerances for geometry optimization were set as the difference in total energy within 1 × 10^{-6} eV/atom. For all systems under study, the following procedure was followed: building a model, choosing parameters for optimization, calculating and analyzing properties.

2.2 Calculation of optical properties by first-principle methods

Optical properties such as the reflectivity, absorption, refractive index, dielectric function, conductivity and loss function have been widely studied. The dielectric function with the optical constant, imaginary part and the real part, can obtain the relation of the reflection, refraction, the coefficient of absorption and dispersion of light. We can also analyze the macroscopic optical response function of solid by complex dielectric constant, but only under the condition of linear response which is defined as

$$\varepsilon(\omega) = \varepsilon_1(\omega) + i\varepsilon_2(\omega) \tag{2.2.1}$$

According to the superposition and causality correlation principle, the Kramers-Kronig relations between the real part ε_1 and the imaginary part ε_2 of the dielectric function are expressed as [137]:

$$\varepsilon_1(\omega) = 1 + \frac{2}{\pi}\int_0^\infty \frac{\omega'\varepsilon_2(\omega')}{\omega'^2 - \omega^2} d\omega' \tag{2.2.2}$$

$$\varepsilon_2(\omega) = -\frac{2\omega}{\pi}\int_0^\infty \frac{\varepsilon_1(\omega')}{\omega'^2 - \omega^2} d\omega' \tag{2.2.3}$$

The formula can be used to investigate the band structure and optical properties of the crystal where ω is angular frequency, thus, when the information on ε_2 of the dielectric function is known, the ε_1 of the dielectric function can be calculated using equation. The complex dielectric function is widely used to study the optical properties of materials; the ε_1 and ε_2 of dielectric function are described as follows

$$\begin{aligned}\varepsilon_1(\omega) &= n^2(\omega) - k^2(\omega)\\ \varepsilon_2(\omega) &= 2n(\omega)k(\omega)\end{aligned} \tag{2.2.4}$$

or

$$\begin{aligned}n(\omega) &= \frac{1}{\sqrt{2}}[(\varepsilon_1^2(\omega)+\varepsilon_2^2(\omega))^{1/2}+\varepsilon_1(\omega)]^{1/2}\\ k(\omega) &= \frac{1}{\sqrt{2}}[(\varepsilon_1^2(\omega)+\varepsilon_2^2(\omega))^{1/2}-\varepsilon_1(\omega)]^{1/2}\end{aligned} \tag{2.2.5}$$

$n(\omega)$ is refractive index, $k(\omega)$ is extinction coefficient, it refers to the standard terms of reflection, refraction and absorption of semiconductor, once determined the real part ε_1 and the imaginary part ε_2 of the dielectric function, the optical constants n and k can be calculated.

A bundle of monochromatic light was irradiated onto the surface of an absorbing medium. After passing through a medium of a certain thickness, the intensity of the transmitted light was weakened because the medium absorbed a part of the light energy. Optical properties were simulated further by the formulas:

$$I = I_0 e^{-\alpha x} \tag{2.2.6}$$

where I is the intensity of transmitted light, I_0 is the intensity of incident light, α is the absorption coefficient, and x is the thickness of the absorbent medium.

2.3 Accounting for weak interactions in first-principle calculations

In chemistry and physics, density functional theory is widely used quantum chemical method for electronic structure calculations, accurate calculations are important for density functional theory because weak intermolecular forces, such as London dispersion force and hydrogen bond, such interactions have different physical origins: the electrostatic, exchange-repulsion, charge-transfer, induction, and dispersion interactions, although all of them can ultimately be attributed to the Coulomb interaction between electrons and nuclei constituting a system[138], however, a general drawback of all common GGA functionals can not describe long-range electron correlations that are responsible for van der Waals forces[139], then the vdW interactions between atoms and molecules play an important role in determining the structure and energy of chemical species.

Van der Waals forces is the attraction of intermolecular forces between molecules. The electron charge density is defined as an electron of an atom is in a certain area in the electron cloud at a specific time, there is no way to know exactly where the electron is located, they are not in the same area 100% of the time, a dipole is formed momentarily when the electrons all go to the same area. Although a molecule is nonpolar, the displacement of electrons makes a nonpolar molecule to be polar for a moment, the molecule is polar, all electrons are concentrated at one end, the molecule is partially negatively charged on that end. The negative end makes the surrounding molecules have an instantaneous dipole to attract the positive of surrounding molecules, this process is called the London Dispersion Force of attraction. Because of the forces of attraction between the electrons and protons in the nucleus are weaker, it is easier to displace the electrons it means the molecule is also more polarizable.

The Van der Waals equation is

$$(P+\frac{n^2a}{V^2})(V-nb)=nRT \tag{2.3.1}$$

Where P is pressure, V is the volume of gas, in moles *n*. The intermolecular forces of attraction is incorporated into the equation with the $\frac{n^2a}{V^2}$ term, here *a* is a specific value of a particular gas. The variable *b* is the eliminated volume per mole, which accounts for the volume of gas molecules. R is a known constant, 0.08206 L atm mol^{-1} K^{-1}, T represents temperature.

Such as non-ideal (real) gases, which is used Van der Waals equation to calculate an actual value. The van der Waals equation takes into account and corrects for the volume of participating molecules and the intermolecular forces of attraction.

Taking into account weak interactions, however, the traditional exchange correlation function cannot accurately describe van der Waals, so van der Waals correction is very necessary. The dispersion correction in the functional we use a modified version of the approach [140]. The total energy is $E_{DFT-D}=E_{KS-DFT}+E_{disp}$,

E_{KS-DFT} is the usual self-consistent Kohn-Sham energy as obtained from chosen density functional, E_{disp} is the empirical dispersion correction[141]

$$E_{disp} = -s_6 \sum_{i=1}^{N_{at}-1} \sum_{j=i+1}^{N_{at}} \frac{C_6^{ij}}{R_{ij}^6} f_{dmp}(R_{ij}) \tag{2.3.2}$$

Where s_6 is a global scaling factor depends on the density functional used, N_{at} is the number of atoms in system, C_6^{ij} is the dispersion coefficient for atom pair *ij*, R_{ij} is an interatomic distance, a damping function f_{dmp} is given by $f_{dmp}(R_{ij}) = \frac{1}{1+e^{-d(R_{ij}/R_r-1)}}$, where R_r is the sum of atomic vdW radii. Density functional theory calculations with van de Waals corrections is utilized to study the geometric and electronic properties, this means stable structures are formed by weak interactions, weak interaction can not only assemble different two-dimensional materials, but also effectively adjust the electronic properties of materials.

2.4 Surface modeling in first-principle calculations (Surface as a model for describing nanoparticles larger than 10 nm).

Theoretical simulations are usually based on the Density functional theory, for the technical choices such as exchange-correlation functional, and numerical algorithms to solve the Kohn–Sham equations, they are determined the accuracy and efficiency of Density functional theory-based methods. The local density approximation used in bulk or surface systems, that the exchange-correlation energy describes a homogeneous electron gas of the same density, while the generalized gradient approximation, there exchange-correlation energy not only depends on the electron density but also on its local gradient, it solves the over binding of the local density approximation.

Material simulations have become powerful tools for engineers and scientists. Modeling the structure of nanoparticle has different sizes, the total number of atoms is truly represented through the first-principles approach, the similar size and number of atoms can be different in shape, that correspond with different volume/surface ratios, various crystallographic surfaces (such as (001), (111)) and varied amounts of topological defects of the surface (steps, adatoms). For the modeling of the surface, at the first step we calculated the lattice parameters of bulk. The second step is building of a slab by increasing the lattice parameter along c crystal axis. For the correct modelling of the surface considering a slab of at least 6 layers within periodic boundary conditions are necessary. In this case the number of internal layers (four) is twice more than surface layers (two). At the next step we calculated adsorption energy as the difference between the energies of two optimized configurations (i) when molecule initially placed in vicinity of the surface (usually 0.25 nm) and (ii) when molecule remotes from the surface at about 0.5 nm. Atomic structure of the surface of nanoparticles is rather similar to the bulk and therefore models of bulk and surface can be used for the modelling of large nanoparticles.

2.5 Conclusion

Density functional theory is a very active research direction. Increasingly accurate exchange-related energy functional approximations are being continuously developed. The density functional theory is presently the most successfull approach to compute the electronic structure of matter. It provides us with a relatively efficient and unbiased tool with which to compute the ground state energy in realistic models of bulk materials and their surfaces. Density functional theory has been generalized to deal with many different situations: spin polarized systems, multicomponent systems such as nuclei and electron hole droplets, free energy at finite temperatures, superconductors with electronic pairing mechanisms, relativistic electrons, time-dependent phenomena and excited states, bosons, molecular dynamics, etc. From physics, chemistry, life sciences to emerging nanomaterials science, density functionals are becoming a standard research tool. By working with the density, density functional theory reaches a good balance between efficiency and accuracy. It is widely used in electronic structure calculations and other field in condensed matter physics.

CHAPTER 3. INVESTIGATION OF THE EFFECT OF DEFECTS ON THE ELECTRONIC STRUCTURE AND OPTICAL PROPERTIES OF MATERIALS BY THE EXAMPLE OF BERYLLIUM IMPURITIES IN ZINC OXIDE

We make this work for learn how impurities influence atomic structure and physical properties in bulk crystal for further do the same for nano-systems. The nanostructured materials have attracted much attention because of their unique optical, magnetic, semiconducting properties and potential applications. Zinc oxide has a polar surface that can form a wide range of nanostructures, in the one-dimensional oxide nano-systems, it is one of the most promising materials for fabrication optoelectronic devices, the nanostructure of zinc oxide has high catalytic efficiency and strong adsorption ability. We used first-principles calculations, chose ZnBeO as a model system, got $Be_xZn_{1-x}O$ with different component of impurities (x=0, 0.125, 0.25, 0.375, 0.5, 0.625, 0.75, 0.875, 1) by changing the amount of Be to replace Zn in the supercell. After structures optimization, we obtained the lattice constants for the stable structures of $Be_xZn_{1-x}O$ with different component of impurities, then the electronic structures and optical properties of $Be_xZn_{1-x}O$ were studied.

At the present calculations, the special points sampling integration over the Brillouin zone were performed using a k-mesh of dimensions 4×4×4 k-points mesh according to a Monkhorst–Pack scheme [143], we selected Be $2s^2$, Zn $3d^{10}4s^2$, O $2s^22p^4$ configuration as the valence states and the basic model was wurtzite ZnO, supercell 2 × 2 × 1 used in the calculations are shown in Fig. 3.1.

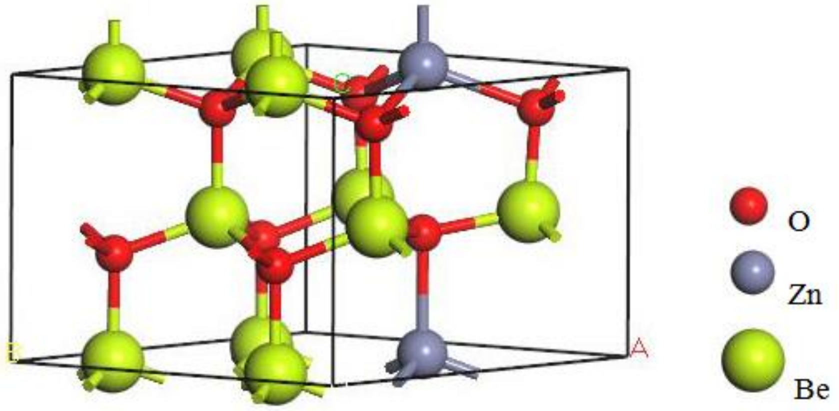

Figure 3.1 – The crystal structure of wurtzite $Be_{0.875}Zn_{0.125}O$ alloys.

The optical properties of the $Be_xZn_{1-x}O$ ternary mixed crystal

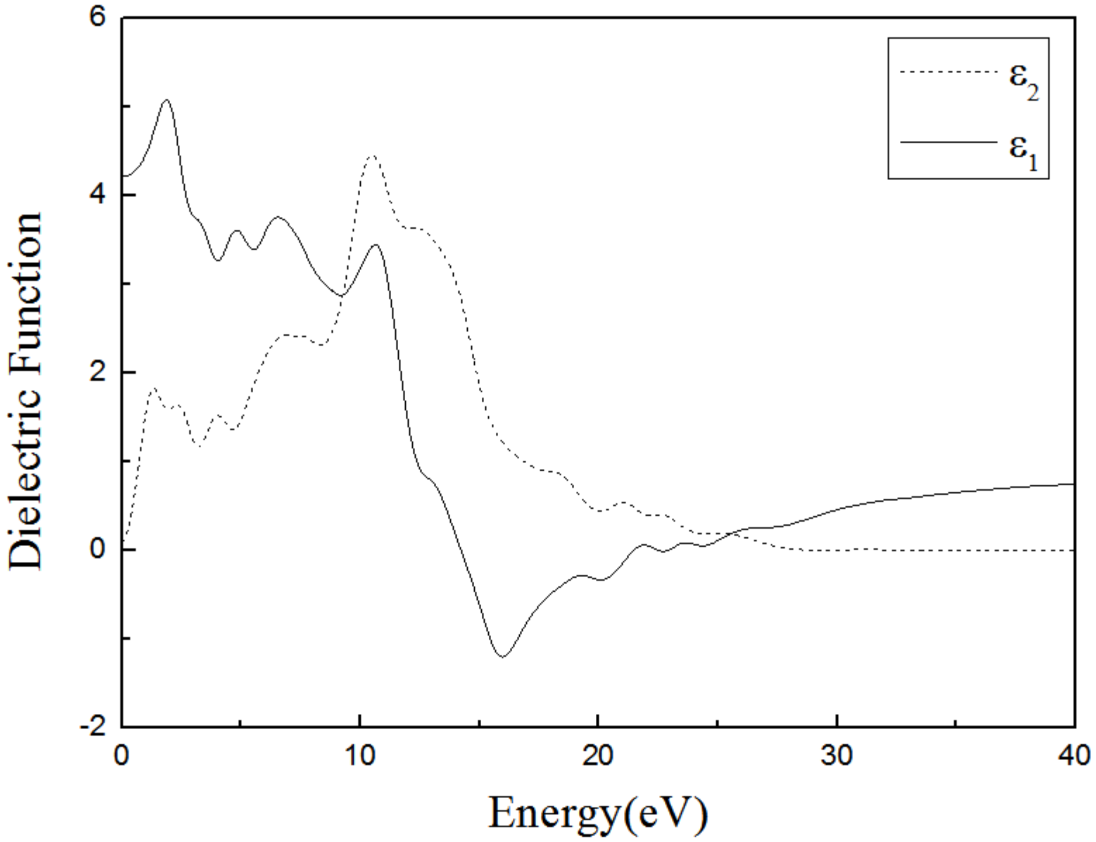

Figure 3.2 – The dielectric function of wurtzite ZnO.

In Fig. 3.2 are report the relationship between the dielectric function of wurtzite ZnO and photon energy. When the energy is 0 eV, the static dielectric constant is 4.22, which is consistent with the experimental value of 4.00 [144]. In Fig. 3.2, it is seen that there are three peaks for ε_2 of dielectric function: the energy of the first peak I1 is about 1.38 eV, it mainly goes through from the valence band at O 2p states to the bottom of conduction band at Zn 4s states. The energy of the second peak I2 is about 6.76 eV; the transition occurs between the 3d orbit of Zn and 2p orbit of O. The energy of the third peak I3 is about 10.47 eV, it corresponds to the transition between the 3d orbit of Zn and the 2 s orbit of O.

The change in the refractive index function is related to the type of media via an electromagnetic wave. The relationship between the refractive index of wurtzite ZnO and photon energy are shown in Fig. 3.3. When the energy is 0 eV, the refractive index of ZnO becomes n_0=2.05; it is comparable to the experimental value of 2.009 [145]. At low energy region, the huge difference between n and k exist. In contrast, n is constant at high energy region where k is almost equal to zero. ZnO has less absorption of high-frequency electromagnetic waves.

As we can see from the Fig. 3.4, the absorption intensity of wurtzite ZnO is mainly concentrated in the bandwidth of 29.85-1931.86 nm where the strongest absorption nearby $x \sim 85.45$ nm. The absorption of BeO is mainly concentrated in the bandwidth of 32.71-457.98 nm. The strongest absorption is observed at $x \sim 102.01$ nm.

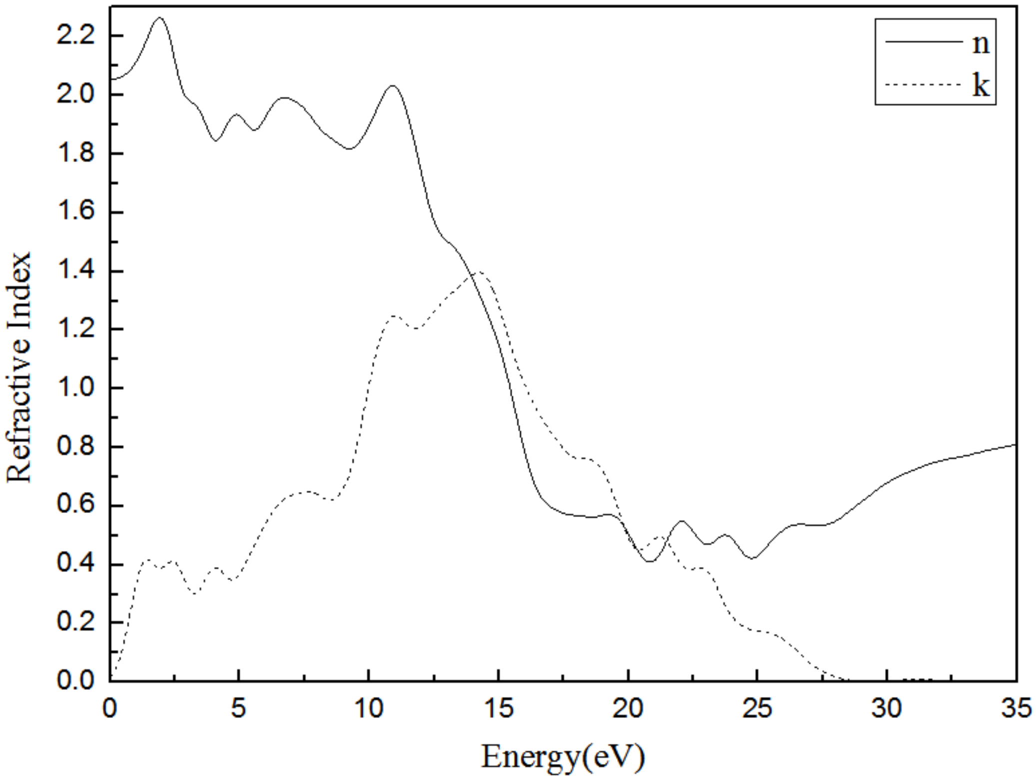

Figure 3.3 – The refractive index of wurtzite ZnO.

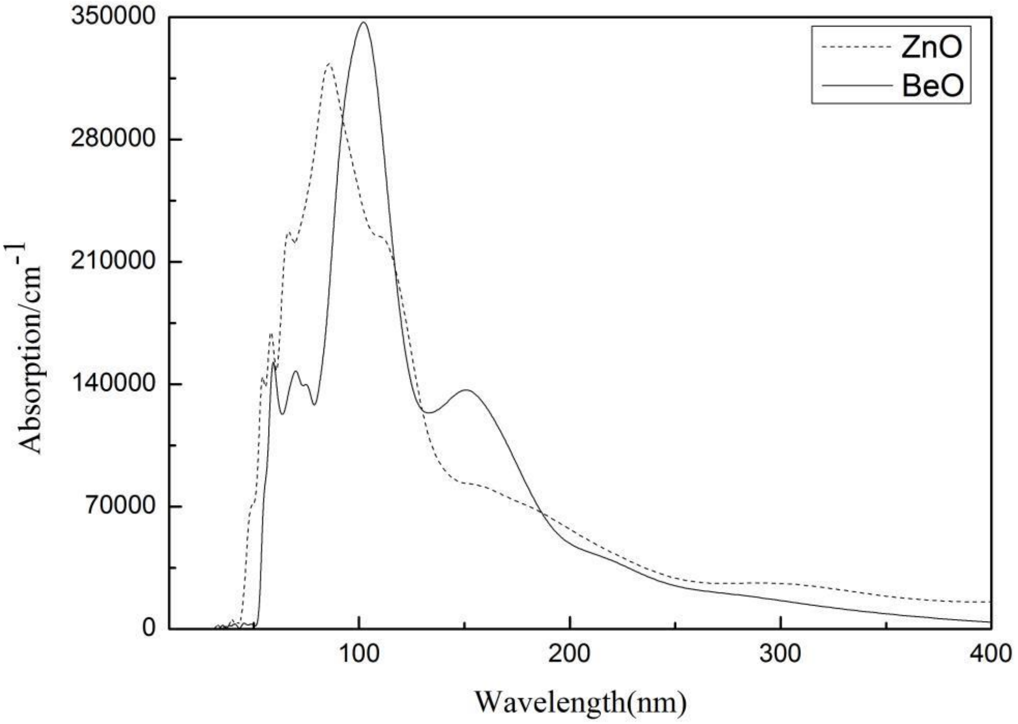

Figure 3.4 – The absorption function of wurtzite ZnO and BeO.

We know that the dielectric function can reflect band structure and spectrum of $Be_xZn_{1-x}O$ ternary mixed crystal. On Fig. 3.5 displayed the relation of dielectric function and photon energy, the real part ε_1 and imaginary part ε_2 of the dielectric function of $Be_xZn_{1-x}O$ ($x = 0.125, 0.375, 0.625, 0.75, 0.875$) are calculated. Based on Fig. 3.5, one can see that as the energy increases the real part ε_1 of the dielectric function of $Be_xZn_{1-x}O$ first reach a maximum peak and then gradually attenuated. The static dielectric constant of $Be_xZn_{1-x}O$ decreases as the Be component increases.

Before we discussed the wider band gap as the composition increases, it requires the high-energy electrons undergo transition and the decrease of static dielectric constant, which is consistent with our calculation. The imaginary part ε_2 of the dielectric function represents the absorption of light. As the Be concentration increases, the three main peaks are constantly moving towards the high energy tail.

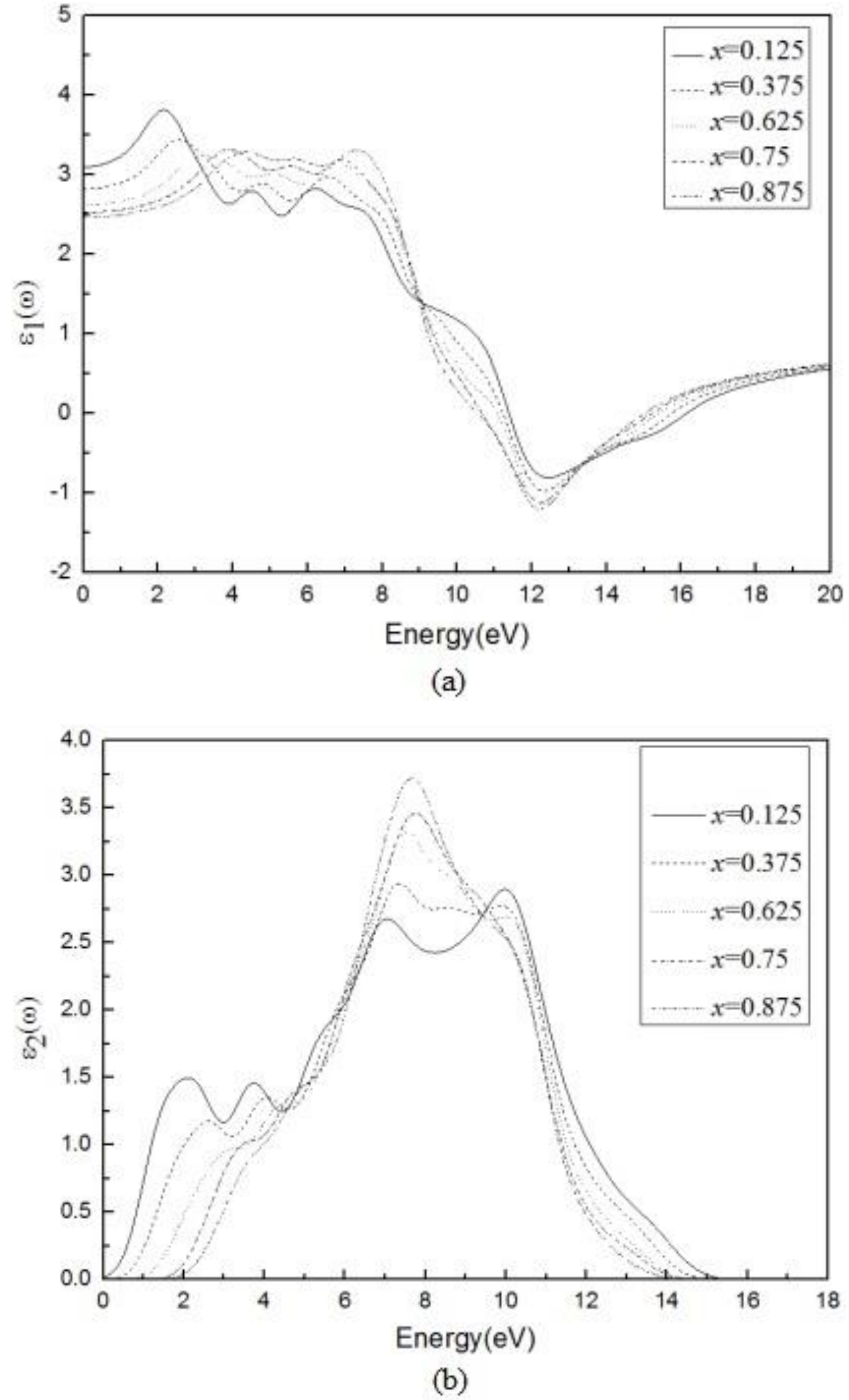

Figure 3.5 – The real part ε_1 (a) and imaginary part ε_2 (b) of the dielectric function of $Be_xZn_{1-x}O$.

Refractive index is related to the interaction of microscopic atoms; it's the most important physical parameter. The refractive index will be interpreted to the density and the local polarizability of these entities. Fig. 3.6 shows the relationship between the real part of the refractive index and the energy of $Be_xZn_{1-x}O$ ternary mixed crystal. When the energy is 0 eV, the refractive index of $Be_xZn_{1-x}O$ decreases as the Be component increases, the refractive index of $Be_xZn_{1-x}O$ and ZnO is different. The relation of the reflectivity and the energy of $Be_xZn_{1-x}O$ ternary mixed crystal are illustrated in Fig. 3.7. We have observed that when the energy is 0 eV, the reflectivity decreases as the Be concentration increases, the energy is gradually increasing in the high energy region. The reflectance spectrum at the high-energy region decreases rapidly as the photon energy increases. On Fig. 3.8 shows the absorption of $Be_xZn_{1-x}O$ ternary mixed crystal. The band gap of $Be_xZn_{1-x}O$ increases with x. The excitation energy required for the electron being excited from valence band edge to conduction band edge. The stronger excitation produces the blue-shift of optical absorption. We can see clearly from Fig. 3.8, the blue shift of absorption spectrum of the system becomes more obvious after increasing x. Our results agree with experiment [146].

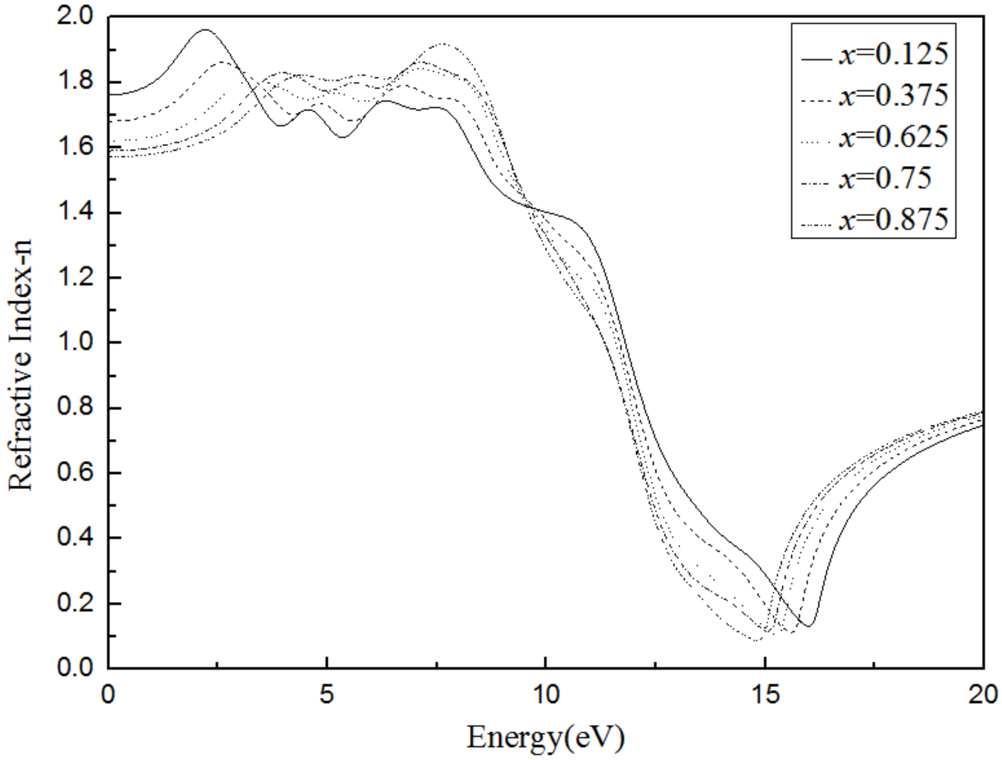

Figure 3.6 – The refractive index (n)of $Be_xZn_{1-x}O$.

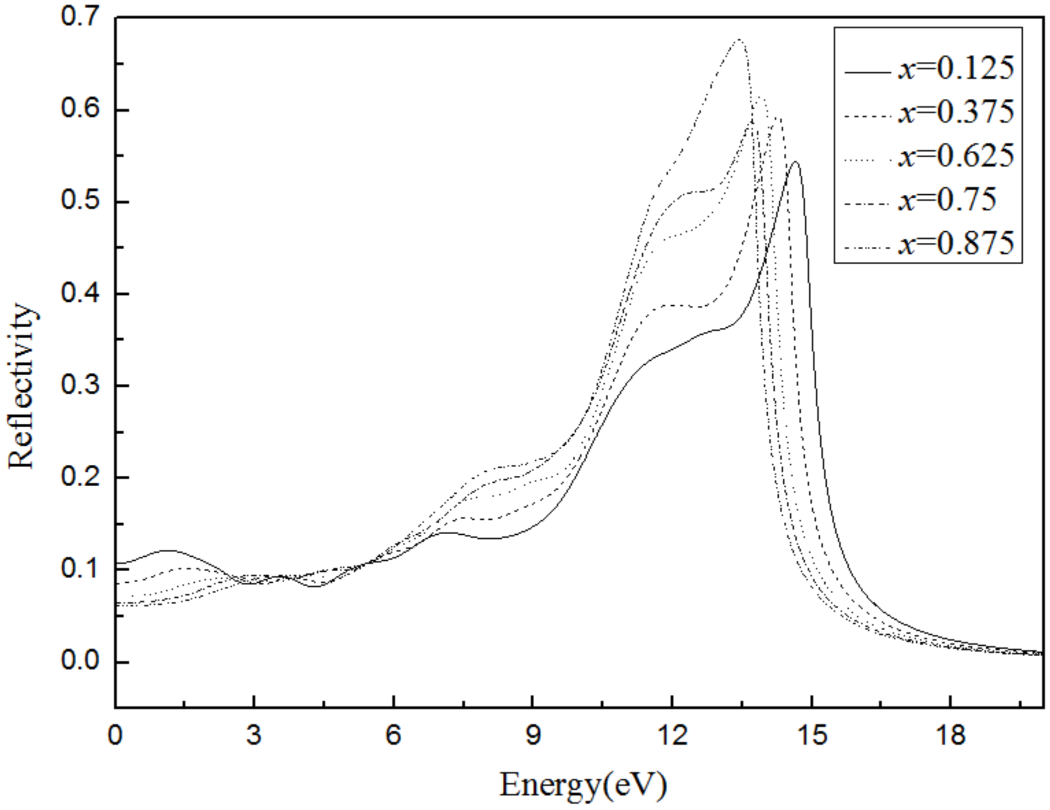

Figure 3.7 – The reflectivity of $Be_xZn_{1-x}O$.

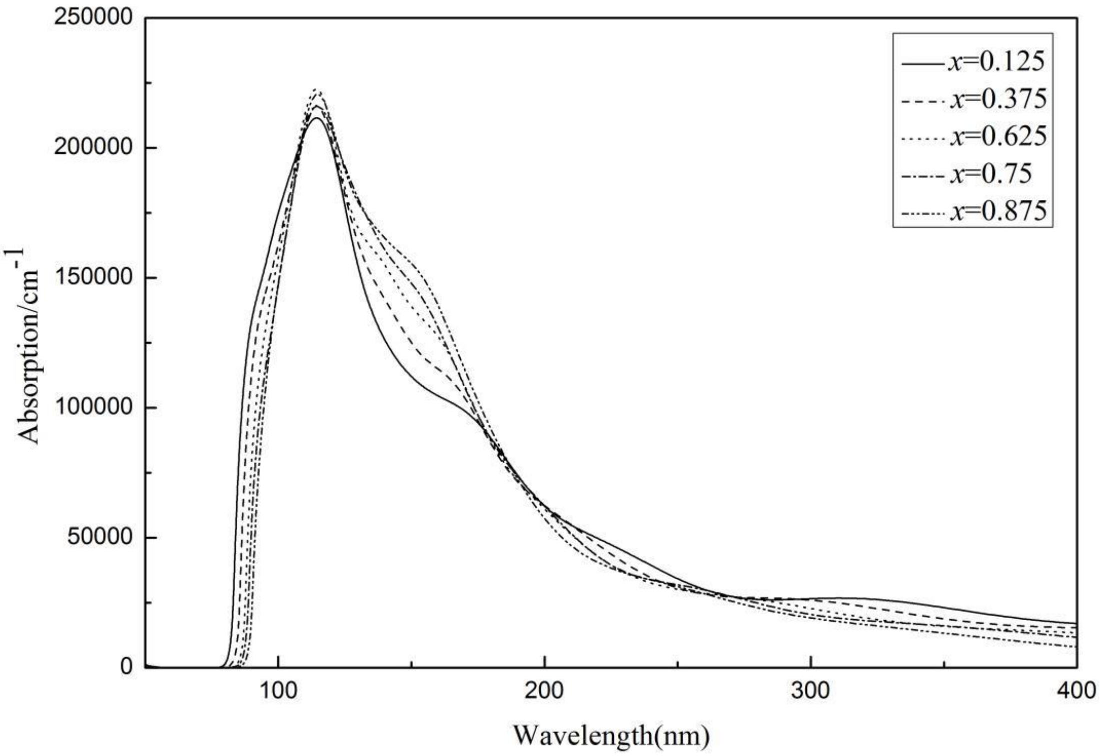

Figure 3.8 – The absorption function of $Be_xZn_{1-x}O$.

Lattice parameters

Table 3.1 – Calculated lattice parameter a and c for $Be_xZn_{1-x}O$ ternary mixed crystal. Compared with other theoretical calculations and experimental results.

x	Lattice parameter a (nm)		Lattice parameter c (Å)		
	This work	Theoretical[a]	This work	Exp.[b]	Theoretical[a]
0	0.3290	0.3256	5.29	5.20	5.26
0.1				5.11	
0.125	0.3215	0.3190	5.20		5.15
0.25	0.3134	0.3134	5.13		5.08
0.375	0.3083	0.3052	5.06		5.02
0.5	0.3020	0.2972	4.84		4.99
0.6				4.79	
0.625	0.2975	0.2924	4.78		4.83
0.7				4.71	
0.75	0.2891	0.2889	4.68		4.68
0.8				4.61	
0.875	0.2823	0.2808	4.59		4.56
1	0.2753	0.2764	4.47	4.38	4.49

[a]Ref.[147]. [b]Ref.[57].

After the structure optimization, the lattice parameters of $Be_xZn_{1-x}O$ ternary mixed crystal have been calculated, table 3.1 show that our calculated compared with other theoretical and experimental, our results are in agreement with them. Fig. 3.9 show us the lattice parameters decrease linearly as Be doping concentration increases, the result compliance with Vegard's law [148] and consistent with experimental results [57], then fitting the results, we get the linear equation as follow,

$$a = 0.328 - 0.052x$$
$$c = 5.313 - 0.839x$$

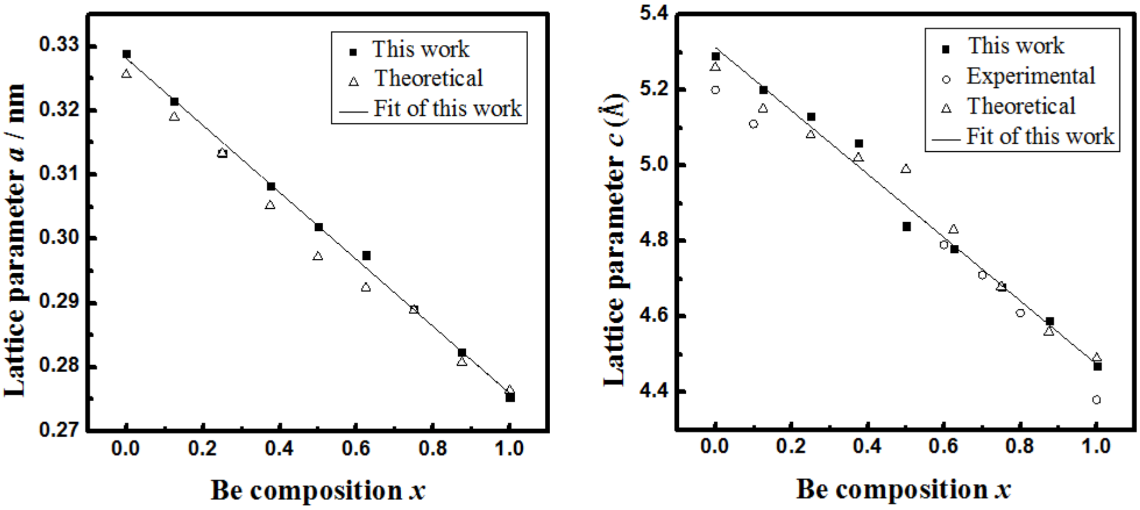

Figure 3.9 – The Lattice parameters of $Be_xZn_{1-x}O$ with different Be concentrations.

Density of states

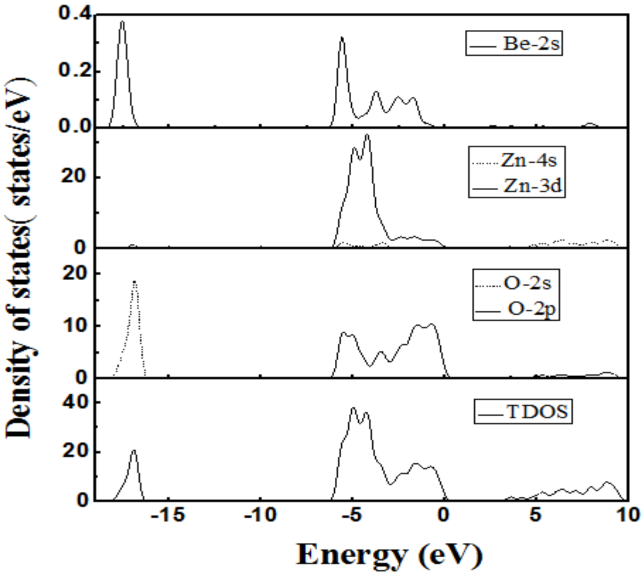

Figure 3.10 – Total and partial density of states for $Be_{0.25}Zn_{0.75}O$.

The partial and total density of states for $Be_xZn_{1-x}O$ are calculated, Fig. 3.10 shows the total and partial DOS for the$Be_{0.25}Zn_{0.75}O$, as an example. The results shown that the valence band maximum occupied by O 2p states, and the conduction band minimum occupied by Zn 4s states. From Fig. 3.11, as Be doping, the contribution of zinc and beryllium in the conduction band position constantly moving to higher energy region, density of states strength Zn 4s states with decreasing proportion of Zn is constantly reduced, density of states strength Be 2s states with increasing proportion of Be is constantly increased, make the band gap width of $Be_xZn_{1-x}O$ increases.

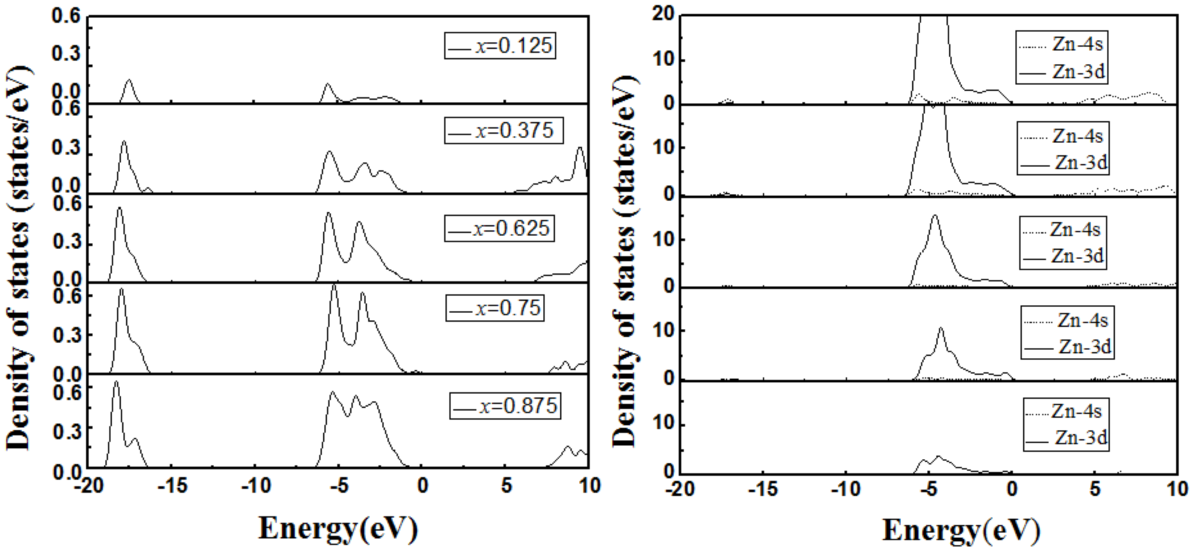

(a) (b)

Figure 3.11 – a, b Beryllium and zinc PDOS of different components

The band structure of the $Be_xZn_{1-x}O$ ternary mixed crystal

$Be_xZn_{1-x}O$ ternary mixed crystal has been widely used in photoelectric devices and also has requirements for band gap. According to the optimized lattice constant, the band structure of $Be_{0.125}Zn_{0.875}O$ and $Be_{0.875}Zn_{0.125}O$ ternary mixed crystal has been calculated. In Fig. 3.12, it is clearly seen that the conduction band and valence band are respectively in the above and below of Fermi level, the top of valence band and the bottom of conduction band are also at the same Γ point, it is indicated that the $Be_{0.125}Zn_{0.875}O$ and $Be_{0.875}Zn_{0.125}O$ ternary mixed crystal are direct band-gap semiconductors. With the increase of Be doping, the lattice structure has changed, the conduction band is constantly moving toward the high-energy tail, the band gap of $Be_xZn_{1-x}O$ ternary mixed crystal increase as the component of Be increases. Despite the changes in the local atomic structure of BeZnO systems caused by a mismatch of ionic radii of Be Zn (0.27 and 0.6 Å respectively) remain direct gap semiconductor. This explains the smoothness of the varying of the optical properties.

Another effect of Be-doping is the change of the number of the states in the conductive band caused by the difference in the energetics of the orbitals in Zn and Be that provides changes the number of optical transitions that provide the smooth shortening of the tail in absorption function (see Fig. 3.8).

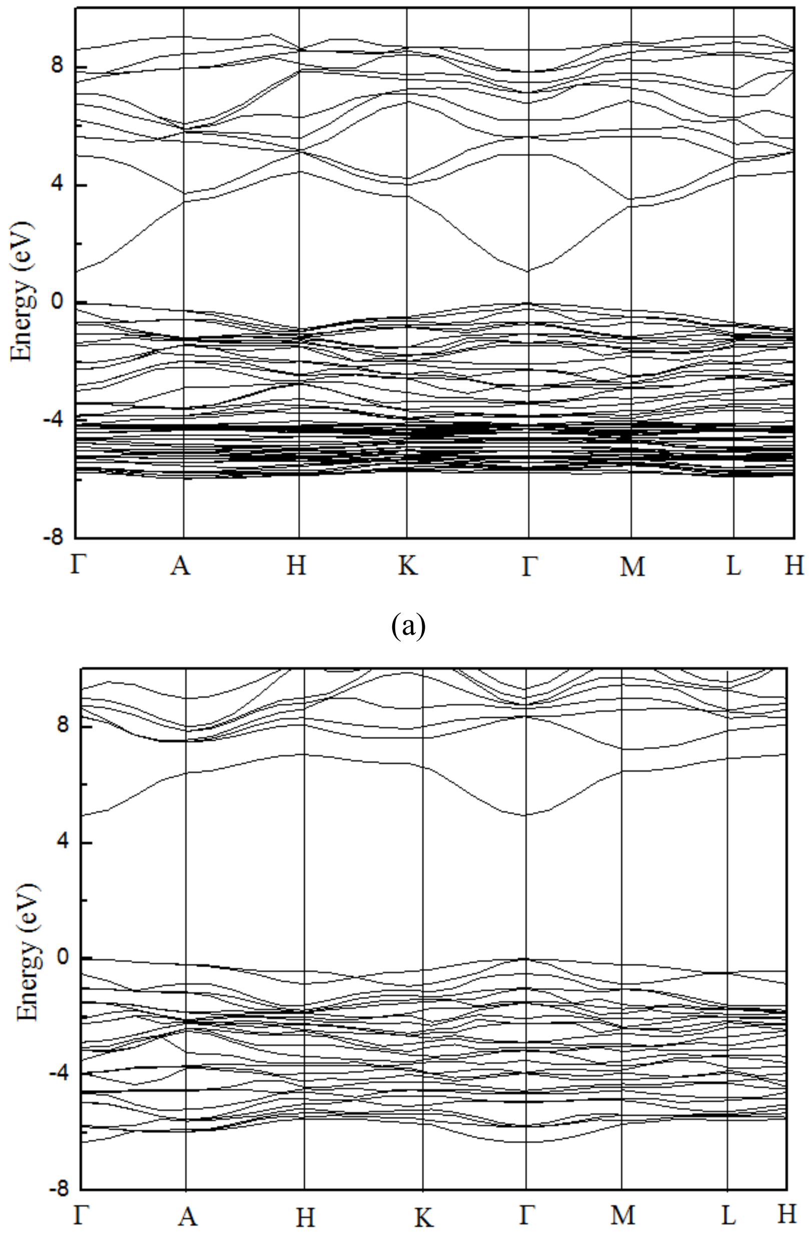

(a)

(b)

Figure 3.12 – The energy band of wurtzite $Be_{0.125}Zn_{0.875}O$ (a) and $Be_{0.875}Zn_{0.125}O$ (b)

Table 3.2 – Band gap Eg and correction Band gap Eg for $Be_xZn_{1-x}O$ ternary mixed crystal. Compared with other theoretical calculations and experimental results.

E_g (eV)

	This work	Theoretical [a]	Correctional	Experimental [b]
x				
0	0.734	0.972	3.3000	3.37
0.1				3.53
0.125	1.083	1.325	3.7777	
0.25	1.568	1.645	4.3913	
0.375	1.816	2.058	4.7679	
0.44				4.63
0.5	2.463	2.381	5.5435	
0.59				4.74
0.6				5.01
0.625	3.041	3.076	6.2502	
0.68				5.45
0.75	4.192	3.799	7.5298	
0.875	4.943	5.236	8.4094	
1	7.004	7.322	10.600	10.60

[a]Ref.[147]. [b]Ref.[57].

The band gap of $Be_xZn_{1-x}O$ ternary mixed crystal is increases with increasing Be concentrations, but our calculated is smaller than experimental, because of the semiconductor based on DFT of GGA exchange-correlation effects between electrons and electron handle deficiency caused errors, but in the same environment, changing the doping concentration for the same structure system material research, the band gap was calculated by DFT is still meaningful. In order to close to the experimental value, Band gap value has been corrected, using the formula[149],

$$E^{cor}_{g,Be_xZn_{1-x}O} = E^{cal}_{g,Be_xZn_{1-x}O} + (1-x)\cdot\Delta E_{ZnO} + x\cdot\Delta E_{BeO}$$

$E^{cor}_{g,Be_xZn_{1-x}O}$ is correction band gap of $Be_xZn_{1-x}O$, $E^{cal}_{g,Be_xZn_{1-x}O}$ is calculation band gap of $Be_xZn_{1-x}O$, x is concentration of Be, ΔE_{ZnO} is experimental band gap minus calculated band gap of ZnO, ΔE_{BeO} is experimental band gap minus calculated band gap of BeO. Correction parameters are experimental of ZnO 3.3eV and experimental of BeO

10.6eV, table 3.2 and Fig. 3.13 shown our calculated compared with experimental and our calculated results are consistent with experimental results, in Fig. 3.13 we used the quadratic function shown band gap of $Be_xZn_{1-x}O$ ternary mixed crystal, the solid line is a fit of our calculation data using the quadratic function, as follow,

$$E_g = 3.491 + 1.173x + 5.608x^2$$

and the dotted line is a fit of experimental [150], the formular is

$$E_g = 3.4 - 2.1x + 9.3x^2$$

and our calculated is consistent with experimental.

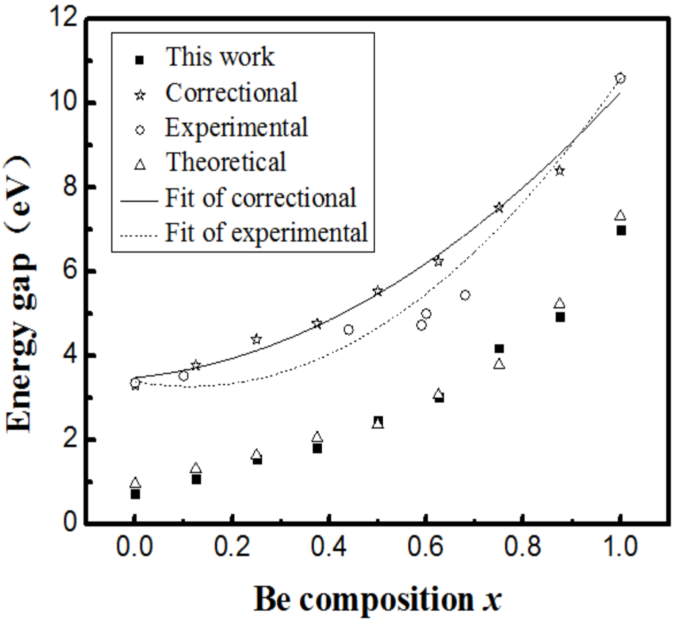

Figure 3.13 – Calculated the Band gap of $Be_xZn_{1-x}O$ ternary mixed crystal for different Be concentrations.

Conclusion

We have used the first-principle calculations to study the electronic structures and optical properties of $Be_xZn_{1-x}O$ ternary mixed crystals. The structural parameters of $Be_xZn_{1-x}O$ ternary mixed crystals have been optimized. The results show that lattice parameters are almost linearly and obey the Vegard's law. After correction the electronic band gap is consistent with experimental results. The results of the density of states for $Be_xZn_{1-x}O$ show that as Be doping the contribution of zinc and beryllium in the conduction band position constantly moving to higher energy region, make the band gap width of $Be_xZn_{1-x}O$ increases. At as the energy increases the real part

ε_1 of the dielectric function of $Be_xZn_{1-x}O$ first reach a maximum peak and then gradually weakened, the static dielectric constant of $Be_xZn_{1-x}O$ decreases as the Be component increases. The imaginary part ε_2 of the dielectric function as the Be component increases, the three main peaks are constantly shifted to the high-energy tail. The refractive index and reflectivity of $Be_xZn_{1-x}O$ ternary mixed crystal are decreases with increasing Be concentrations. The reflectance spectrum at the high energy region decreases rapidly as the photon energy increases. The blue shift of absorption spectrum of the system becomes more pronounced after increasing the concentration of Be. A key factor influencing the change in the optical properties of the $Be_xZn_{1-x}O$ system is a change in the lattice parameters due to a change in the impurity concentration. In the lattice of actual crystals, not every equilibrium position is occupied by atoms, and there are always a few positions that are empty. Due to the appearance of vacancies, the atoms around them deviate from the equilibrium position and lattice distortion occurs. Formation of a vacancy leads to missing bonds and distortion of the lattice. [151] For the surface formation, some bonds of the surface atoms are broken, the remaining atoms change the length of the bond to adapt to the new environment. Changes of the symmetry at the surface are reflected by corresponding changes in the crystal lattice. The interference of distortions of lattice originating at the terminal surfaces leads to changes of symmetry of the lattice. [152, 153] Nanostructured materials exhibit many excellent physical properties, which are different from traditional polycrystalline materials. These unique properties are usually attributed to the small grain size leading to a significant increase in grain boundary density. W Qin described the grain size dependence of the crystal lattice distortion of nanostructured materials. [154]

CHAPTER 4. INVESTIGATION OF THE ELECTRONIC STRUCTURE, CHEMICAL ACTIVITY AND OPTICAL PROPERTIES OF β-C_3N_4

We make this work for studies of the electronic and optical properties of ideal and lightly disordered bulk C_3N_4, check the role of the surface and defects, and discuss chemical stability of the surface and nanoclusters of carbonitride. Carbonitride is currently considered as a prospective material for various applications, such as photocatalysts, fuel cell electrodes, light-emitting equipment, chemical sensors and other devices. In some works, only the systems with perfect crystal structure were considered, we also require consideration of the surface and nano-phases of carbonitride. Taking into account effect of disorder, surface, and defects is the further logical step toward understanding electronic structure and optical properties of realistic carbonitride structures. We demonstrate significant sensitivity of absorption spectra of β-C_3N_4 to any kinds of disorder in atomic structure. Formation and passivation of the surface provides similar changes in optical properties. The value of the indirect bandgap depends on the chemical structure of the surface. Functionalization of the active sites on the surface by monovalent species (hydrogen and fluorine) leads to vanishing of the bandgap in the case of (001) surface and changes the value of the bandgap in the case of nanoclusters. Results of our calculations also demonstrate the appearance of magnetic moments in hydrogenated and fluorinated (001) surface of β-C_3N_4.

4.1 Description of the crystal structure and the effect of disordering on the electronic structure and optical properties

At the present calculations, we selected C $2s^22p^4$, N $2s^22p^4$ configuration as the valence states. The special points sampling integration over the Brillouin zone was performed using a k-mesh of dimensions 2 × 2 × 2 k-points mesh according to a Monkhorst–Pack scheme. Calculated non spin-polarized densities of states were smeared employing Gaussian function of half-width with half-height 0.2 eV and spin-polarized with 0.02 eV. The basic model of bulk C_3N_4 was shown. Supercell 2 × 2 × 2 (Fig. 4.1.1) of 224 atoms was used for the modelling of disorder and vacancies in bulk.

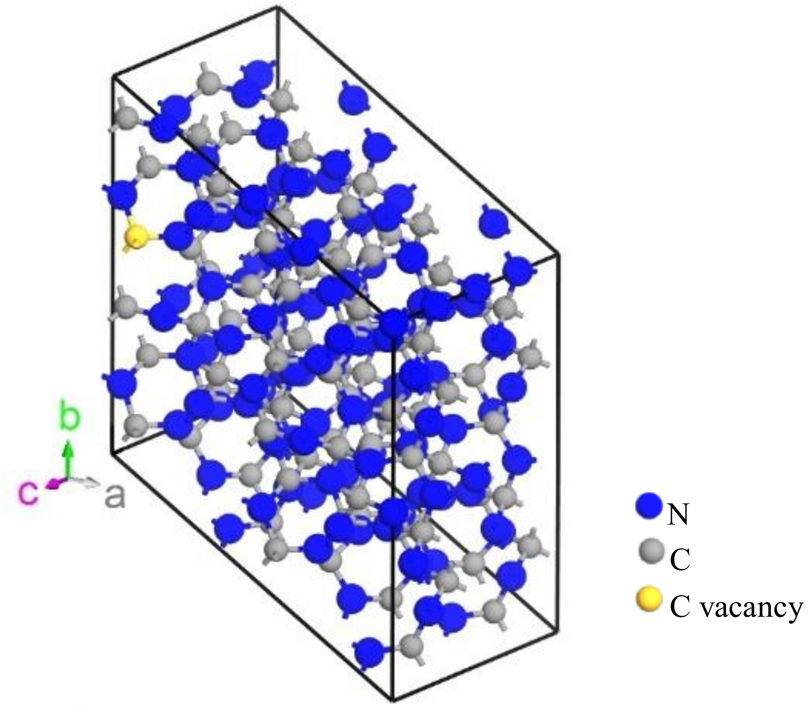

Figure 4.1.1 – Optimized atomic structure of C_3N_4 supercell with carbon vacancy

The first step of our studies is to check the effect of various kinds of disorder in bulk on the electronic structure and optical properties of C_3N_4. Pristine C_3N_4 is a wide-gap insulator. In the case of supercell optimization without constrained symmetry leads to appearance of some disorder in atomic structure (mean square deviation of calculated atomic positions from stoichiometric is 0.3 Å) but does not provide significant changes in electronic structure (Fig. 4.1.2). The changes in the band structure (Fig. 4.1.3a, b) is caused by appearance of non-equivalent atoms. The value of the direct bandgap remains almost the same. Thus, we can conclude that small amount of disorder does not induce luminescence in this system. These negligible changes in atomic and electronic structure induce significant changes in optical properties (Fig. 4.1.4). The blue shift in absorption spectra is similar to the case of the vacancies in bulk of C_3N_4. Formation of N-vacancy leads to decreasing of the bandgap by about 2 eV (Fig. 4.1.2 and 4.1.3d), and in the presence of the carbon vacancy (Fig. 4.1.1) vanishing of the bandgap occurs (Fig. 4.1.2 and 4.1.3c). According to absorption spectra shown in Figure 4.1.4, the absorption of bulk C_3N_4 is limited to the UV region of the spectrum whereas the absorption is below UV region for supercell. The contribution from the vacancies are clearly visible in Figure 4.1.4. Surprisingly, absorption function does not deviate visibly from the curve for lightly disordered pure bulk C_3N_4 (Fig. 4.1.4). Thus, we can conclude that the presence of the vacancies significantly influences the energies of valence band (VB) to conduction band (CB) transitions (see Fig. 4.1.3a) but for the absorption function, elimination of the symmetry is the key parameter. This conclusion is correct for the other optical properties of discussed systems.

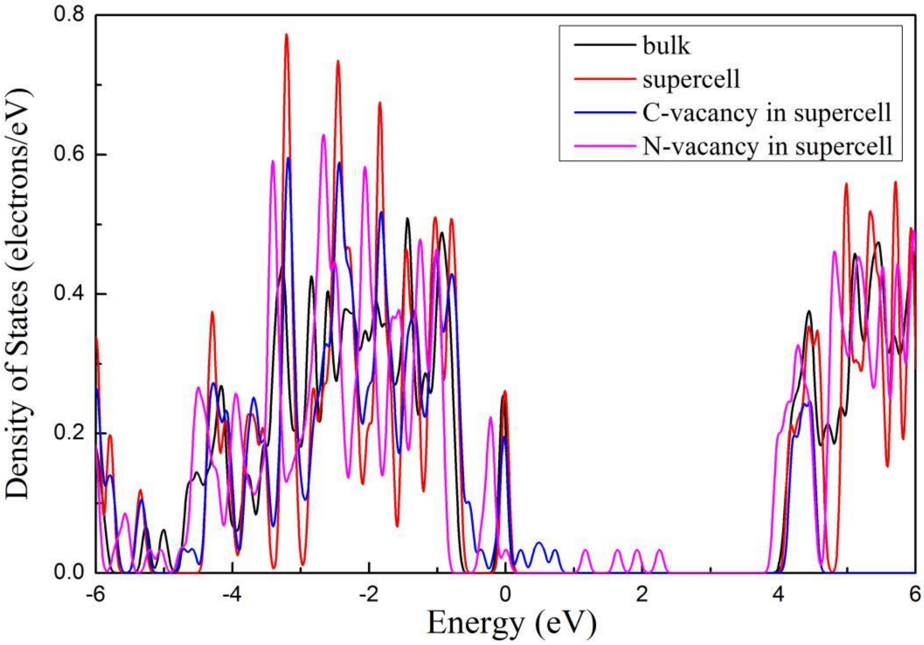

Figure 4.1.2 – Total densities of states for various configurations of bulk C_3N_4. Note that some states on Fermi level are caused by the smearing of densities of states, see band structures on Fig. 4.1.3.

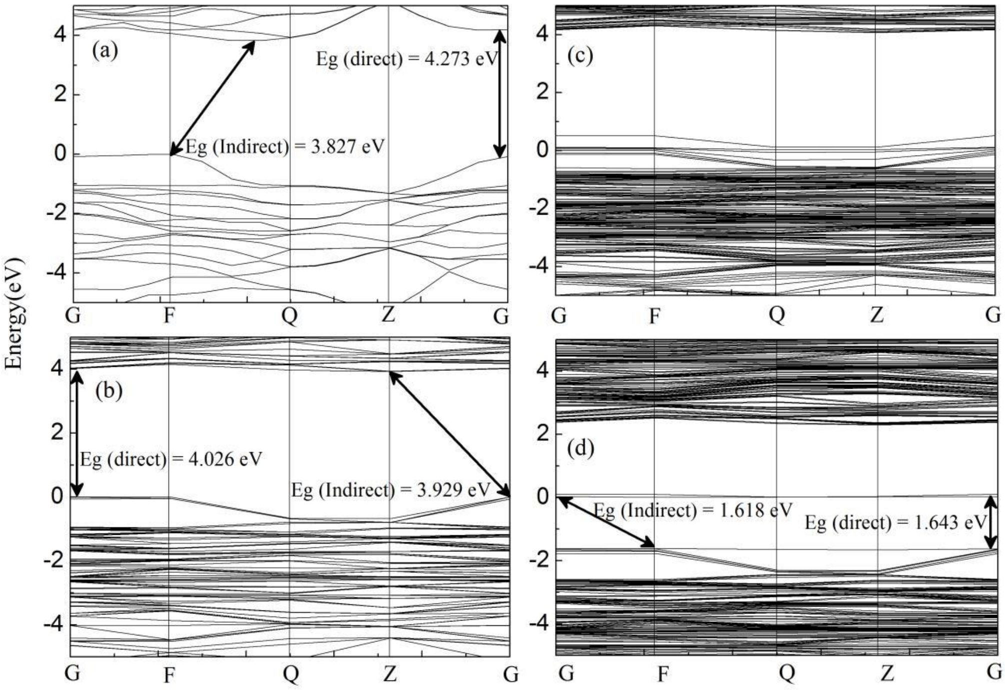

Figure 4.1.3 – Band structure of pristine (a), disordered supercell (b), carbon (c), and nitrogen (d) vacancy in C_3N_4.

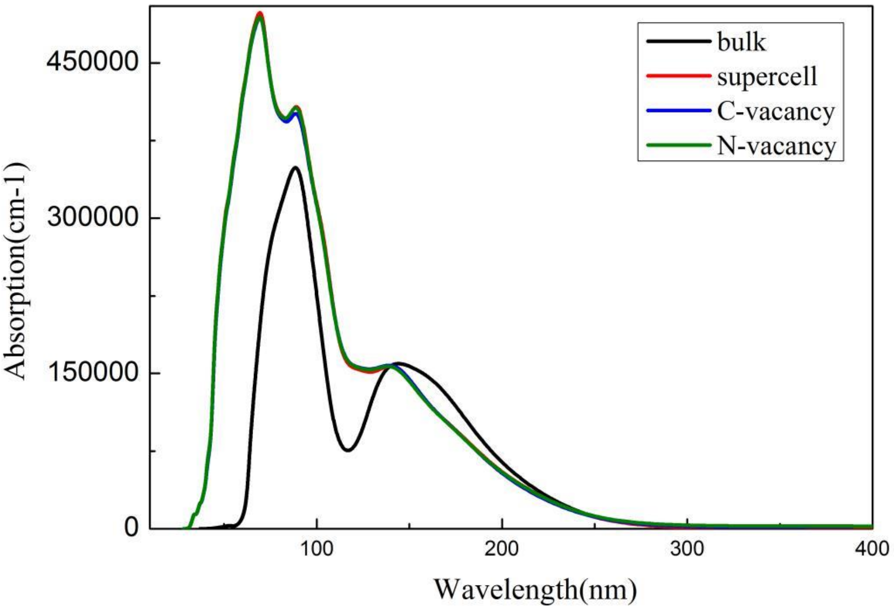

Figure 4.1.4 – Absorption function for various configurations of bulk C_3N_4.

It can be seen from Fig. 4.1.5 that the real and imaginary parts of C_3N_4 have two peaks respectively. The first peak of real part is appearing earlier than the first peak of imaginary part, and the peak value is high, and the second peak of real part is still appearing earlier than the second peak of the imaginary part, but the peak value is low. The imaginary part curve starts with a transition threshold, which is close to the band gap value of the corresponding compound, and then the curve rises rapidly, reaching a peak at 7.187 eV. When the energy is greater than 10.761 eV, the curve gradually increased again, and peaked again at 12.982 eV. The dielectric constant characterizes the ability of the dielectric to restrain the charge, and the insulation performance of the material. The larger the dielectric constant, the stronger the ability to restrain the charge, and the better the insulation performance of the material. The electron energy loss function is an important factor describing the energy loss when electrons penetrate the material quickly. The peak of the loss spectrum represents the plasmon resonance, and its corresponding frequency is the so-called plasmon frequency. When the photon energy is lower than the energy at the peak of the loss function, the material exhibits a dielectric function similar to that of metal, and when it is higher than the energy at the peak, the material exhibits the properties of an insulator. That is to say, the position of the peak of the loss function curve indicates the turning point of a material transition from insulator to metal. In addition, the peak of the loss function curve corresponds to the trailing edge of the reflection spectrum (Fig. 4.1.7). From loss function in fig.4.1.6 we can clearly see the peak position of bulk C_3N_4 corresponds to the lowest energy, which indicates that it is easier to transform from a semiconductor conductor, and it can be inferred from peak positions of other configurations that this transition is relatively difficult.

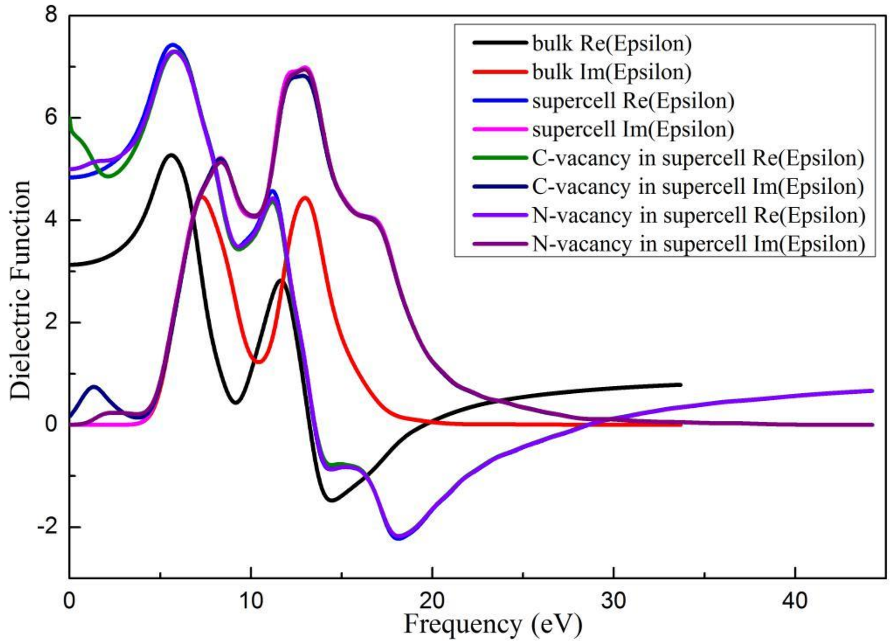

Figure 4.1.5 – Dielectric function for various configurations of bulk C_3N_4.

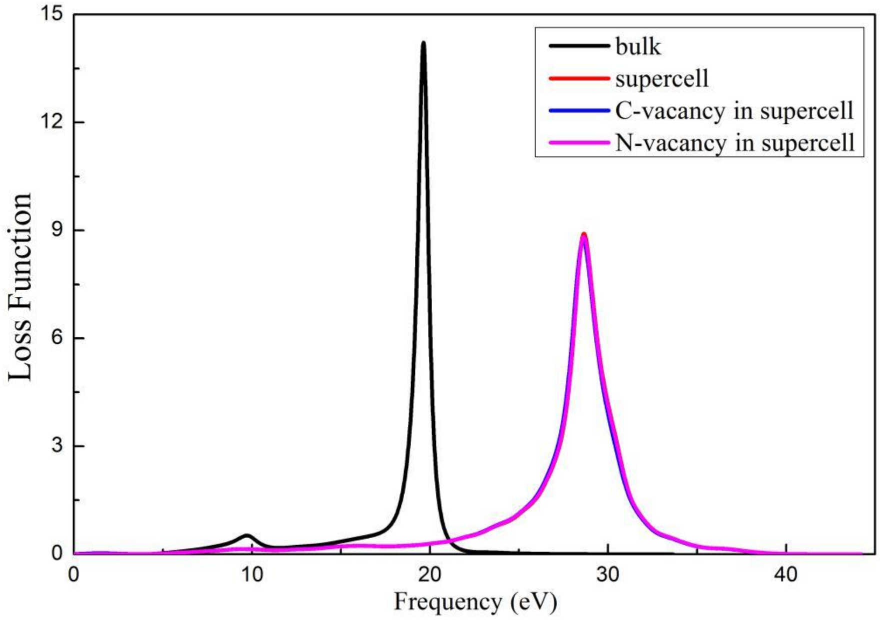

Figure 4.1.6 – Loss function for various configurations of bulk C_3N_4.

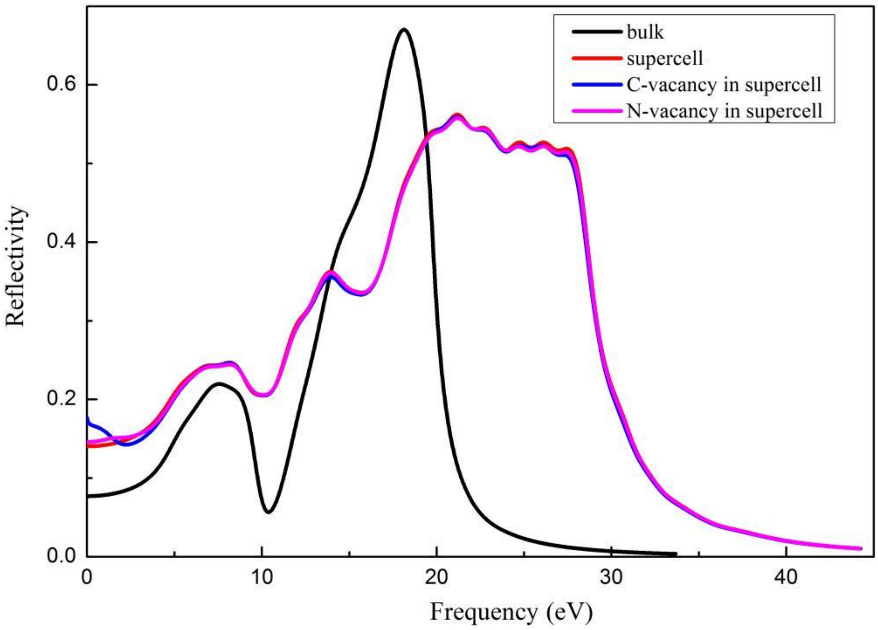

Figure 4.1.7 – Reflectivity for various configurations of bulk C_3N_4.

4.2 Surface modeling and identification of surface activity centers

For the modeling of the surface, we calculated the lattice parameters of bulk then built a slab by increasing the lattice parameter along *c* crystal axis (Fig. 4.2.1), usually one employs a slab of at least 6 layers within periodic boundary conditions. The nanoparticles of the size above 10 nm, atomic structure of the surface is mostly similar to the bulk, after that compared the charge value of atoms with the charge value in bulk, check which atoms have the largest difference, passivation of these atoms with hydrogen, oxygen and fluorine, after optimization find the configuration with the lowest total energy.

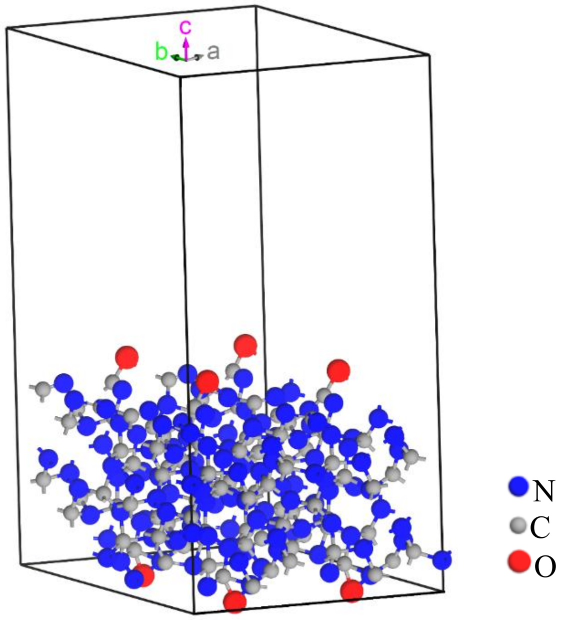

Figure 4.2.1 – (001) surface of C_3N_4 passivated by oxygen.

4.3 Nanocluster Modeling

For the modeling of the nanoparticles, we started our calculation from stoichiometric C_3N_4 structure inside empty box (Fig. 4.3.1). Similar to the case of slab, we recognized active sites on the surface of the nanocluster and performed the modelling of its passivation. Formation energies were calculated by standard formula:

$$E_{form} = (E_{products} - [E_{host} + mE_{mol}/2])/m \qquad (4.3.1)$$

where E_{mol} is the energy of a single molecule in empty box, E_{host} in the total energy of the system before attachment of m atoms. Because only diatomic molecules were considered in our work, we divided energy of molecule by two.

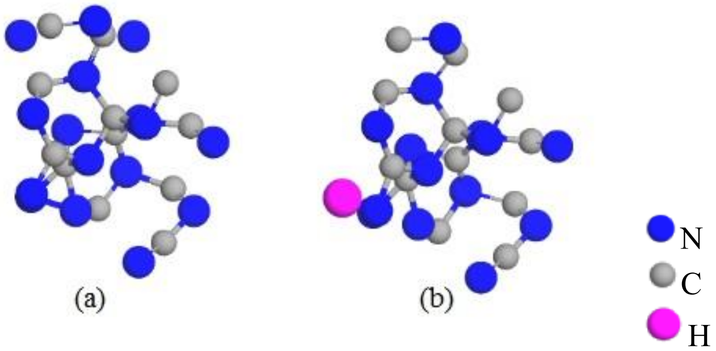

Figure 4.3.1 – bare (a), and passivated by hydrogen (b) nanocluster.

4.4 The effect of covalent modification on the electronic structure and optical properties of nanostructured (surface and nanoclusters) β-C_3N_4

The next step of our modeling is the check for the contribution from surface states. Note that for the nanoparticles of the size above 10 nm, atomic structure of the surface is mostly similar to the bulk. For the modeling of the surface, we used the slab of 230 atoms (see Fig. 4.2.1). Results of the calculations demonstrate significant (about 2.5 eV) decreasing of the bandgap (Fig. 4.4.1 and 4.4.2a). Visible decreasing of the bandgap can explain appearance of the luminescence in nanosized C_3N_4.

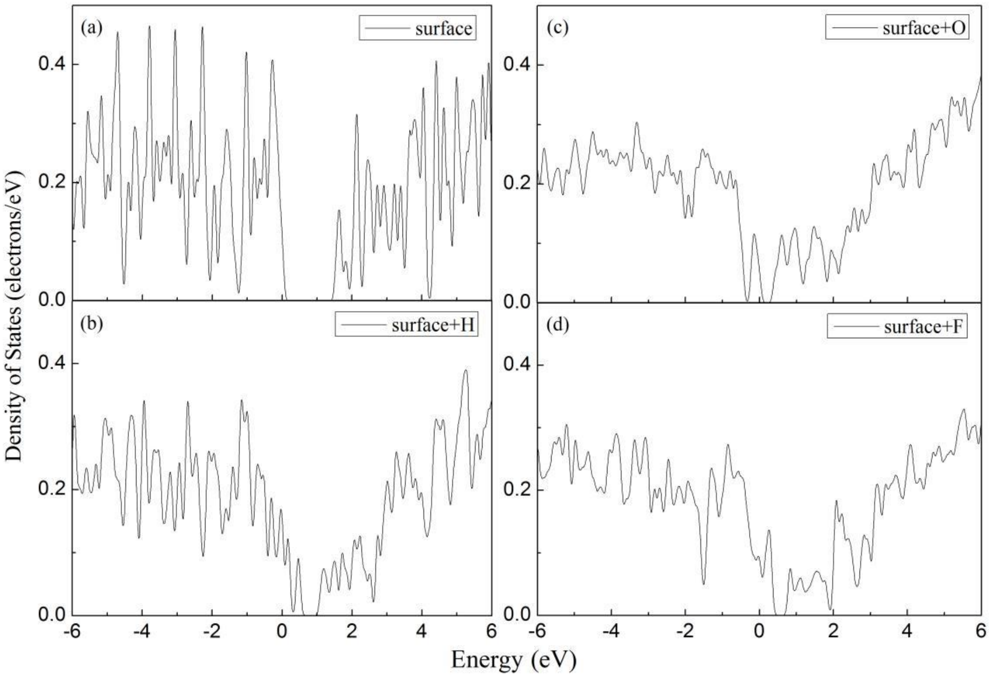

Figure 4.4.1 – Total densities of states of pristine (a) and passivated with hydrogen (b), oxygen (c), and fluorine (d) (001) surface of C_3N_4.

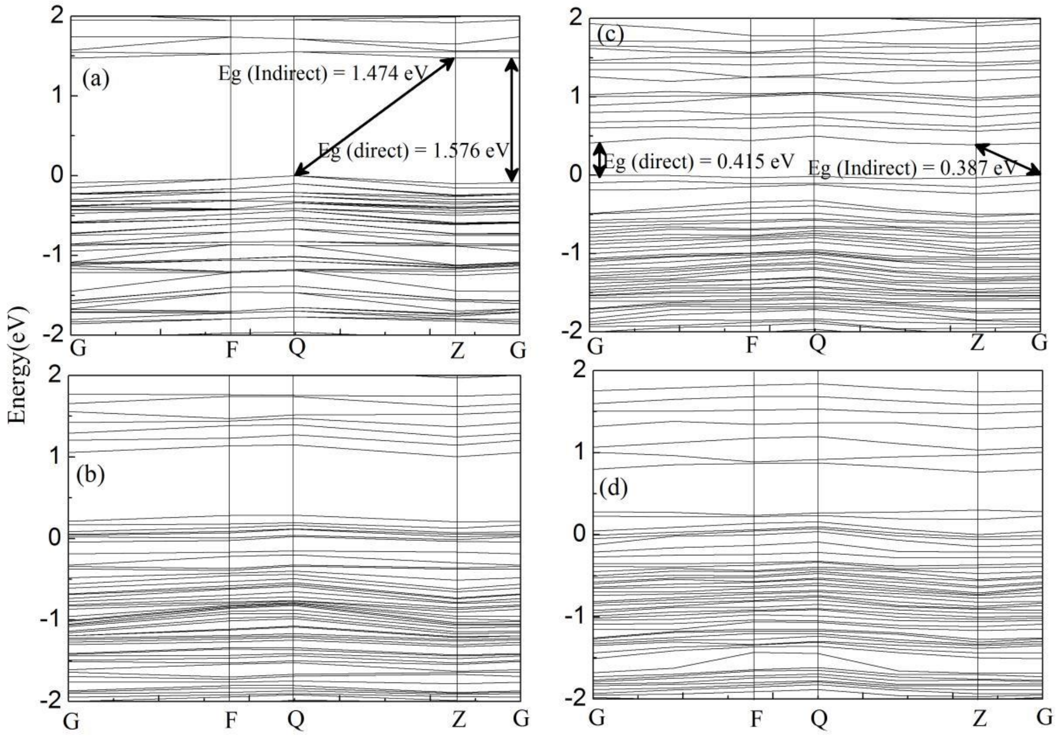

Figure 4.4.2 – Band structure of pristine (a) and passivated with hydrogen (b), oxygen (c), and fluorine (d) (001) surface of C_3N_4.

This decreasing of the bandgap corresponds with appearance of the dangling bonds on several surface atoms that provide the change in electronic structure (Fig. 4.4.3a,d). These atoms are the source of the surface chemical activity. For evaluation of chemical activity, we have performed the calculation of the formation energies of the passivation of these centers with hydrogen, oxygen (Fig. 4.2.1), and fluorine. The oxygen is the natural source of the passivation agents from the air. Hydrogen and fluorine have been chosen as the opposite (reduction vs. oxidation) species for artificial passivation. Calculated formation energies are -1.32, -2.31 and -5.62 eV for hydrogen, oxygen, and fluorine respectively. These results are evidence for the significant chemical activity of dangling bonds on (001) the surface of C_3N_4, which will be unavoidably passivated at ambient conditions.

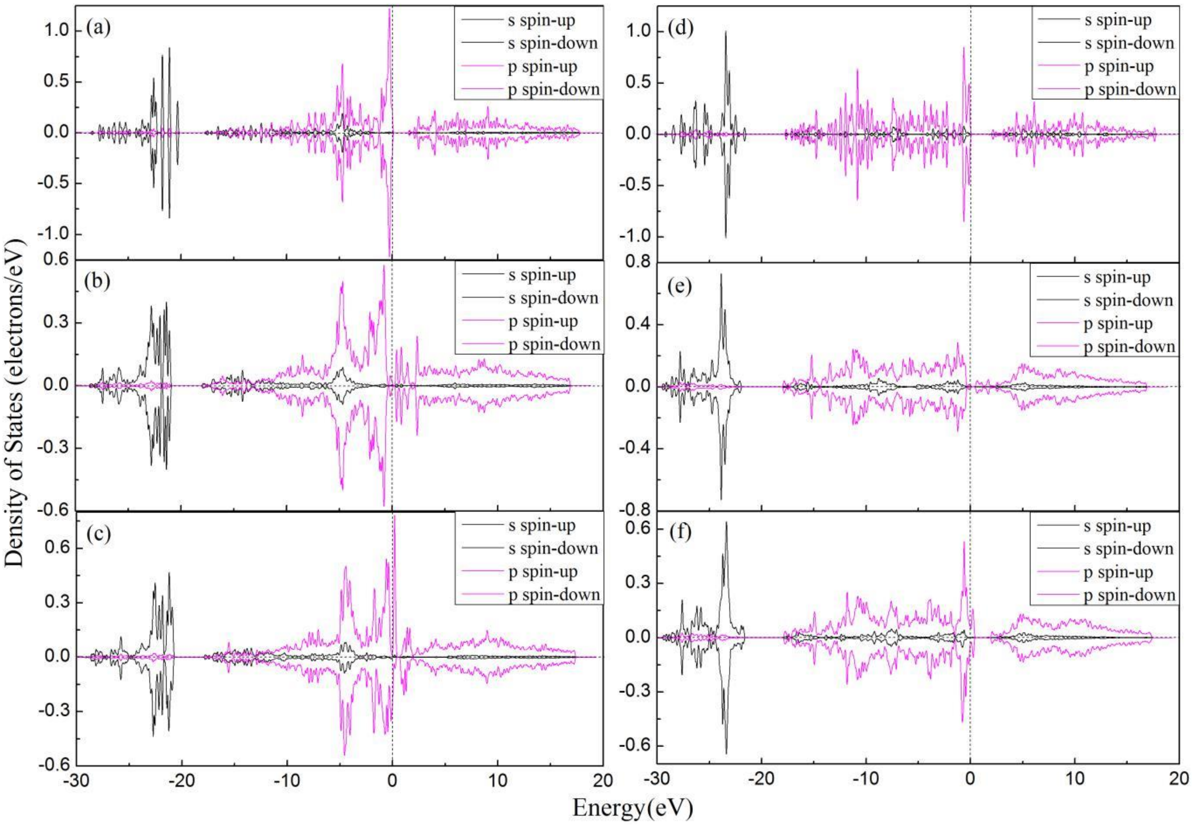

Figure 4.4.3 – Spin-polarized densities of states for the nitrogen atom with dangling bond on the surface of C_3N_4 (a) and inside the central bulk-like part of the slab (d), the same atoms after passivation of the surface by oxygen (b,e), the same atoms after passivation of the surface by fluorine (c,f).

The passivation leads to drastic changes in electronic structure of surface (Fig. 4.4.3 a, d) but also provides visible influence of the electronic structure of bulk (Fig. 4.4.3 b,c,e,f). Note that passivation with monovalent species can induce magnetic moment on the passivated atom, which is initially non-magnetic. Appearance of the magnetic moment is caused by interaction of monovalent species with non-magnetic lone-pair that provide formation of unpaired electrons of this atom. In the case of the interaction of the same atom with divalent species, both electrons of lone pair participate in the formation of the covalent bond. Thus, we can discuss hydrogenation and especially fluorination as the method for production of chemically stable *sp*-magnetic materials.

Passivation of the surface by different species leads significant changes in electronic structure (Fig. 4.4.1 and 4.4.2). In the case of fluorination and hydrogenation leading to the vanishing of the bandgap, this is corresponding with partial saturation of dangling bonds available for interactions with monoatomic species. In the case of the oxidation leading to the decreasing of the bandgap to the value of about 0.39 eV, this is in qualitative agreement with experimental results. [155-157] There is a significant absorption variation (around 120 nm) obtained in the surface on the hydrogen atom of C_3N_4 (shown in Fig. 4.4.4) compared with other surfaces. Similarly to the bulk, optical properties of the surface mainly depend on atomic structure and symmetry rather than the presence of defects and its further passivation (see Fig. 4.4.4-4.4.7). In general, optical functions of the surface are similar to the bulk with various defects.

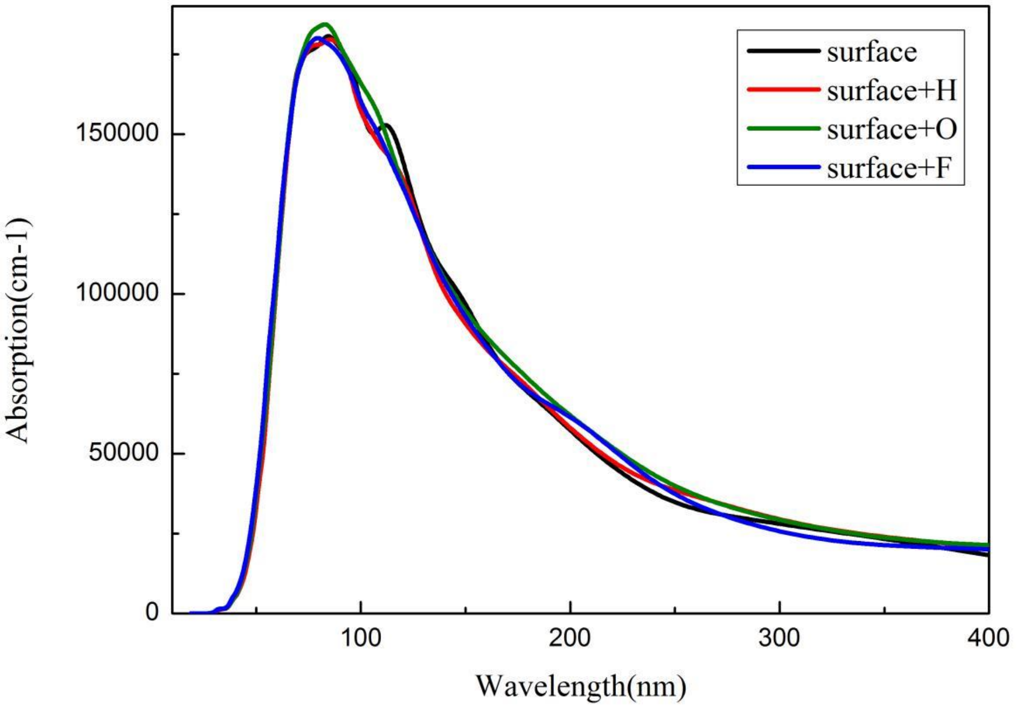

Figure 4.4.4 – Absorption function for surface of C_3N_4.

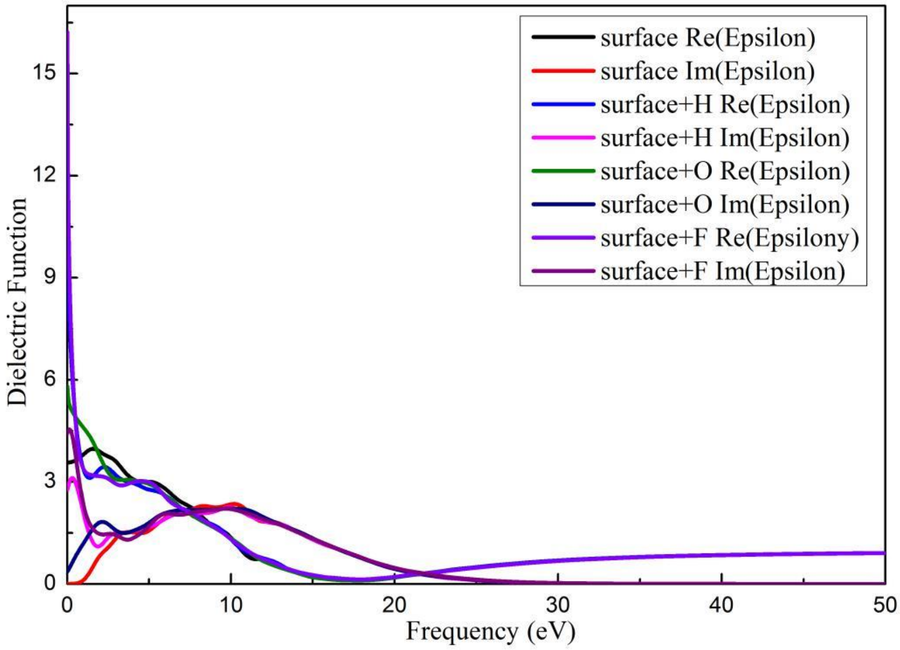

Figure 4.4.5 – Dielectric function for surface of C_3N_4.

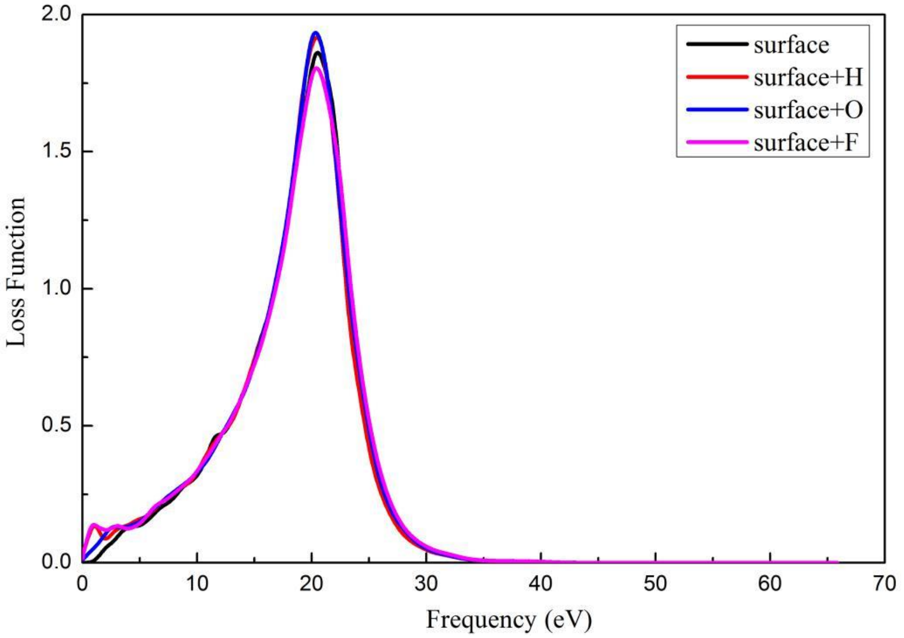

Figure 4.4.6 – Loss function for surface of C_3N_4.

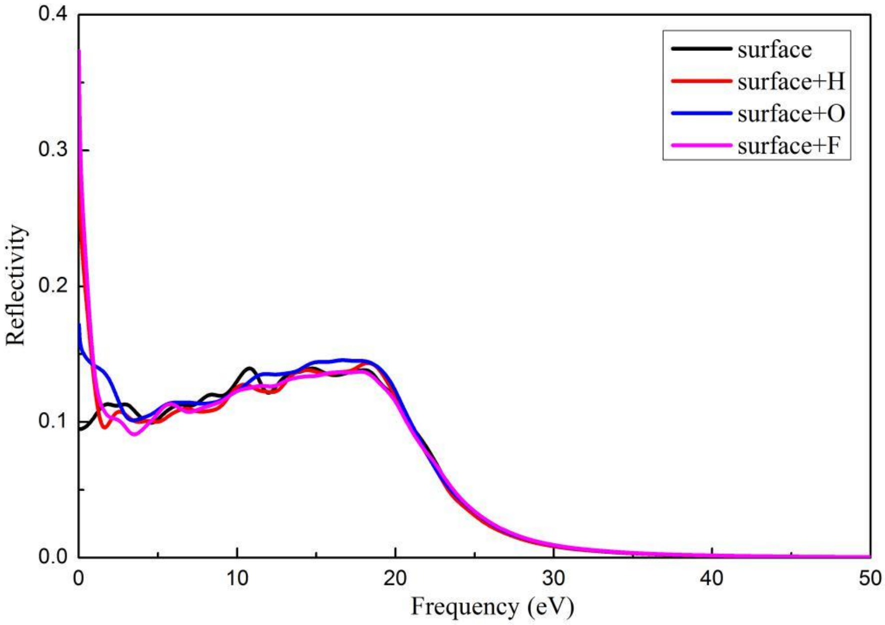

Figure 4.4.7 – Reflectivity for surface of C_3N_4.

The last step of our modeling is C_3N_4 nanoclusters (Figure 4.3.1). Electronic structure of nanocluster evidences the presence of dangling bonds on the surface (Fig. 4.4.8). Similar to the case of slab, we recognized active sites on the surface of the nanocluster and performed the modelling of its passivation. Negative sign and large magnitude of formation energies -4.40 eV, -6.99, and -7.11 eV/atom evidence chemical activity of the cluster. Note that some atoms on the surface of nanoclusters can be detached in the process of passivation (see Fig. 4.4.11-4.4.13). Similarly, the surface passivation leads to visible changes in electronic structure (Fig. 4.4.8 and 4.4.9). Oxidation and hydrogenation lead to the formation of the indirect bandgap of 0.27 and 0.46 eV that is in qualitative agreement with experimental results [155,158,159]. We can see that the absorption of nanoclusters of C_3N_4 ((Fig. 4.4.10) is different from surfaces, bulk, and vacancies spectrum. The nanoclusters of C_3N_4 elaborates that there is continues mountainous peaks (around 95, 110, 135, and 175 nm) obtained in the below-UV region with low intensities. In contrast to the bulk and surface optical properties of the nanocluster, which are different (Fig. 4.4.10). This deviates from the patterns typical for other bulkier systems caused by significant changes in atomic structure of nanoclusters (Fig. 4.3.1).

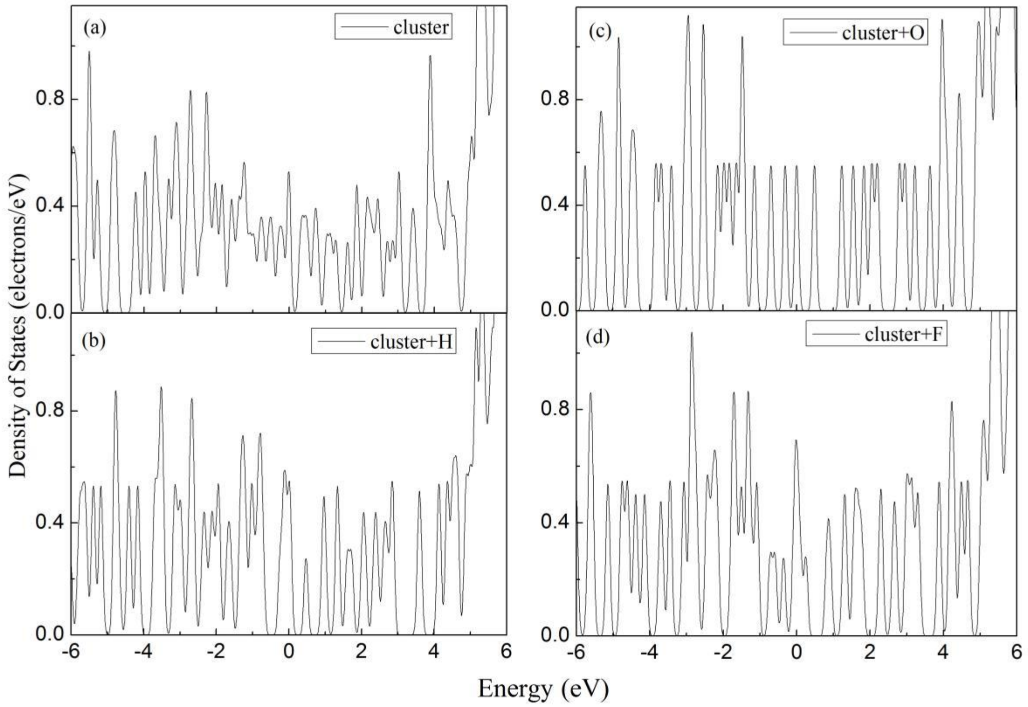

Figure 4.4.8 – Total densities of states of pristine (a) and passivated with hydrogen (b), oxygen (c), and fluorine (d) C_3N_4 nanocluster.

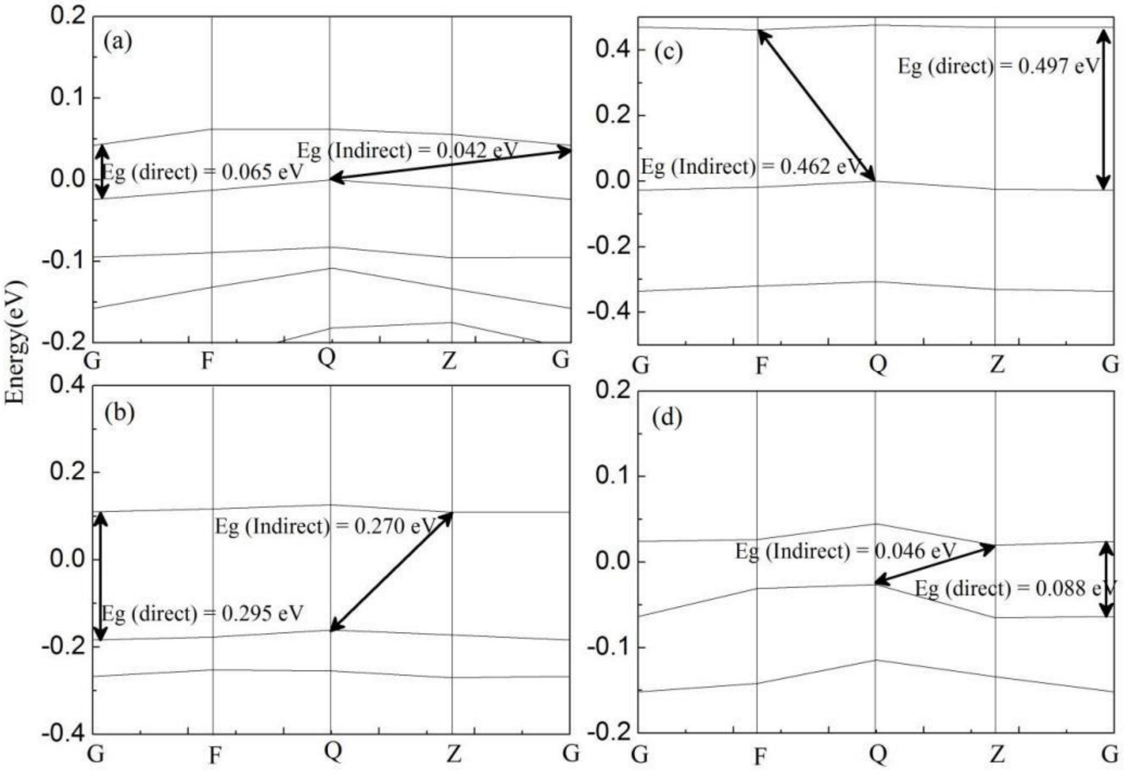

Figure 4.4.9 – Band structure of pristine (a) and passivated with hydrogen (b), oxygen (c), and fluorine (d) C_3N_4 nanocluster.

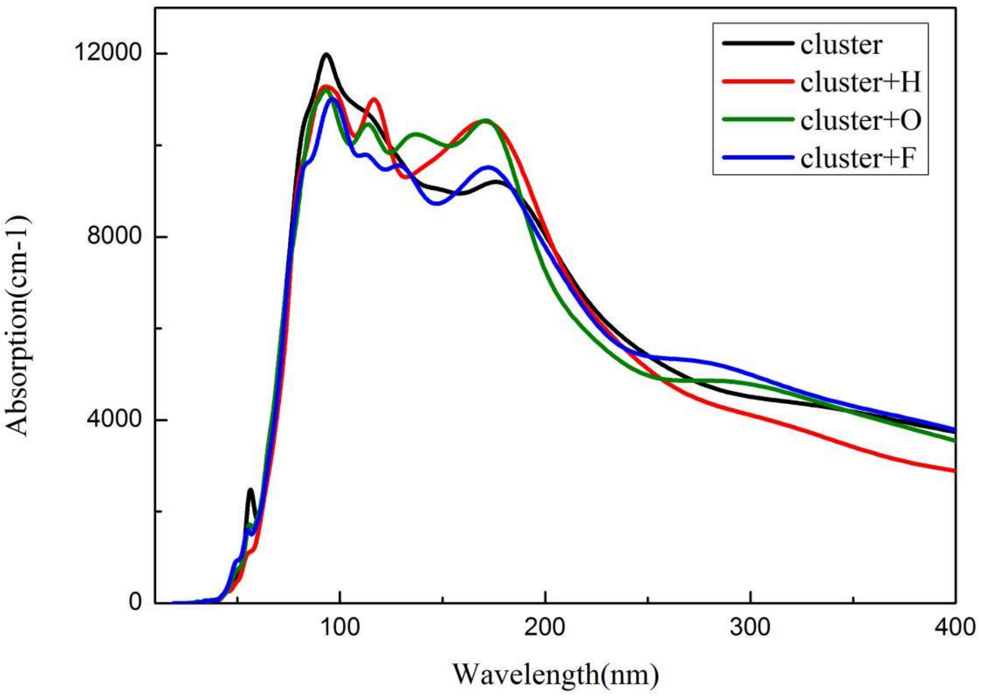

Figure 4.4.10 – Absorption function for nanoclusters of C_3N_4.

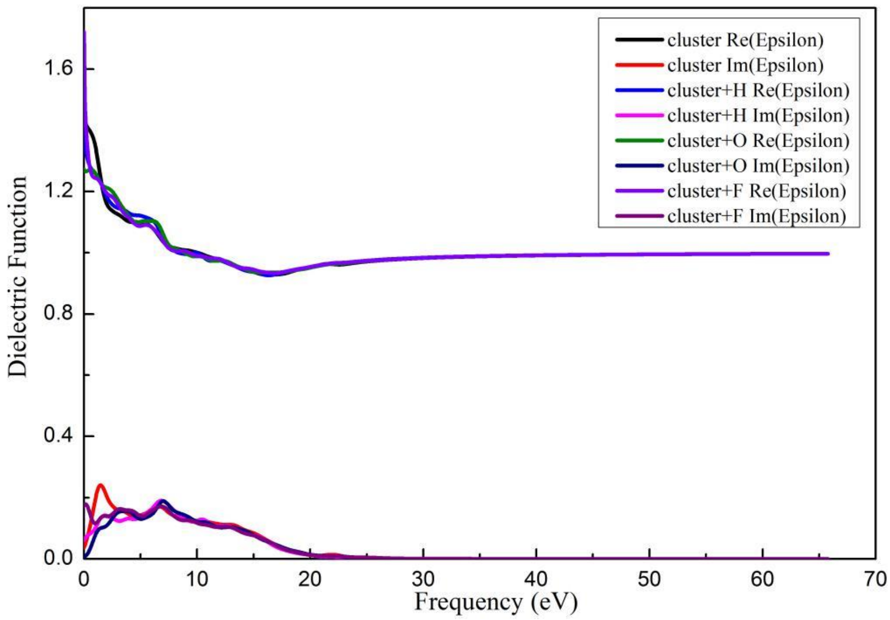

Figure 4.4.11 – Dielectric function for nanoclusters of C_3N_4.

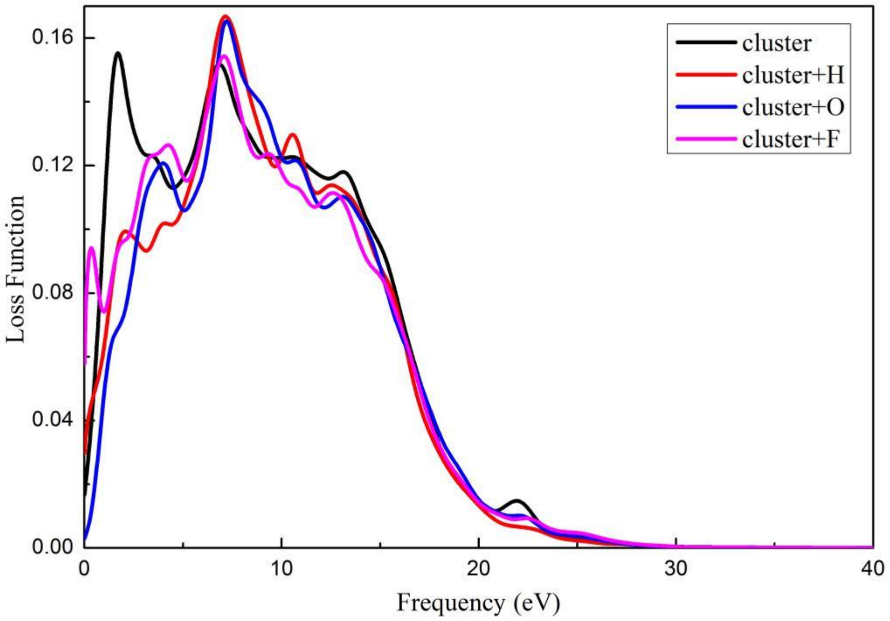

Figure 4.4.12 – Loss function for nanoclusters of C_3N_4.

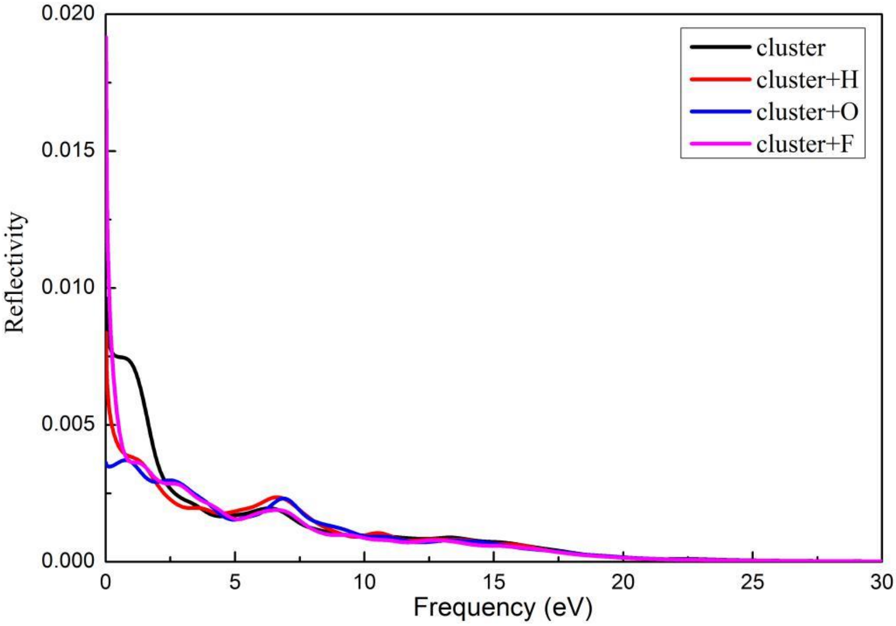

Figure 4.4.13 – Reflectivity for nanoclusters of C_3N_4.

4.5 Conclusion

First-principles calculations demonstrate significant sensitivity of the absorption, reflectivity, refractive index, dielectric function, conductivity, and loss function of β-C_3N_4 to the disorder in atomic structure. Fabrication and passivation of the surface does not significantly change these functions, but the value of the indirect bandgap depends on the chemical structure of the surface. In the case of (001) surface of bulky β-C_3N_4 and in the case of nanocluster, surface is the state of chemical activity, and some surface states will be unavoidably passivated. Partial oxidation of the surface of bulk and nanoclusters of β-C_3N_4 provides decreasing of the bandgap to 0.39 and 0.46 eV. Passivation of the surface by monovalent species (hydrogen and fluorine) vanishes bandgap in the case of (001) surface and changes the value of the bandgap in the case of nanoclusters. Therefore, functionalization of the surface of β-C_3N_4 is the route for predictable manipulation of the optical properties of this material.

CHAPTER 5. MODELING BOROPHENE OXIDATION

We make this work for discuss the stability at ambient conditions and the physical properties of oxidized borophene sheets. 2D materials beyond graphene is emerging area of current material sciences. Boron monolayers (borophene) is the one from this class. Despite more than 50 works in recent years about modelling structural composition and physical properties of this material theoretical evaluation of chemical stability was not performed. We make the step-by-step modeling of the oxidation of free-standing boron layers, the process of the oxidation will be exothermic and lead to the formation of foam-like boron oxide films with incorporation of boron clusters. The physical properties of oxidized boprophene sheets indicate that it possible application in areas of solar energy, sensors, coating and spintronic.

5.1 Description of borophene and its structural varieties

Planar hexagonal B36 was proposed as potential bases for extended 2D borophene [160]. After that, four phases (2-Pmmn, $\beta 12$, $\chi 3$ and graphene-like phases) of borophene have been synthesized on Ag (111) surface or Al (111) surface substrates under ultrahigh vacuum conditions [108, 161, 110]. The 2-Pmmn phase of borophene is a corrugated configuration with highly anisotropic electronic and mechanical properties, $\beta 12$, $\chi 3$ are planar without vertical undulations, for graphene-like borophene on Al substrate is more energetically stable than on Ag substrate [162]. In 2007, Yakobson's group [163] predicted the existence of mechanically stable B_{80} fullerene cage similar to C_{60} buckyball. However, hollow cages are indeed not the ground state structures for the medium-sized BN clusters from N=68, whereas core-shell configurations are more thermodynamically preferred based on ab initio global search by different groups [164,165] and others [166,167]. The energetic unfavorability of these empty boron cages can be attributed to the electron deficiency of boron, which tends to form more compact structures.

In recent works were reported that borophene is a highly anisotropic metal, the optical properties of borophene exhibit strong anisotropy as well [108, 168] and superconductivity induced by the strain. [169] Another experiments reports that the only line-edged borophene nanoribbons are stable in the free-standing form and demonstrate low-resistivity Ohmic conductance [170]. 2D borophene was proposed as an ideal electrode material with high electrochemical performance for both Li-ion and Na-ion batteries [171]. The stability of lattice defects including boron vacancy was investigated, they found find that the mechanical strength of borophene is reduced by the vacancy, the anisotropy in Poisson's ratio can be tuned [172]. Studied on the adsorption behavior of borophene towards SO_2 molecules by using density functional theory method [173]. Electronic and mechanical properties of few-layer borophene, for bilayer structures the AA stacking mode was found the most stable among the six high-symmetry stacking configurations. From monolayer to multylayer borophene was observed the robust anisotropic metallic features with large energy splitting at point 1.7 eV that is corresponding with strong interlayer van der Waals interactions. Since the layered structures can withstand larger critical strains than that in monolayer, layered borophene exhibits more flexibility than monolayer one [174]. NiB_6 monolayer was proposed as a stable 2D Dirac material with anisotropic elastic properties with a Young's modulus of 189 N m^{-1}. The calculation of band indicated that a double Dirac cone feature near the Fermi level with a high Fermi velocity of 8.5×10^5 m s^{-1}[175].

Stimulated by the B_{80} fullerene cage, a 2D boron sheet (BS), namely "α-sheet", with appreciable stability was constructed [176-178]. By incorporating periodic hexagonal holes in the triangular lattice to reach the balance between three-center (3c) and two-center (2c) bonds, this mixed hexagonal-triangular boron sheet (ht-BS) is more stable than previously proposed buckled triangular boron sheets (t-BS) [179-182], which can be explained by a chemical bonding picture that the hexagon holes serve as scavengers of extra electrons from the filled hexagons [183]. In recent works were reported results of the seeking of more stable structure for 2D allotropes of boron, including the snub-sheet, g1/8-sheet, g2/15-sheet, α1-sheet, β1-sheet, struc-1/8-sheet [184-187]. All these ht-BSs can be constructed by carving different patterns of hexagonal holes within the triangular sheet and described by a hexagon hole density η, defined as the ratio of number of hexagon holes to the number of atoms in the original t-BS.

These works motivate experimentalist to further attempts to synthesize free-standing borophene. In previous experiments [188,189], single-walled and multi-walled boron nanotubes have been observed, which hints the possible existence of boron monolayer sheet since a boron sheet can be viewed as unrolling a boron nanotube. With metal passivation to stabilize the sp^2 hybridization, similar silicene monolayer has been successfully fabricated on Ag(111) and Ir(111) surfaces in recent experiments [189-193], providing important clues for BS synthesis. On the other hand, small boron clusters in vacuum were proved to adopt quasi-planar configurations [109,194-199], which may act as precursors for experimental synthesis of BS on metal surface via soft-landing of cluster beams [200].

Note that the synthesis of BS was done in the absence of oxygen but possible application in devices usually will be at ambient conditions. Fast degradation of the phosphorene [201,202] and oxidation of dichalcogenides [203] suggest that additionally to mechanical stability chemical stability should be also discussed. In our work we provide modelling of step-by-step oxidation of two representative types of borophene sheets and discuss the properties and possible applications of obtained oxidized boron sheets (OBS).

5.2 A step-by-step description of the oxidation process of two borophene allotropes.

Multiple structural phases of BS reported in the previous works. [184-187] These structural phases have almost the same total energy per boron atom. This multiple structural forms of BS can be classified in several groups denoted by Greek letters. The most energetically favorable is so-called β and χ types of BS. The first type can be described as continuous BS with triangular lattice with the pairs of hexagonal pores nearby (Fig. 5.2.1). Ne number of these pairs of hexagonal pores per unit of square can vary within this type. The second is the same triangular lattice with the lines of hexagonal pores (Fig. 5.2.2). The distance between the pores can be different for BS of this type. Two structures (one from each class of BS) with minimal number of the atoms in the supercells have been chosen for the further modeling.

For both types of studied BSs we have find that the first step of the oxidation will be decomposition of molecular oxygen on the edges of hexagonal pore (Figs. 5.2.1, 5.2.2). For the check of the favorability of this process we performed the calculation of formation energy by standard formula:

$$\mathrm{Eform} = \mathrm{E(host{+}guest)} - [\mathrm{E(host)} + \mathrm{E(guest)}] \qquad (5.2.1)$$

where E(host+guest)] is the energy of the system after decomposition of the oxygen atom, E(host) is the total energy of the system before this process and E(host) is the energy of oxygen molecule in ground (triplet) state in gaseous phase. Results of the calculations demonstrate that for both types of considered BSs this process is extremely energetically favorable. Because the magnitude of formation energy is several times larger than activation energy of the oxygen on pure and doped graphene [204] the process should be barrierless.

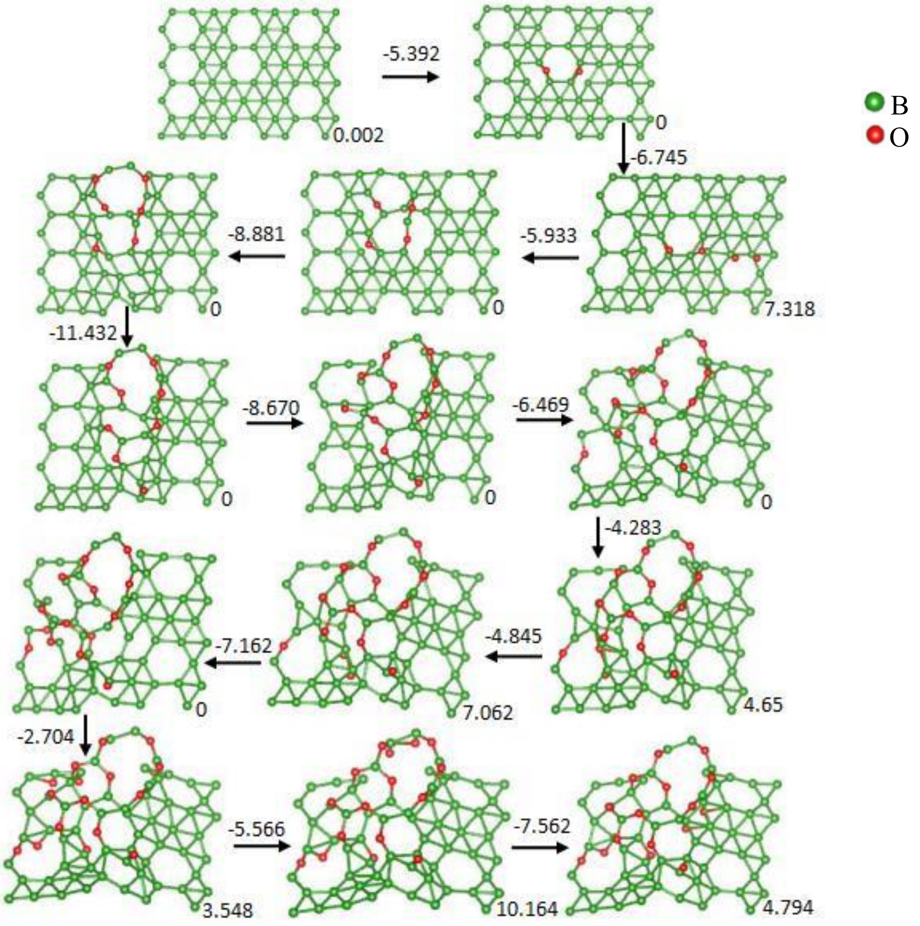

Figure 5.2.1 – Optimized atomic structure of the first steps of the oxidation process of boron sheet of β-type. The numbers near the arrows is formation energies (in eV) and numbers in the corner of the structures is total magnetic moment of the

supercell (in μ_B).

Significant favorability of the first step of the oxidation suggest us to perform further modelling of step-by-step oxidation. Because distortion of the monolayer in result of the first step of the oxidation increase the number of non-equivalent pairs of atoms we considered only decomposition of the next oxygen molecules in vicinity of the hexagonal pores and on the boron atoms with the largest out-of-plane distortions. Results of the calculations (Figs. 5.2.1, 5.2.2) evidence similarity of the patterns of further oxidation for both types of BSs: oxidation continue first on the borders of hexagonal pores and then goes deeper in the areas of continuous triangular lattice. All steps of the oxidation process of both types of BSs is also significantly favorable. This energetic favorability persists when oxidation process turns from edges of the hexagonal pores into the areas of triangular lattice. Further steps of the oxidation are also energetically favorable and lead formation of foam-like structures in both considered types of BSs (see Fig. 5.2.3). Note that in both studied structures in the process of oxidation occur formation non-oxidized boron cluster with atomic structure similar to B_{12}. [166] Based on results of the modelling that demonstrate similarity for two representative samples of different types of BSs can propose that our results are valid for all BSs.

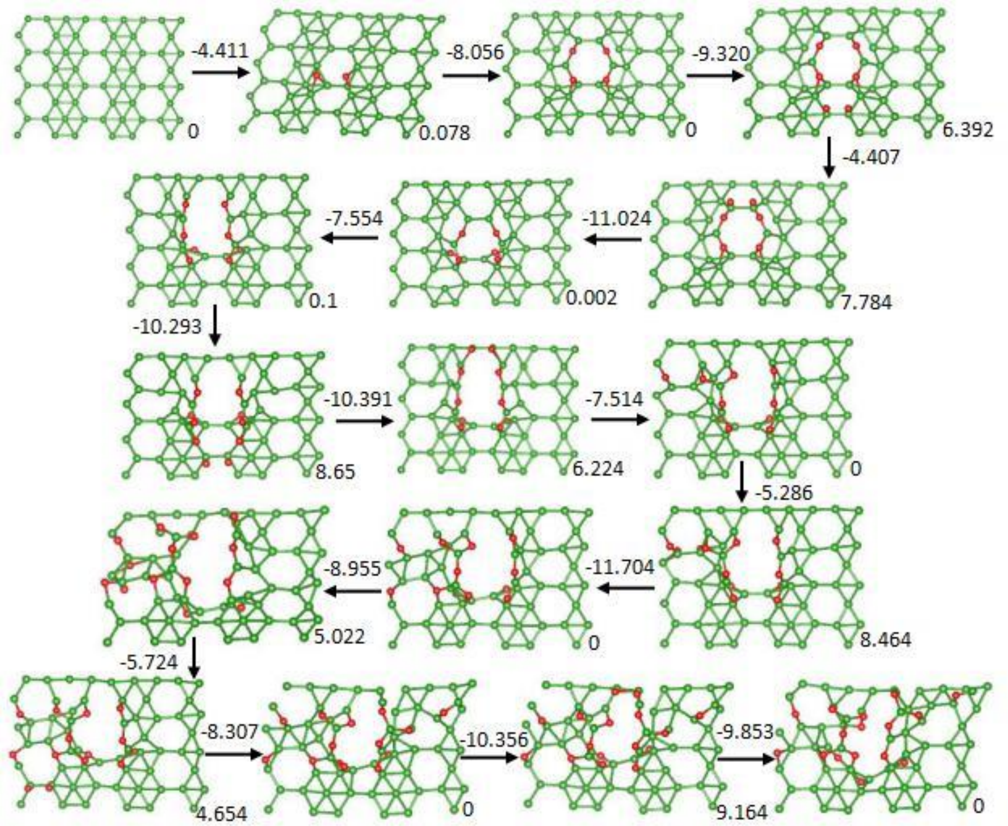

Figure 5.2.2 – Optimized atomic structure of the first steps of the oxidation process of boron sheet of χ-type. The numbers near the arrows is formation energies (in eV) and numbers in the corner of the structures is total magnetic moment of the supercell (in μ_B).

Therefore similarly to the phosphorene, [201,202] BSs require fabrication of additional protective cover from chemically inert material (for example hBN). [205] From the other hand oxidized BSs (OBSs) can be interesting by itself and further we provide evaluation of the properties of these materials that can be used in further applications.

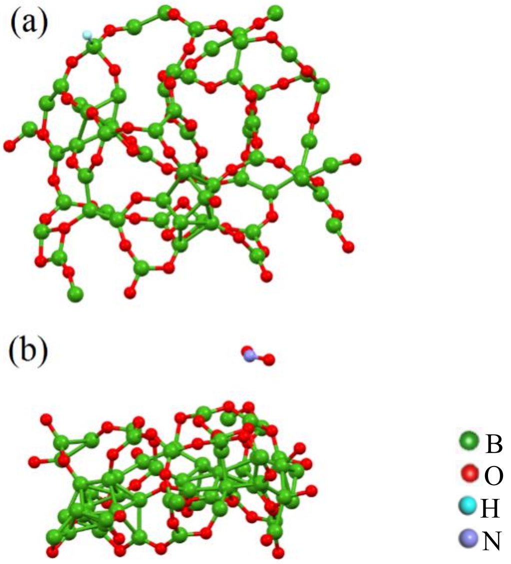

Figure 5.2.3 – Optimized atomic structure of totally oxidized boron sheet of β-type with magnetic center passivated by hydrogen atom (a) and totally oxidized boron sheet of χ-type with physically adsorbed molecules of NO_2.

5.3 The proposal of a simplified method to identify centers of chemical activity on the surface of two-dimensional systems

Chemisorption is an adsorption in which an adsorbate molecule and an atom (or molecule) on a solid surface undergo electron transfer, exchange, or sharing to form an adsorption chemical bond.

For evaluate the most active sites for oxidation by molecular hydrogen we locate the oxygen atoms above the nearest boron atoms in different non-equivalent places of BSs and after optimization find the configuration with the lowest total energy.

5.4 Description of the mechanical and magnetic properties of borophene

In contrast to graphene where formation of epoxy groups does not induce any magnetic moments oxidation of both considered types of BSs provides appearance of dangling bonds which is the source of unpaired electrons. [206] The cause of this difference is odd number of electrons in boron 2*p* shell. At early step of oxidation magnetic moments is rather large because adsorption of the oxygen atoms provides break of multiple bonds. The values of magnetic moments per supercell at early stages of the oxidation is non-integer because BSs remain metallic. Further oxidation until final step provides saturation of all dangling bonds in χ-OBS but surprising survival of magnetism (1 μ_B per cell) in β-OBS. Usually oxidation provide vanishing of *sp*-magnetism (also called *d*0-magnetism) by saturation of all dangling bonds but in the case of β-OBS where special topology prevents passivation of magnetic center. [207] Formation of this magnetic state in β-OBS is related with appearance of the states in vicinity of Fermi level (Fig. 5.4.1). The sharp peak is related with the single $2p^1$ electron localized on non-oxidized boron atom surrounded by oxidized boron atoms. Survival of the magnetic moment suggest the absence of the second boron atom suitable for the oxidation in vicinity of magnetic center. To evaluate magnetic interactions between remote magnetic centers we multiply the supercell along a-axis and calculate the difference between total energies of the systems with parallel and antiparallel orientation of the spins on magnetic centers. Calculated difference evidence that magnetic interactions between the centers is ferromagnetic. The magnitude of the energy difference between ferro- and antiferromagnetic configurations is 5 meV. Discussed magnetic moments in OBS can be eliminated by monovalent species. For the check of this possibility we modeled hydrogenation of boron atom with magnetic moment in β-OBS (Fig. 5.2.3a). Saturation of dangling bond provides elimination of magnetic moment and appropriate features in electronic structure because now unpaired electron on 2p shell participate in covalent bond with 1s electron of hydrogen that provides shift down of the corresponding energy level (Fig. 5.4.1). In result of the hydrogenation of magnetic center the value of calculated within GGA approach bandgap increased from about 0.1 to almost 0.4 eV. Note that DFT provides underestimation of the bandgap. To estimate the values of the real bandgap we will used relation between GGA and experimental values discussed in the Ref. [208] Thus the calculated value of 0.1 eV is corresponding with experimental value of about 0.3 eV and calculated 0.4 eV with the real bandgap of 0.8 eV. Note that discussed passivation is endothermic process and require the energy of +0.53 eV/H. Thus magnetism in OBS is chemically stable even at room temperature. This combination of air-stable ferromagnetism and narrow bandgap makes β-OBS prospective material for spintronic applications but further experimental exploration of the reproducibility of magnetism in OBS is required. In the case of non-magnetic χ-OBS the value of the calculated bandgap is larger (calculated value ~1 eV that is corresponding with the experimental values of order of 1.8 eV) which in combination of low weight and flexibility makes this material attractive as material for solar cells. The multiple peaks around Fermi energy (between -2 and +2 eV) could be the source of multiple optical transitions [208] that makes OBS optical-active material. The appearance of these peaks is related with formation of localized states of the electrons on bonds between non-oxidized boron atoms (see Fig. 5.2.3 and Fig. 5.4.1). Partial oxidation provides break of the continuous web of the overlapping π-orbitals [184-187] of boron atoms that lead to the opening of the bandgap. Thus the number of the peaks near Fermi level and the distance between the peaks depends from initial atomic structure of borophene that guide oxidation process and amount of non-oxidized boron atoms and as results localized $2p^1$ states near Fermi level.

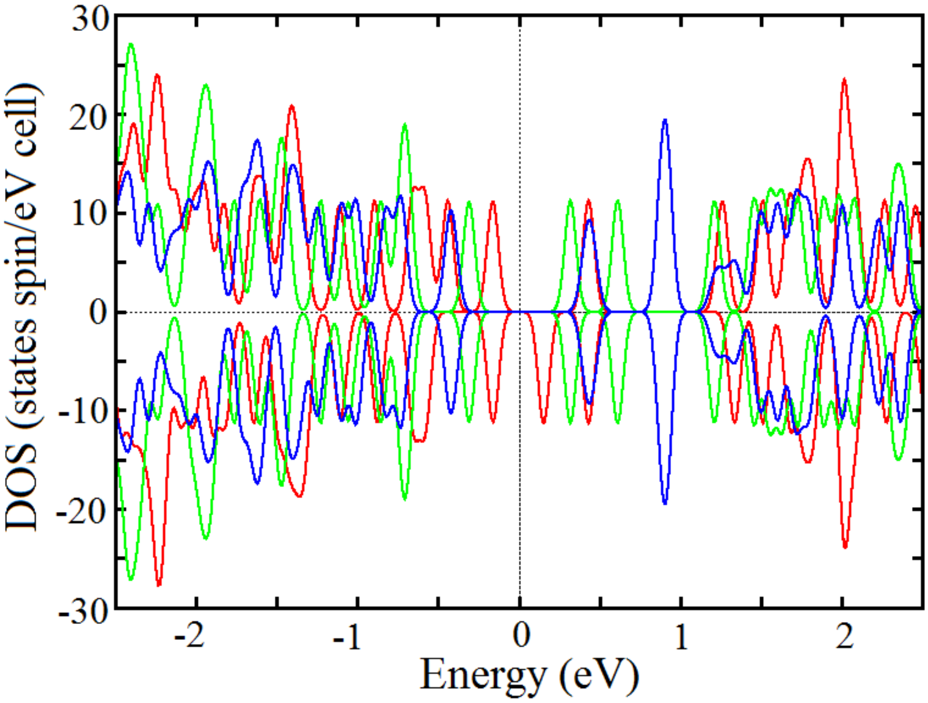

Figure 5.4.1 – Spin-polarized density of states of fully oxidized boron sheet of *β*-type (red line) and *χ*-type (blue line). Green line is corresponding with *β*-OBS after passivation of magnetic center by hydrogen (Fig. 5.2.3a). Charge density distribution in the part of oxidized *β*-OBS are shown on inset.

The next step of our survey of the physical and chemical properties of OBS is the study of the conditions of adsorption of various molecules on both studied types of OBS and influence of the adsorption on electronic structure. In our modelling we considered three types of the adsorbants - nitrogen dioxide, water and hydrogen. First we calculated enthalpy of adsorption by the same formula that was used for the calculation of the formation energy. Results of calculations (see Tab. 5.4.1) demonstrate robust adsorption of nitrogen dioxide and water on β-OBS and less stable adsorption on χ-OBS.

Table 5.4.1 – The enthalpies of adsorption (eV/mol) of selected gases on OBSs.

Adsorbant/Substrate	β-OBS	χ-OBS
NO_2	- 0.357	-0.170
H_2O	-0.386	-0.119
H_2	-0.008	-0.059

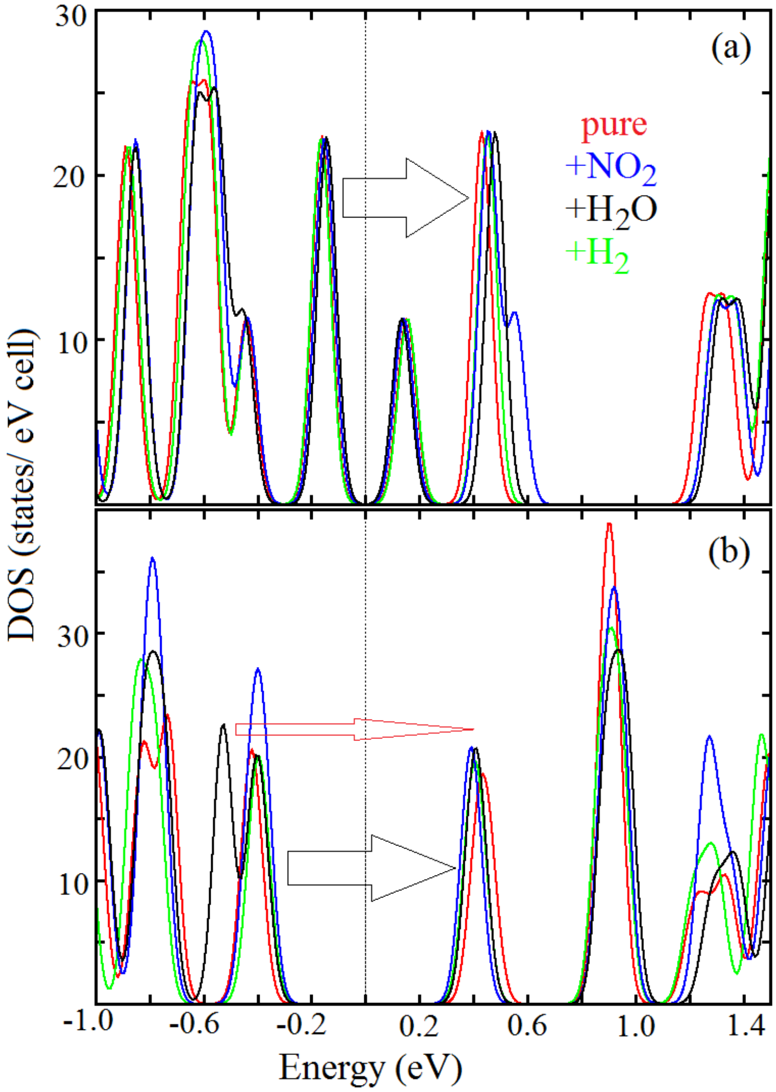

Figure 5.4.2 – Total densities of states of β-OBS (a) and χ-OBS (b) before (red) and after adsorption of nitrogen dioxide (blue), water (black) and hydrogen (green) molecules. Arrows are indicating possible optical transitions influenced by adsorption of the molecules.

For the hydrogen molecule stable adsorption will occur only at χ-OBS but the magnitude of the enthalpy of the process is rather small. Unstable adsorption of hydrogen molecule on β-OBS provides no changes in electronic structure in vicinity of Fermi level. Contrary, all considered cases of the stable adsorptions provide visible changes in the positions and shapes of some peaks in vicinity of Fermi level that should change the intensity and perhaps quench some optical transitions (the key transitions are shown by arrows in Fig. 5.4.2). In the case of β-OBS will occur blue shift in adsorption and in the case of χ-OBS red shift. Note that similarly to other boron nanostructures both studied OBS systems changes in the electronic structure is distinct for each type of adsorbed molecule therefore OBS can be proposed as sensing material with high selectivity. Adsorption of water provides appearance of the states at about -0.6 eV that can create additional transitions. So we can propose OBS as chemically stable humidity sensors.

5.5 The use of oxidized borophene as a membrane for the separation of atomic hydrogen and protons

Combination of porous structure and chemical stability of OBSs creates opportunities for possible usage of these materials as membranes for the separation of the gases. For evaluation of permeability of OBSs we performed calculation of migration of hydrogen atom and hydrogen protons throughout the centers of the pores in both considered OBSs. For the simulation of the proton we generate pseudopotential for hydrogen atom with $0.05e^-$ on 1s orbital and perform the calculation of the system with the charge $+0.95e^-$. This method was previously used for the study of the migration of the proton trough graphene and hexagonal boron nitride. [209] Results of the calculations demonstrate energy barrier for H^+ is 0.704 eV for β-OBS and 0.594 eV for χ-OBS. For atomic hydrogens the values of the energy barriers are 0.751 and 0.693 eV. Thus OBSs could be proposed as impermeable material for hydrogen material and can be used for the coating of the volumes for hydrogen storage and flowing to prevent hydrogen leakage.

5.6 Conclusion

Our first-principle modelling of the interaction of borophene sheets with molecular oxygen demonstrate instability of these materials in free standing form to oxidation. In result of the exothermic oxidation, borophene sheets will turn to foam-like boron oxide membrane with incorporated non-oxidized boron clusters. Obtained material is narrow-gap semiconductor and can be used as light-weight chemically stable solar cells. In some kinds of borophene sheets oxidation provide the appearance of stable at ambient condition *d0*-magnetism caused by unpaired electrons on single non-oxidized boron atoms. Stable physical adsorption of various gases on oxidized borophene sheets leads to the changes in optically active part of borophene spectra that make this material attractive for gas sensing. The calculated barrier for the migration of protons of hydrogen and atomic hydrogen through the pores of oxidized borophene demonstrates the impermeability of the membrane for both considered species, which makes it possible to use oxidized borophene as a coating preventing hydrogen leakage.

CHAPTER 6. NON-COVALENT MODIFICATION OF INDIUM SELENIDE

We make this work to solve the disagreement between experimental works and within theoretical community about adsorption properties and chemical stability of InSe. InSe discussed as the one of the most prospective two dimensional materials. We performed modelling of the adsorption of some commonly considered gases on InSe. In contrast to previous theoretical works we vary not only the adsorbnats but also the size of supercell and especially the modes of the optimization, we demonstrate that favorability of the adsorption of the same gas on the same supercell can be totally different if we optimize only atomic positions and both atomic positions and lattice parameters. For make our work more comprehensive we check the influence of in-plane and out-of-plane distortions of the substrate and found that even minimal distortions (for example stretching at 1%) of the substrate significantly influence adsorption of the molecules. We can conclude that each previous work is correct but describe interaction of InSe with environment at some narrow range of conditions and even slight change of these conditions could provide significant change in chemical properties. Because InSe is the member of the broad family of similar materials and more populous class of dichalcogenides is also contain very flexible 2D membranes results reported in our work can be applied to large number of real and hypothetic 2D materials.

6.1 Two-dimensional topological materials and their potential application

More and more researchers study two-dimensional topological materials due to the promise of devices with non-dissipative electric or spin currents, the exotic electronic states may provide a new approach for spintronics, quantum computation and many other potential device applications [210-212].

The two-dimensional topological insulator has a non-dissipative boundary state at its boundary, which provides a preferred material for non-dissipative micro-nano devices. At the same time, this boundary state is protected symmetrically by time inversion, so it can resist the disturbance of non-magnetic impurities or defects. Under the combined effects of spin-orbit coupling and time inversion symmetry breaking, some materials can achieve a special Hall effect: the quantum anomalous

Hall effect. Its characteristic is that in the absence of an external magnetic field, the boundary of the material still has a non-dissipative boundary state. The electrons transmitted in these channels will not collide with each other. This special Hall effect provides a new direction for low-power electronic devices in the future.

6.2 Description of the atomic structure of indium selenide and the current state in the description of the surface activity of indium selenide and related materials

Since the successful isolation of graphene, the greatly favors applications of two-dimensional materials in electronics, optoelectronics and other fields due to their physical and chemical properties. [26-28, 213-215] Two-dimensional materials have ultrathin thickness, the high surface area provides a large number of reactive sites, which makes them efficient adsorbents for gas molecules, these materials efficient in catalysis, sensing, solar energy conversion and storage technologies. [216-218]

Recently, indium selenide (InSe) with a hexagonal structure and a typical layered semiconductor characteristic has gained increasing attention owing to its intriguing electronic properties. For example, MoS2 with the direct (monolayer) to indirect (multilayer) transition, while InSe has an indirect band gap for monolayer and a direct band gap for multilayer sheets when exceeding a critical thickness. [219] Bulk InSe has three forms (β-phase, γ-phase, and ε-phase) with a layered crystal structure, it has a honeycomb lattice that consists of four covalently bonded Se-In-In-Se atoms, the layers are bonded together by interactions discussed as the van der Waals interactions. [220-222] As a two-dimensional material, it was found that the electron mobility of the boron-nitride/graphene passivated InSe sheet exceed 10^3 $cm^2\ V^{-1}S^{-1}$ at room temperature. [224, 225] Based on the density functional theory calculations, the bandgap of InSe transform from direct to indirect semiconductors as the number of layers decreases. [226, 227] Thus indium selenide has a great prospective for optoelectronic applications. [228, 229]

The experimental results evidence that the thinner InSe films rapid oxidative degradation. At ambient conditions some small molecules (O_2, CO, H_2O and NO_2) are always interact with the surface of two-dimensional nanomaterials. These small molecules can modify the electronic and optical properties of two-dimensional nanomaterials. The lone-pair states of Se at the top of the valence band of indium selenide make high sensitivity to the external adsorbate. [223] Since high electrical conductivities, the molecular adsorption changed electrical conductivity [217, 230], gas sensors based on graphene have some practical applications [231-234]. It is found that a certain amount of electrons transferred between the adsorbed molecules on the InSe monolayer and the substrates. [235] Other works have reported positive adsorption energy of H_2O molecules on Se vacancies, [236] the different adsorption sites of the InSe surface for the physisorption of oxygen almost zero adsorption energy. [235] Another works provides experimental and theoretical evidences of chemical stability of InSe-monolayers.

Possible cause of this contradictions between results of the theoretical modelling is using of different types of the optimization of substrates and different sized of supercells that could be crucial for the modelling of flexible membranes. Some works reports results for 3×3 InSe supercells [234,124] other for 4×4 [222,223,235] that is corresponding with coverage by impurities 11.1% and 6.3% of the surface. Additionally, in some works were used only optimization of the atomic positions for fixed lattice parameters [235] other groups report results after optimization of both atomic positions and lattice parameters. [222,223,124] The first case will further denote as ‘optimization positions’ can be discussed as the model of the surface of bulk of InSe and similar crystals or monolayer on rigid substrate. The second approach will further denote as ‘optimization all’ is corresponding with the case of free standing membrane. For evaluate the contribution from the different approach to the modelling and concentration of impurities we have performed the modeling of the adsorption of the molecules of four species (O_2, CO, H_2O, NO_2) on 2×2, 3×3 (see Fig. 6.2.1a,b) and 4×4 InSe supercells with using of the ‘optimization positions’ and ‘optimization all’ modes. For make our modelling more comprehensive we have performed modeling of the adsorption over uniaxial strained and compressed at 1% 4×4 supercell and ripple created from 4×4 supercell (Fig. 6.2.1c). This last part of our work provides evaluation of the contribution from substrate to adsorption properties of InSe membrane.

At the present calculations, we selected In $5s^2 5p^1$, Se $4s^2 4p^4$, O $2s^2 2p^4$, C $2s^2 2p^4$, N $2s^2 2p^4$, H $1s^1$ configuration as the valence states. The special points sampling integration over the Brillouin zone was performed using a k-mesh of dimensions $2 \times 2 \times 1$ k-points mesh according to a Monkhorst–Pack scheme.

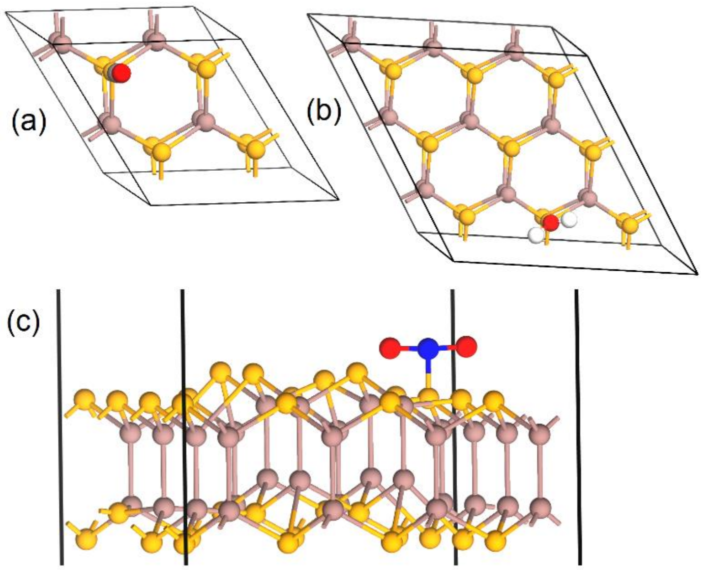

Figure 6.2.1 – Optimized atomic structures of CO adsorbed on 2×2 supercell of InSe (a), water adsorbed on 3×3 supercell of InSe (b) and NO_2 adsorbed in vicinity of the ripple in 4×4 supercell of InSe (c).

Calculation of the absorption were performed by the formula:

$$I = I_0 e^{-\alpha x} \qquad (6.2.1)$$

where I is the intensity of transmitted light, I_0 is the intensity of incident light, α is the absorption coefficient, and *x* is the thickness of the absorbent medium. A bundle of monochromatic light was irradiated onto the surface of an absorbing medium. After passing through a medium of a certain thickness, the intensity of the transmitted light was weakened because the medium absorbed a part of the light energy.

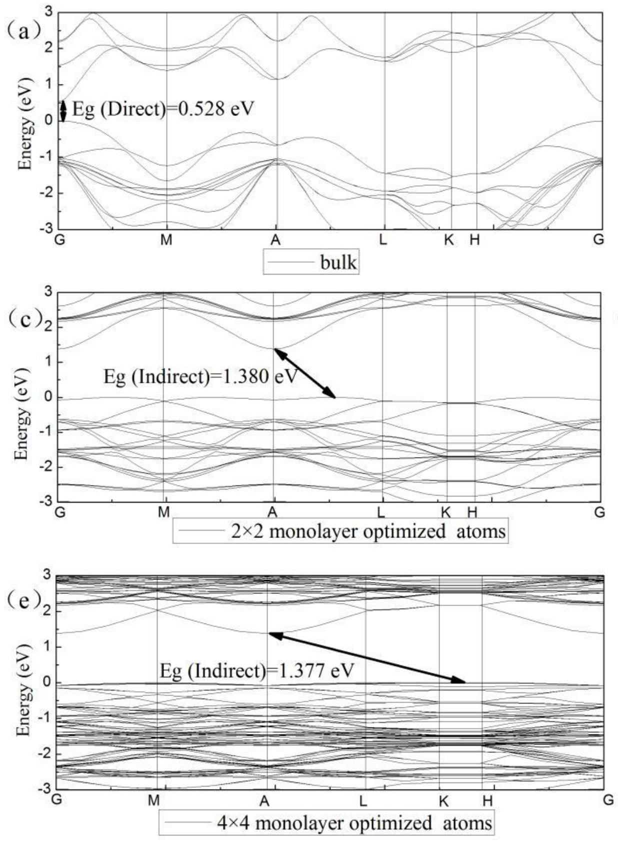

Figure 6.2.2 – Band structure of bulk (a) and monolayer (b) of InSe before optimization and 2×2 (c,d) and 4×4 (e,f) supercells after optimization of atomic positions (c,e) and lattice parameters and atomic positions (d,f).

At the first step of our modeling we check the influence of the supercell size and optimization mode on electronic structure and optical properties. Results of the calculations demonstrate that optimization the only atomic positions provide breaking of the symmetry for all considered supercells. The mean displacement of the atoms from ideal positions is 0.013, 0.006 and 0.005 Å for 2×2, 3×3 and 4×4 supercells respectively. Surprisingly but the break of the symmetry does not provides significant changes in the values of DFT-bandgap (see Fig. 6.2.2b,c,e). In the case of the optimization of both lattice parameters and atomic positions lattice parameters is insignificantly decreased. The values of the mean displacement of the atoms is increased comparable to the optimization of the only atomic positions up to 0.075, 0.067 and 0.066 Å for discussed supercells. These changes in crystal structure provides not the only increasing of the number of bandlines but also increasing of the value of DFT-bandgap up to 2 eV (Fig. 6.2.2d,f). Note that DFT calculations are performing at zero temperature therefore at room temperature deviations of the atoms from ideal positions should be larger. From the other hand these displacement of the atoms is small enough and does not provides visible influence on optical properties of InSe such as absorption function (see Fig. 6.2.3a).

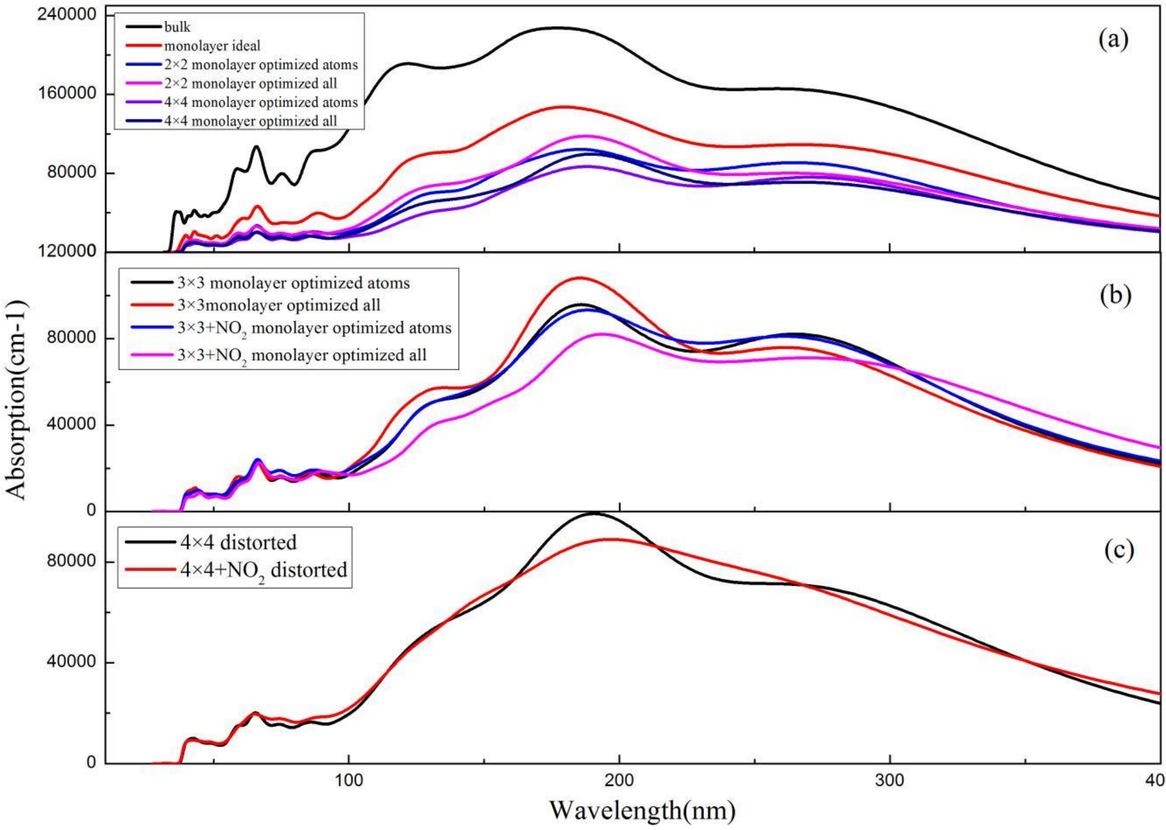

Figure 6.2.3 – Absorption coefficient for various InSe substrates without adsorbed gases (a),
before and after adsorption of NO_2 (b)
and after formation of the ripple and further adsorption of NO_2 (c)

6.3 The effect of adsorption on the electronic structure and optical properties of indium selenide

Adsorption energies were calculated by standard formula:

$$E_{ads} = E_{InSe+mol} - [E_{InSe} + E_{mol}] \tag{6.3.1}$$

where E_{InSe} in the total energy of InSe supercell before attachment of m atoms. The calculations of E_{mol} were performed for the single molecule within the supercell of the same size. In this approach to the calculation of E_{mol} the interactions between molecules adsorbed on InSe is excluded from adsorption energies and the values of these energies characterize only InSe-molecule interactions.

Table 6.3.1 – Calculated energies of the adsorption on various molecules on InSe undistorted substrates (meV/mol), distance between molecule and InSe (d) and mean displacement (D) both in Å. The first numbers in the cells is corresponding with optimization of the only atomic positions and the second (after slash) with optimization of atomic positions and lattice parameters.

Adsorbant	Supercell	E_{ads}	d	D
O_2	2×2	-748 / -851	3.214 / 3.475	0.036 / 0.032
	3×3	-702 / -762	3.192 / 3.058	0.017 / 0.013
	4×4	-756 / +1,079	3.281 / 2.916	0.005 / 0.010
CO	2×2	+70 / +918	3.409 / 2.620	0.034 / 0.051
	3×3	+72 / +101	3.419 / 3.340	0.014 / 0.012
	4×4	+1,269 / +452	3.102 / 4.019	0.009 / 0.103
H_2O	2×2	+123 / +84	3.134 / 3.301	0.042 / 0.041
	3×3	+756 / +380	3.041 / 3.702	0.019 / 0.167
	4×4	+1,171 / +589	2.948 / 4.002	0.009 / 0.098
NO_2	2×2	+1,432 / +1,383	2.523 / 3.278	0.048 / 0.308
	3×3	-15 / -944	2.248 / 2.392	0.022 / 0.136
	4×4	+282 / +1,108	2.276 / 4.002	0.014 / 0.130

The next step of our modelling is the modelling of the energetics of the adsorption of various molecules. Results of the calculations demonstrate that in the case of adsorption of molecular oxygen the process is always energetically favorable except adsorption of 4×4 supercell with optimized both lattice parameters and atomic positions. This result is in agreement with experimentally observed stability of free-standing InSe monolayer at ambient conditions. [124,237] Decreasing of the size of supercell is corresponding with increasing of the concentration of the oxygen. Thus in the case of high pressure of the oxygen or air chemical degradation of free-standing InSe monolayer could occur. In the case of the optimization of the only atomic positions adsorption of molecular oxygen is favorable. This type of the optimization can be discussed as the model for the oxidation of the monolayer on substrate or the surface of bulk or few layers of layered materials because the presence of substrate makes top layer rigid. Thus obtained in calculations favorable adsorption of the oxygen in the case of optimization of the only atomic positions is also in qualitative agreement with experimentally observed oxidative degradation of few-layers of InSe. [114]

In the case of adsorption of carbon monoxide and water picture is similar: physical adsorption is strongly unfavorable. Almost for all cases and both types of the optimizations decreasing of the concentration of the adsorbants realized via increasing of the supercell size leads to increasing of the adsorption energy. To understand the difference between adsorption of molecular oxygen and these two gases we have checked mean displacement of the atoms if the substrate. Results of the calculations demonstrate correlation between magnitude of mean displacement and unfavorability of the adsorption. The cause of smaller distortions of the substrate after adsorption of the oxygen is sp^1 hybridization in molecular oxygen that permit fill empty *5p* shells of selenium by lone pairs on *2p* orbitals of the oxygen. In the case of carbon monoxide and especially in the case of water formation of this kind of bond leads to reorientation of the *sp*-orbitals of selenium and as results to larger distortions of InSe substrate. The energy cost of these distortions overcome energy gain from the filing of the empty 5p orbitals of one selenium atoms by electrons from adsorbed molecules. Note that different types of the optimization lead to the different magnitudes of mean displacement of the atoms in substrate.

The last adsorbant considered in our work is nitrogen dioxide. The combination of the oxygen atoms with lone pairs of the electrons and partially empty *2p* orbitals of nitrogen. Results of the calculations demonstrate that at moderate concentrations (3×3 supercell) adsorption of NO_2 is favorable similarly to the adsorption of oxygen and at high and low concentrations adsorption is unfavorable similarly to the water and carbon monoxide. Note that in the case of favorable adsorption on 3×3 supercell the difference in the magnitudes of the adsorption energies is much larger than in the case of the adsorption of molecular oxygen. The values of mean displacements are also rather different.

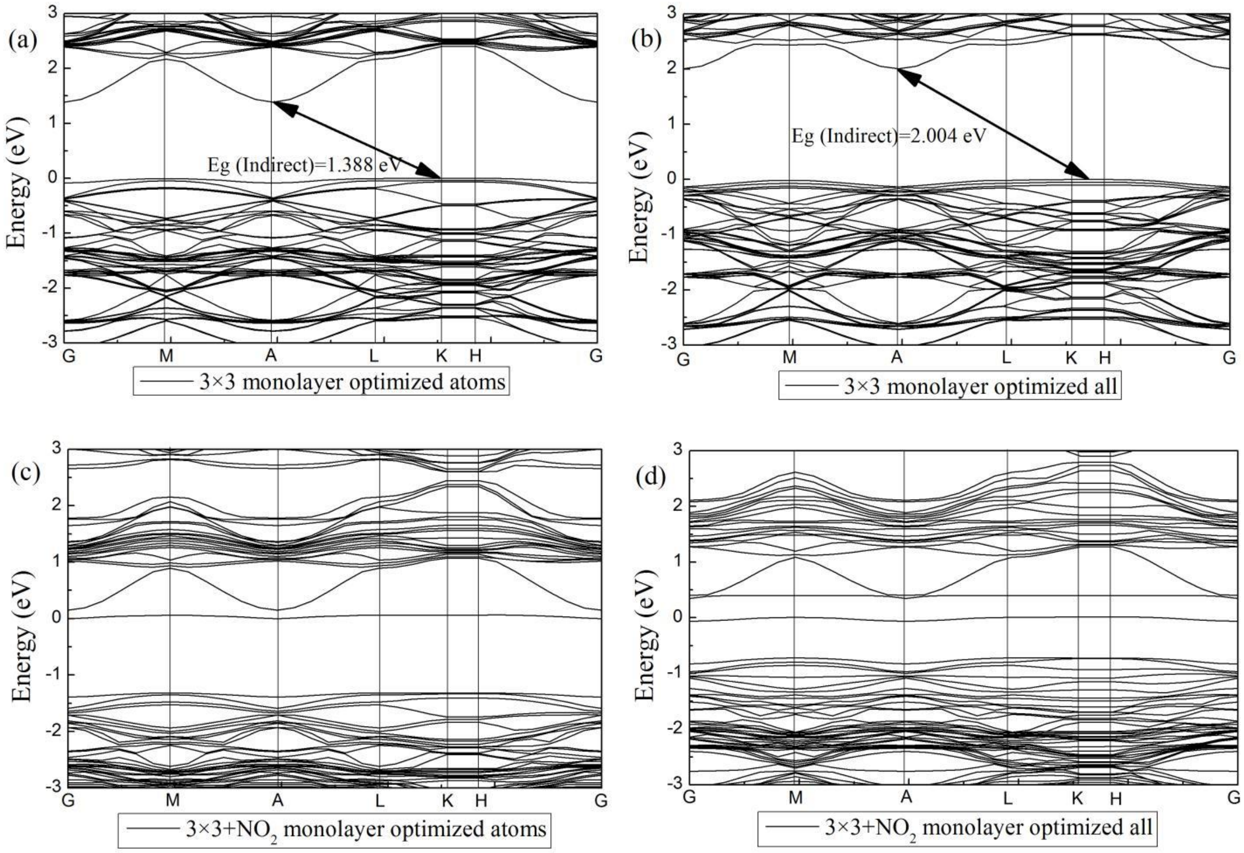

Figure 6.3.1 – Band structure of 3×3 supercell of InSe after optimization of the only atomic positions (a,c) and optimization of lattice parameters and atomic positions (b,d) before (a,b) and after (c,d) adsorption of NO_2.

These different patterns of the interactions of NO_2 with 3×3 supercell of InSe also leads to the difference in the molecular levels of the adsorbant. The band structure of InSe substrate remain almost the same after adsorption of NO_2 for both types of the optimization (see Fig. 6.3.1). But in the case of the optimization only atomic positions we can see degenerate orbital on the Fermi level (Fig. 6.3.1c) and in the case of the optimization of lattice parameters and atomic positions occur split of these levels to occupied and unoccupied (Fig. 6.3.1d) that significantly increase favorability of the adsorption. For make our survey more comprehensive we checked the influence of the adsorption on the optical properties of the systems. Results of the calculations (Fig. 6.2.3b) demonstrate that similarly to the insignificant changes of the band structure of InSe substrate absorption functions is also remain almost the same.

6.4 The effect of additional distortion of the InSe-substrate on molecular adsorption.

Table 6.4.1 – Calculated energies of the adsorption on various molecules on InSe distorted substrates (meV/mol), distance between molecule and InSe (d) and mean displacement (D) both in Å. All results are reported for 4×4 supercell.

Substrate Distortion	Adsorbant	E_{ads}	d	D
Stretch 1%	O_2	+769	2.739	0.010
	CO	+61	3.336	0.009
	H_2O	-411	2.836	0.008
	NO_2	+742	2.206	0.011
Compression 1%	O_2	+535	3.136	0.016
	CO	+362	3.111	0.010
	H_2O	+480	2.622	0.007
	NO_2	+1,384	2.105	0.009
Ripple	O_2	+1,134	2.401	0.039
	CO	-3	3.192	0.013
	H_2O	+547	2.503	0.030
	NO_2	+83	2.277	0.034

Results presented in previous paragraphs demonstrate that InSe-monolayer is extremely flexible materials. Fixation of lattice parameters significantly influence structural, electronic and chemical properties of this materials. Deposition of the monolayer on rigid scaffold can provides not only fixation of the lattice parameters but also change the value of the lattice parameters. To evaluate contribution from the changes of lattice parameters we performed the calculations of the adsorption of four previously considered types of molecules on 4×4 supercell after uniaxial stretch at 1% and compression at 1%. Note that in this case lattice parameters are fixed and only atomic positions are optimizing. Results of the calculations (Tab. 6.4.1) evidence that planar distortion of the substrate change energetics of the adsorption. Adsorption of the oxygen became unfavorable in both cases (stretch and compression of the substrate) and adsorption of the water became favorable on stretched substrate. Foe all considered adsorpbant distance between substrate and molecule became smaller (see Tab. 6.3.1 and 6.4.1) and mean displacement of the atoms in substrate from initial positions is almost the same in the case of stretch of the surface and larger when substrate compressed. This even very small in-pane distortion of InSe substrate can significantly influence its chemical properties.

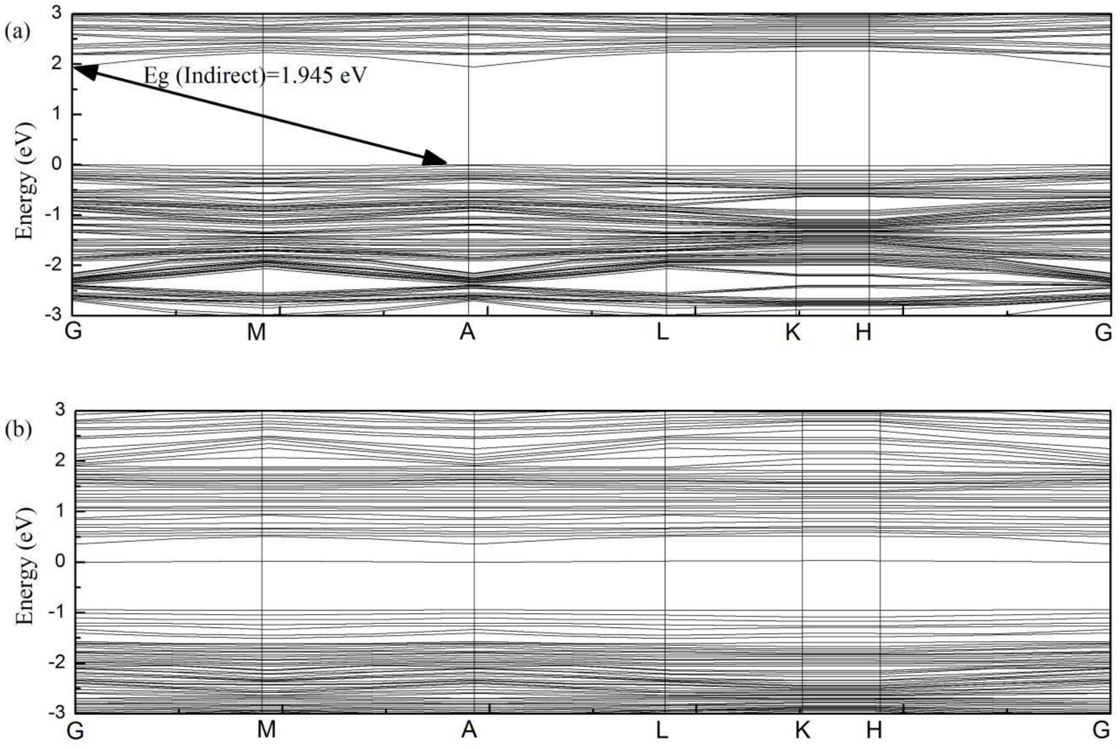

Figure 6.4.1 – Band structure of 4×4 rippled supercells of InSe before (a) and after (b) adsorption of NO_2.

Another type of distortion of InSe membrane that can be induced by scaffold is formation of the ripples. Note that this ripples can be also induced by thermal fluctuation of free-standing membrane. [238] Our previous work demonstrate that the presence of the ripple in graphene substrate can change energetics of physical adsorption of the molecules. [239] For the building of the model ripple we uniaxially compress 4×4 supercell at 5% and push up several atoms in the center of the supercell. This initial structure was further optimized with fixed lattice parameters. In-plane compression of the supercell is essential for preventing the return of shifted atoms in initial positions (see Fig. 6.2.1c). Formation of the ripple does not change significantly band structure (see Figs. 6.2.2f and 6.4.1a) and optical properties (see Fig. 6.2.3a,c) of InSe monolayer. Distortion of InSe substrate predictable influence energetics of the adsorption and mean displacement of the atoms in membrane (see Tab. 6.4.1). Similarly to the adsorption of the molecules on in-plane distorted membrane distance between adsorbants and substrate is smaller than in the case of adsorption on non-distorted InSe membrane. Another difference between these two cases is the influence of the adsorption on band structure of the substrate. In the case of non-distorted substrate band structure of InSe remain almost the same before and after adsorption of NO_2 (Fig. 6.3.1). Adsorption of the same molecule near the ripple provides decreasing of DFT-bandgap at the value at about 0.5 eV and almost flattened the lines in valence bands (see Fig. 6.4.1). The nature of these effects is stronger adsorption-induced displacements of the atoms of rippled substrate (see results for the calculations with fixed lattice parameters in Tab. 6.3.1 and Tab. 6.4.1).

6.5 Conclusion

The simulation results presented in our works demonstrate that the energetics of physical (non-covalent) adsorption of various molecules on an InSe monolayer strongly depends on the size of the supercell and especially on the optimization mode. Calculations with optimization of the only atomic positions report robust adsorption of the oxygen at any concentrations contrary to the calculations with optimization of lattice parameters and atomic positions, which report unfavorability of the adsorption at low concentration of the oxygen. In-plane and out-of-plane distortion of InSe membrane makes adsorption of molecular oxygen unfavorable in contrast to adsorption of water and carbon monoxide. Difference in the energetics and favorability of the adsorption can be discussed as the balance between energy gain from the formation of non-covalent bonds between adsorbants and selenium atoms and energy costs of distortion of the substrate created by formation of this bond. Based on results of our calculations we can conclude that chemical stability of such flexible membrane as indium selenide is strongly depends from multiple conditions such as the presence of the substrate, distortions created by the substrate and concentration of the adsorbants. Thus disagreement between previous experimental and theoretical works can be caused differences in experimental conditions and in modes of the calculations used by different theoretical teams. Our results demonstrate that for very flexible materials all distortions-related factors should be taken into account in interpretation of experimental results and theoretical modeling.

CONCLUSION

In this dissertation we report results of the modeling of the atomic structure of novel materials for optics, electronics and photoelectronics based on oxide and low-dimensional systems and the formation of a systematic description of the relationship between the morphology of the material. For maximum consistency, we studied materials with the most different morphology (large nanoparticles, nanoclusters, two-dimensional membranes) and physical properties (semiconductors and conductors), both realistic and hypothetical (two-dimensional boron). Chemical stability of studied materials and the effect of modification in various ways (doping, creating defects, surface oxidation, etc.) on electronic structure and optical properties of materials for use in catalysis, sensing, solar energy conversion and storage technologies have been investigated. In low-dimensional systems, the contribution from the surface and the influence of doping of near-surface regions, the shape and defects of the surface, and changes in the surface structure after modification are taken into account and the contribution from the adsorption of molecules on the surface is inevitable, so we selected the most representative representatives of various classes of low-dimensional materials(zinc oxide, β-C_3N_4, indium selenide, borophene) and simulated the influence of various processing methods and the influence of the environment on the physical properties of these materials.

Zinc oxide usually forms large nanoparticles with a structure identical to the array and a small contribution of the surface to physical properties. Therefore, to simulate zinc oxide nanoparticles, a supercell of the ZnO array can be used under periodic boundary conditions. Zinc oxide doped with beryllium can be used in UV photovoltaic equipment. Based on our calculations, we have demonstrated that doping can increase the efficiency of photoactive materials. In our work, we investigated the relationship between the atomic structure and optical properties of zinc oxide doped with beryllium ($Zn_{x-1}Be_xO$) for various beryllium concentrations. The results show that the lattice parameters are nearly linear and obey Vegard's law. After correcting the band gap value, the electronic band gap is consistent with the experimental results, which once again shows the adequacy of the model chosen for modeling large nanoparticles. The results of the density of states for $Be_xZn_{1-x}O$ show that as Be doping the contribution of zinc and beryllium in the conduction band position constantly moving to higher energy region, make the band gap width of $Be_xZn_{1-x}O$ increases. The blue shift of absorption spectrum of the system becomes more pronounced after increasing the concentration of Be. A key factor influencing the change in the optical properties of the $Be_xZn_{1-x}O$ system is a change in the lattice parameters due to a change in the impurity concentration.

The next step in our research was the study of smaller nanoparticles and nano-clusters. For this purpose, one of the allotropies of carbon nitride β-C_3N_4 was chosen, which forms nanoparticles with an atomic structure close to that of an array, but with a large contribution from the surface due to the small size of nanoparticles. In the course of our work, we performed first-principles modeling of the optical and chemical properties of β-C_3N_4 in the bulk (pristine and defected), surface and nanoclusters. We have demonstrated the significant sensitivity of absorption spectra of β-C_3N_4 to any kinds of disorder in atomic structure. The formation and passivation of the surface as a result of interaction with the environment provides similar changes in optical properties. The value of the indirect bandgap depends on the chemical structure of the surface. Functionalization of the active sites on the surface by monovalent species (hydrogen and fluorine) leads to vanishing of the bandgap in the case of (001) surface and changes the value of the bandgap in the case of nanoclusters. Results of our calculations also demonstrate the appearance of magnetic moments in hydrogenated and fluorinated (001) surface of β-C_3N_4. The main contribution to the change in the optical properties of β-C_3N_4 is made by the deviation of the atomic structure from ideal. The minimum disordering with a standard deviation of 0.03 Å atoms from stoichiometric positions is sufficient to change the reflection and absorption spectra of β-C_3N_4. Modification of defects on the β-C_3N_4 surface does not lead to significant changes in these functions, but it can lead to a significant change in the energy gap between the valence and conduction bands.

The next object of our research was chosen with the calculation of a decrease in dimension and an increase in the contribution from the surface. Since the atomic structure, defects and chemical modification of the surface of such materials as graphene, boron nitride and molybdenum disulfide are described in sufficient detail, two-dimensional boron allotropes would be chosen as the object of study. Dozens of recent theoretical works have been devoted to this class of materials, but in all these works the chemical stability of the materials under study has not been investigated. A single-layer boron membrane (borophene), various allotropes of which have an atomic structure different from boron crystals, and which, unlike other systems under study, is a conductor. A step-by-step modeling of the oxidation of various types of boron monolayers was performed. Results of the calculations demonstrate that the process of the oxidation is always exothermic and lead toward the formation of foam-like boron oxide films with incorporated non-oxidized small boron clusters. Some of these boron-oxide films demonstrate the presence of chemically stable magnetic centers. Oxidation of borophene leads to the transformation of its electronic structure from metal to semiconductor, which makes it a promising material for building flexible solar harvesting devices. Moreover, in some kinds of borophene sheets oxidation provide the appearance of stable at ambient condition *d0*-magnetism caused by unpaired electrons on single non-oxidized boron atoms. Stable physical adsorption of various gases on oxidized borophene sheets leads to the changes in optically active part of borophene spectra that make this material attractive for gas photo-detectors. Calculated barrier of the migration of hydrogen protons and atomic hydrogen throughout the pores of oxidized borophene demonstrates impermeability of the membrane for both considered species that make possible usage of oxidized borophene as hydrogen-leakage preventing coating.

We applied the approaches and skills developed in the course of modeling the interaction of borophene with the environment to another two-dimensional object - indium selenide. This material is obtained by exfoliating three-dimensional van der Waals crystals, but the chemical stability of the obtained single layers is still in question. Indium selenide represents a system of layers connected by weak non-covalent bonds, which are easily exfoliated in liquids to form a single-layer membrane. Calculated adsorption energies of various gases on the surface of a single-layer indium selenide depend on whether optimization has been made only of atomic positions (which is corresponding to the case of monolayer on a substrate) or of atomic positions and lattice parameters (which is corresponding to the case of a free membrane). The effect of crystal lattice distortions (strain and buckling) on the optical properties of a single-layer indium selenide membrane (InSe) and the adsorption of molecules on its surface was studied. A relationship has been established between the adsorption properties of a single-layer indium selenide and membrane flexibility. Our results demonstrate that for very flexible materials all distortions-related factors should be taken into account in interpretation of experimental results and theoretical modeling.

In addition to studying the effect of dimensionality reduction on changes in the physical and chemical properties of materials important for practical application, our work demonstrates the need for mandatory verification of changes in the atomic structure of low-dimensional materials as a result of interaction with the environment, as well as the importance of taking into account all the degrees of freedom of two-dimensional membranes in modeling their chemical properties. Both of these methodological results are important for the modeling of other low-dimensional systems and the development of theoretical materials science.

The author expresses his deep gratitude to the scientific consultant D.V. Bukhvalov for invaluable help and support in the preparation of this work.

LIST OF REFERENCES

1. Geim, A. K. Van der Waals heterostructures / A. K. Geim, I. V. Grigorieva // Nature. – 2013. – V. 499. – P. 419-425.
2. Wallbank, J. R. Tuning the valley and chiral quantum state of Dirac electrons in van der Waals heterostructures / J. R. Wallbank, D. Ghazaryan, A. Misra, Y. Cao, J. S. Tu, B. A. Piot, M. Potemski, S. Pezzini, S. Wiedmann, U. Zeitler, T. L. Lane, S. V. Morozov, M. T. Greenaway, L. Eaves, A. K. Geim, V. I. Fal'ko, K. S. Novoselov, A. Mishchenko // Science. – 2016. – V. 353. – P. 575-579.
3. Withers, F. Light-emitting diodes by band-structure engineering in van der Waals heterostructures / F. Withers, O. Del Pozo-Zamudio, A. Mishchenko, A. P. Rooney, A. Gholinia, K. Watanabe, T. Taniguchi, S. J. Haigh, A. K. Geim, A. I. Tartakovskii, K. S. Novoselov // Nature Materials. – 2015. – V. 14. – P. 301-306.
4. Chang, J. S. Multi-dimensional zinc oxide (ZnO) nanoarchitectures as efficient photocatalysts: What is the fundamental factor that determines photoactivity in ZnO? / J. S. Chang, J. Strunk, M. N. Chong, P. E. Poh, J. D. Ocon // J. Hazard. Mater. – 2020. – V. 381. – № 120958.
5. Ong, C. B. A review of ZnO nanoparticles as solar photocatalysts: Synthesis, mechanisms and applications / C. B. Ong, L. Y. Ng, A. W. Mohammad // Renew. Sust. Energ. Rev. – 2018. – V. 81. – P. 536-551.
6. Bharat, T. C. Synthesis of Doped Zinc Oxide Nanoparticles: A Review / T. C. Bharat, Shubham, S. Mondal, H. S. Gupta, P. K. Singh, A. K. Das // Materials Today: Proceedings. – 2019. – V. 11. – P. 767-775.
7. Theerthagiri, J. A review on ZnO nanostructured materials: energy, environmental and biological applications / J. Theerthagiri, S. Salla, R. A. Senthil, P. Nithyadharseni, A. Madankumar, P. Arunachalam, T. Maiyalagan, H. S. Kim // Nanotechnology. – 2019. – V. 30. – № 392001.
8. Leedahl, B. Study of the Structural Characteristics of 3d Metals Cr, Mn, Fe, Co, Ni and Cu implanted in ZnO and TiO_2 - experiment and Theory / B. Leedahl, D. A. Zatsepin, D. W. Boukhvalov, E. Z. Kurmaev, R. J. Green, I. S. Zhidkov, S. S.

Kim, L. Cui, N. V. Gavrilov, S. O. Cholakh, A. Moewes // J. Phys. Chem. C. – 2014. – V. 118. – P. 28143-28151.

9. Torquato, S. Random heterogeneous materials: microstructure and macroscopic properties / S. Torquato, H. Haslach // Appl. Mech. Rev. – 2002. – V. 55. – P. B62-B63.
10. Tran, A. V. Reliable molecular dynamics: uncertainty quantification using interval analysis in molecular dynamics simulation / A. V. Tran, Y. Wang // Comput. Mater. Sci. – 2017. – V. 127. – P. 141-160.
11. Grudimn, S. Practical modeling of molecular systems with symmetries / S. Grudimn, S. Redon // J. Comput. Chem. – 2010. – V. 31. – P. 1799-1814.
12. Serrano, E. Nanotechnology for sustainable energy / E. Serrano, G. Rus, J. García-Martínez // Renew. Sust. Energ. Rev. – 2009. – V. 13. – P. 2373-2384.
13. Vandenbosch, Guy A. E. Upper bounds for the solar energy harvesting efficiency of nano-antennas / Guy A. E. Vandenbosch, Z. K. Ma // Nano Energy. – 2012. – V. 1. – P. 494-502.
14. Yunus, I. S. Nanotechnologies in water and air pollution treatment / I. S. Yunus, Harwin, A. Kurniawan, D. Adityawarman, A. Indarto // Environmental Technology Reviews. – 2012. – V. 1. – P. 136 -148.
15. Mohamed, E. F. Nanotechnology: Future of Environmental Air Pollution Control / E. F. Mohamed // Environmental Management and Sustainable Development. – 2017. – V. 6. – P. 2164-7682.
16. Ikoba, U. Nanocarriers in therapy of infectious and inflammatory diseases / U. Ikoba, H. S. Peng, H. C. Li, C. Miller, C. X. Yu , Q. Wang // Nanoscale. – 2015. – V. 7. – P. 4291-4305.
17. Boulaiz, H. Nanomedicine: Application Areas and Development Prospects / H. Boulaiz, P. J. Alvarez, A. Ramirez, J. A. Marchal, J. Prados, F. Rodríguez-Serrano, M. Perán, C. Melguizo, A. Aranega // Int. J. Mol. Sci. – 2011. – V. 12. – P. 3303-3321.
18. Singh, L. The role of nanotechnology in the treatment of viral infections / L. Singh, H. G. Kruger, G. E. M. Maguire, T. Govender, R. Parboosing // Ther. Adv.

Infectious. Dis. – 2017. – V. 4. – P. 105-131.

19. Stone, J. E. GPU-accelerated molecular modeling coming of age / J. E. Stone, D. J. Hardy, I. S. Ufimtsev, K. Schulten // J. Mol. Graph. and Model. – 2010. – V. 29. – P. 116-125.
20. Kundoo, S. Synthesis of crystalline carbon nitride thin films by electrolysis of methanol–urea solution / S. Kundoo, A. N. Banerjee // Mater. Lett. – 2002. – V. 57. – P. 2193-2197.
21. Yu, D. L. Synthesis of graphite-C3N4 crystal by ion beam sputtering / D. L. Yu, F. R. Xiao, T. S. Wang // J. Mater. Sci. Lett. – 2000. – V. 19. – P. 553-556.
22. Sharma, A. K. Synthesis of crystalline carbon nitride thin films by laser processing at a liquid-solid interface / A. K. Sharma, P. Ayyub, M. S. Multani // Appl. Phys. Lett. – 1996. – V. 69. – P. 3489-3491.
23. Niu, C. Experimental realization of the covalent solid carbon nitride / C. Niu, Y. Z. Lu, C. M. Lieber // Science. – 1993. – V. 261. – P. 334-337.
24. Montigaud, H. C3N4: Dream or reality? Solvothermal synthesis as macroscopic samples of the C_3N_4 graphitic form / H. Montigaud, B. Tanguy, G. Demazeau // J. Mater. Sci. – 2000. – V. 35. – P. 2547-2552.
25. Teter, D. M. Low-Compressibility Carbon Nitrides / D. M. Teter, R. J. Hemley // Science. – 1996. – V. 271. – P. 53-55.
26. Xu, M. S. Graphene-Like Two-Dimensional Materials / M. S. Xu, T. Liang, M. M. Shi, H. Z. Chen // Chem. Rev. – 2013. – V. 113. – P. 3766-3798.
27. Balendhran, S. Elemental analogues of graphene: silicene, germanene, stanene, and phosphorene / S. Balendhran, S. Walia, H. Nili, S. Sriram, M. Bhaskaran // Small. – 2015. – V. 11. – P. 640-652.
28. Ferrari, A. C. Science and technology roadmap for graphene, related two-dimensional crystals, and hybrid systems / A. C. Ferrari, F. Bonaccorso, V. Fal’ko, K. S. Novoselov, S. Roche, P. Bøggild, S. Borini, F. H. Koppens, V. Palermo, N. Pugno // Nanoscale. – 2015. – V. 7. – P. 4598-4810.
29. Yang, W. Two-dimensional layered nanomaterials for gas-sensing applications / W. Yang, L. Gan, H. Li, T. Zhai // Inorg. Chem. Front. – 2016. – V. 3. – P. 433-

451.

30. Heurich, J. Electrical Transport through Single-Molecule Junctions: From Molecular Orbitals to Conduction Channels / J. Heurich, J. C. Cuevas, W. Wenzel, and G. Schön // Phys. Rev. Lett. – 2002. – V. 88. – № 256803.
31. Cuevas, J. C. Towards a theory of electrical transport through atomic and molecular junctions / J. C. Cuevas, J. Heurich, F. Pauly, W. Wenzel, G. Schon // Phase Transitions. – 2004. – V. 77. – P. 175-189.
32. Cuevas, J. C. Theoretical description of the electrical conduction in atomic and molecular junctions / J. C. Cuevas, F. Pauly, J. Heurich, W. Wenzel, and G. Schon // Nanotechnology. – 2003. – V. 14. – P. R29-R38.
33. Grabowski, B. Ab initio up to the melting point: Anharmonicity and vacancies in aluminum / B. Grabowski // Phys. Rev. B. – 2009. – V. 79. – № 134106.
34. Nicholls, R. J. Probing the bonding in nitrogen-doped graphene using electron energy loss spectroscopy / R. J. Nicholls, A. T. Murdock, J. Tsang, J. Britton, T. J. Pennycook, A. Koós, P. D. Nellist, N. Grobert, J. R. Yates // ACS Nano. – 2013. – V. 7. – P. 7145-7150.
35. Vosko, S. H. Ab Initio Calculation of the Spin Susceptibility for the Alkali Metals Using the Density-Functional Formalism / S. H. Vosko, J. P. Perdew // Phys. Rev. Lett. – 1975. – V. 35. – P. 1725-1728.
36. Xiong, K. Defect energy levels in HfO_2 high-dielectricconstant gate oxide / K. Xiong, J. Robertson, M. C. Gibson, S. J. Clark // Appl. Phys. Lett. – 2005. – V. 87. – № 183505.
37. Zhang, W. B. Stability and magnetism of vacancy in NiO: a GGA+U study / W. B. Zhang, N. Yu, W. Y. Yu, B. Y. Tang // Phys. J. B. – 2008. – V. 64. – P. 153-158.
38. Hasnip, P. J. Ab initio studies of disorder in the full Heusler alloy $Co_2Fe_xMn_{1-x}Si$ / P. J. Hasnip, J. H. Smith, V. K. Lazarov // J. Appl. Phys. – 2013. – V. 113. – № 17B 106.
39. Birch, Finite Elastic Strain of Cubic Crystals / Birch, Francis // Phys. Rev. – 1947. – V. 71. – P. 809-824.

40. Jaffe, J. E. Ab initio high pressure structural and electronic properties of ZnS / J. E. Jaffe, R. Pandey, M. J. Seel // Phys. Rev. B. – 1993. – V. 47. – P. 6299-6303.
41. Samara, G. A. Pressure induced phase transitions in some II–VI compounds / G. A. Samara, H. G. Drickamer // J. Phys. Chem. Solids. – 1962. – V. 23 – P. 457-461.
42. Peutzfeldt, A. Surface hardness and wear of glass ionomers and compomers / A. Peutzfeldt, F. Garcia-Godoy, E. Asmussen Am J Dent // Am. J. Dent. – 1997. – V. 10 – P. 15-17.
43. Shahdad, S. A. Hardness measured with traditional Vickersand Martens hardness methods / S. A. Shahdad, J. F. McCabe, S. Bull, S. Rusby, R. W. Wassell // Dent. Mater. – 2007. – V. 23 – P. 1079-1085.
44. Yun, F. Energy band bowing parameter in $Al_xGa_{1-x}N$ alloys / F. Yun, M. A. Reshchikov, L. He, T. King, H. Morkoç // . Appl. Phys. – 2002. – V. 92 – P. 4837-4839.
45. Wu, G. M. Crystal quality and electrical properties of p-type GaN thin film on Si(111) substrate by metal-organic chemical vapor deposition MOCVD / G. M. Wu, T. H. Hsieh // J. Achiev. Mater. Manuf. Eng. – 2007. – V. 24 – P. 193-197.
46. Yu, P. Room Temperature Stimulated Emission from ZnO Quantum Dot Films / P. Yu, Z. K. Tang, G. K. L. Wong, M. Kawasaki // Physics of semiconductors. – 1996. – V. 1 – P. 1453-1456.
47. Janotti, A. Fundamentals of zinc oxide as a semiconductor / A. Janotti, C. G. Van de Walle // Rep. Prog. Phys. – 2009. – V. 72 – № 126501.
48. Liu, Z. W. Scaling behavior and coarsening transition of annealed ZnO films on Si substrate / Z. W. Liu, W. J. Fu, M. Liu, J. F. Gu, C. Y. Ma, Q. Y. Zhang // Surf. Coat. Technol. – 2008. – V. 202 – P. 5410-5415.
49. Bagnall, D. M. Optically pumped lasing of ZnO at room temperature / D. M. Bagnall, Y. F. Chen, Z. Zhu, T. Yao, S. Koyama, M. Y. Shen, T. Goto // Appl. Phys. Lett. – 1997. – V. 70 – P. 2230-2232.
50. Aoki, T. ZnO diode fabricated by excimer-laser doping / T. Aoki, Y. Hatanaka // Appl. Phys. Lett. – 2000. – V. 76 – P. 3257-3258.

51. Zhang, X. D. First-pinciples study of electronic and optical properties in wurtzite $Zn_{1-x}Cd_xO$ / X. D. Zhang, M. L. Guo, W. X. Li, C. L. Liu // J. Appl. Phys. – 2008. – V. 103 – № 063721.
52. Liu, Y. Ultraviolet detectors based on epitaxial ZnO films grown by MOCVD / Y. Liu, C. R. Gorla, S. Liang, N. Emanetoglu, Y. Lu, H. Shen, M. Wraback // J. Electron. Mater. – 2000. – V. 29 – P. 69-74.
53. Ohtomo, A. Structure and optical properties of $ZnO/Mg_{0.2}Zn_{0.8}O$ superlattices / A. Ohtomo, M. Kawasaki, I. Ohkubo, H. Koinuma, T. Yasuda, Y. Segawa // Appl. Phys. Lett. – 1999. – V. 75 – P. 980-982.
54. Makino, T. Radiative and nonradiative recombination processes in lattice-matched (Cd,Zn)O/(Mg,Zn)O multiquantum wells / T. Makino, C. H. Chia, N. T. Tuan, Y. Segawa, M. Kawasaki, A. Ohtomo, K. Tamura, H. Koinuma // Appl. Phys. Lett. – 2000. – V. 77 – P. 1632-1634.
55. Ohtomo, A. $Mg_xZn_{1-x}O$ as a II–VI widegap semiconductor alloy / A. Ohtomo, M. Kawasaki, T. Koida, K. Masubuchi, H. Koinuma // Appl. Phys. Lett. – 1998. – V. 72 – P. 2466-2468.
56. Madelung, O. Semiconductors: Data Handbook / O. Madelung // third ed. New York: Springer. –2003.
57. Ryu, Y. R. Wide-band gap oxide alloy: BeZnO / Y. R. Ryu, T. S. Lee, J. A. Lubguban, A. B. Corman, H. W. White, J. H. Leem, M. S. Han, Y. S. Park, C. J. Youn, W. J. Kim // Appl. Phys. Lett. – 2006. – V. 88 – № 052103.
58. Ryu, Y. R. A technique of hybrid beam deposition for synthesis of ZnO and other metal oxides / Y. R. Ryu, T. S. Lee, H. W. White // J. Crystal Growth. – 2004. – V. 261 – P. 502-507.
59. Ryu, Y. R. Next generation of oxide photonic devices: ZnO-based ultraviolet light emitting diodes / Y. R. Ryu, T. S. Lee, J. A. Lubguban, H. W. White, B. J. Kim, Y. S. Park, C. J. Youn // Appl. Phys. Lett. – 2006. – V. 88 – № 241108.
60. Yu, J. H. Wide band-gap investigation of modulated BeZnO layers via photocurrent measurement / J. H. Yu, J. H. Kim, H. J. Yang, T. S. Kim, T. S. Jeong, C. J. Youn, K. J. Hong // J. Mater. Sci. – 2012. – V. 47 – P. 5529-5534.

61. Wang, Y. C. Comparative study of polar and non-polar BeZnO films grown by plasma-assisted molecular beam epitaxy / Y. C. Wang, T. Z. Wu, M. M. Chen, L. X. Su, Q. L. Zhang, Z. K. Tang // Chin. J. Luminesc. – 2013. – V. 34 – P. 1483-1488.
62. Kim, W. J. Crystalline properties of wide band gap BeZnO films / W. J. Kim, J. H. Leem, M. S. Han, I. W. Park, Y. R. Ryu, T. S. Lee // J. Appl. Phys. – 2006. – V. 99 – № 096104.
63. Khoshman, J. M. Vacuum ultra-violet spectroscopic ellipsometry study of sputtered BeZnO thin films / J. M. Khoshman, M. E. Kordesch // Optik. – 2011. – V. 122 – P. 2050-2054.
64. Jeong, T. S. Optical properties of BeZnO layers studied by photoluminescence spectroscopy / T. S. Jeong, M. S. Han, J. H. Kim, S. J. Bae, C. J. Youn // J. Phys. D Appl. Phys. – 2007. – V. 40 – № 370.
65. Khoshman, J. M. Bandgap engineering in amorphous Be_xZn_yO thin films / J. M. Khoshman, D. C. Ingram, M. E. Kordesch // Appl. Phys. Lett. – 2008. – V. 92 – № 091902.
66. Ding, S. F. Theoretical study of $Be_xZn_{1-x}O$ alloys / S. F. Ding, G. H. Fan, S. T. Li, K. Chen, B. Xiao // Phys. B. – 2007. – V. 394 – P. 127-131.
67. Fan, X. F. A direct first principles study on the structure and electronic properties of $Be_xZn_{1-x}O$ / X. F. Fan // Appl. Phys. Lett. – 2007. – V. 91 – № 121121.
68. Park, S. H. Internal field effects on electronic and optical properties of ZnO/BeZnO quantum well structures / S. H. Park, D. Ahn // Phys. B. – 2014. – V. 441 – P. 12-16.
69. Ganmukhi, R. Theoretical investigation of BeZnO-based UV LEDs / R. Ganmukhi, M. Calciati, M. Goano, E. Bellotti // Semicond. Sci. Technol. – 2012. – V. 27 – № 125015.
70. Duan, Y. Elasticity, band structure, and piezoelectricity of $Be_xZn_{1-x}O$ alloys / Y. Duan, H. Shi, L. Qin // Phys. Lett. A. – 2008. – V. 372 – P. 2930-2933.
71. Chen, M. Stabilization of BeZnO alloy by S incorporation: a density functional theory investigation / M. Chen, D. Yong, C. Wu, Z. Shen, A. Chen, Y. Zhu, B.

Pan, Z. Tang // J. Alloys Compd. – 2016. – V. 658 – P. 636-641.

72. Kong, F. T. Interstitial hydrogen in ZnO and BeZnO / F. T. Kong, H. J. Tao, H. R. Gong // Int. J. Hydrogen Energy. – 2013. – V. 38 – P. 5974-5982.
73. Teter, D. M. Low-Compressibility Carbon Nitrides, Science / D. M. Teter, R. J. Hemley // – 1996. – V. 271 – P. 53-55.
74. Liu, A. Y. Prediction of new low compressibility solids, Science / A. Y. Liu, M. L. Cohen // – 1989. – V. 245 – P. 841-842.
75. Kundoo, S. Synthesis of crystalline carbon nitride thin films by electrolysis of methanol-Urea solution / S. Kundoo, A. N. Banerjee // Mater. Lett. – 2002. – V. 57 – P. 2193-2197.
76. Yu, D. L. Synthesis of graphite-C_3N_4 crystal by ion beam sputtering / D. L. Yu, F. R. Xiao, T. S. Wang // J. Mater. Sci. Lett. – 2000. – V. 19 – P. 553-556.
77. Sharma, A. K. Synthesis of crystalline carbon nitride thin films by laser processing at a liquid-solid interface / A. K. Sharma, P. Ayyub, M. S. Multani // Appl. Phys. Lett. – 1996. – V. 69 – P. 3489-3491.
78. Niu, C. Experimental realization of the covalent solid carbon nitride / C. Niu, Y. Z. Lu, C. M. Lieber // Science. – 1993. – V. 261 – P. 334-337.
79. Montigaud, H. C_3N_4: Dream or reality? Solvothermal synthesis as macroscopic samples of the C_3N_4 graphitic form / H. Montigaud, B. Tanguy, G. Demazeau // J. Mater. Sci. – 2000. – V. 35 – P. 2547-2552.
80. Hu, C. C. Carbon Nitride (C_3N_4) Photocatalysts Synthesized from Different Methods for Photocatalytic Reaction Under Visible Light Irradiation / C. C. Hu, M. S. Wang, Z. W. Guo // ECS Trans. – 2016. – V. 72 – P. 9-14.
81. Yu, K. M. Observation of crystalline C_3N_4 / K. M. Yu, M. L. Cohen, E. E. Hailer, W. L. Hansen, A. Y. Liu, I. C. Wu // Phys. Rev. B. – 1994. – V. 49 – P. 5034-5037.
82. Cayuela, A. Semiconductor and carbon based fluorescent nanodots: The need for consistency / A. Cayuela, M. L. Soriano, C. Carrillo-Carrión, M. Valcarcel // Chem. Commun. – 2016. – V. 52 – P. 1311-1326.
83. Messina, F. Photoluminescence of carbon dots embedded in a SiO_2 matrix / F.

Messina, L. Sciortino, G. Buscarino, S. Agnello, F. Gelardi, M. Cannas // Mater. Today Proc. – 2016. – V. 3 – P. S258-S265.

84. Liu, S. Q. Highly photoluminescent nitrogen-rich carbon dots from melamine and citric acid for the selective detection of iron(III) ion / S. Q. Liu, R. L. Liu, X. Xing, C. Q. Yang, Y. Xua, D. Q. Wu // RSC Adv. – 2016. – V. 6 – P. 31884-31888.
85. Sciortino, L. Nitrogen-doped carbon dots embedded in a SiO_2 monolith for solid-state fluorescent detection of Cu^{2+} ions / L. Sciortino, F. Messina, G. Buscarino, S. Agnello, M. Cannas, F. M. Gelardi // J Nanopart. Res. – 2017. – V. 19 – № 228.
86. Messina, F. Fluorescent nitrogen-rich carbon nanodots with an unexpected β-C_3N_4 nanocrystalline structur / F. Messina, L. Sciortino, R. Popescu, A. M. Venezia, A. Sciortino, G. Buscarino, S. Agnello, R. Schneider, D. Gerthsen, // J. Mater. Chem. C. – 2016. – V. 4 – P. 2598-2605.
87. Sciortino, L. Tailoring the Emission Color of Carbon Dots Through Nitrogen-Induced Changes of Their Crystalline Structure / L. Sciortino, A. Sciortino, R. Popescu, R. Schneider, D. Gerthsen, S. Agnello, M. Cannas, F. Messina // J. Phys. Chem. C. – 2018. – V. 34 – P. 19897-19903.
88. Sciortino, A. β-C_3N_4 Nanocrystals: Carbon Dots with Extraordinary Morphological, Structural, and Optical Homogeneity / A. Sciortino, N. Mauro, G. Buscarino, L. Sciortino, R. Popescu, R. Schneider, G. Giammona, D. Gerthsen, M. Cannas, F. Messina // Chem. Mater. – 2018. – V. 30 – P. 1695-1700.
89. Faggio, G. Carbon Dots Dispersed on Graphene/SiO2/Si: A Morphological Study / G. Faggio, A. Gnisci, G. Messina, N. Lisi, A. Capasso, G.H. Lee, A. Armano, A. Sciortino, F. Messina, M. Cannas // Phys. Status Solidi A. – 2019. – V. 216 – № 1800559.
90. Fan, Q. Y. Two Novel C_3N_4 Phases: Structural, Mechanical and Electronic Properties / Q. Y. Fan, C. C. Chai, Q. Wei, Y. T. Yang // Materials. – 2016. – V. 9 – № 427.

91. Yao, H. Y. Optical properties of β-C_3N_4 and its pressure dependence / H. Y. Yao, W. Y. Ching // Phys. Rev. B. – 1994. – V. 50 – P. 11231-11234.

92. Xu, Y. Band gap of C_3N_4 in the GW approximation / Y. Xu, S. P. Gao // Int. J. Hydrogen Energy. – 2012. – V. 37 – P. 11072-11080.

93. Cohen, M. L. Structural, electronic and optical properties of carbon nitride / M. L. Cohen // Mat. Sci. Eng. A. – 1996. – V. 209 – P. 1-4.

94. Liu, A. Y. Structural properties and electronic structure of low-compressibility materials: Si_3N_4 and hypothetical C_3N_4 / A. Y. Liu, M. L. Cohen // Phys. Rev. B. – 1990. – V. 41 – P. 728-734.

95. Bonaccorso, F. Graphene photonics and optoelectronics / F. Bonaccorso, Z. Sun, T. Hasan, A. C. Ferrari // Nat. Photonics. – 2010. – V. 4 – P. 611-622.

96. Ahmadivand, A. Gated Graphene Enabled Tunable Charge–Current Configurations in Hybrid Plasmonic Metamaterials / A. Ahmadivand, B. Gerislioglu, G. T. Noe, Y. K. Mishra // ACS Appl. Electron. Mater. – 2019. – V. 1 – P. 637-641.

97. Fang, J. Enhanced Graphene Photodetector with Fractal Metasurface / J. Fang, D. Wang, C. T. DeVault, T. F. Chung, Y. P. Chen, A. Boltasseva, V. M. Shalaev, A.V. Kildishev // Nano Lett. – 2017. – V. 17 – P. 157-162.

98. Ahmadivand, B. Ramezani Gated graphene island-enabled tunable charge transfer plasmon terahertz metamodulator / B. Ahmadivand, Z. Gerislioglu // Nanoscale. – 2019. – V. 11 – P. 8091-8095.

99. Gerislioglu, B. Hybridized plasmons in graphene nanorings for extreme nonlinear optics / B. Gerislioglu, A. Ahmadivand, N. Pala // Opt. Mater. – 2017. – V. 73 – P. 729-735.

100. Segall, M. D. First-principles simulation: Ideas, illustrations and the CASTEP code / M. D. Segall, P. J. D. Lindan, M. J. Probert, C. J. Pickard, P. J. Hasnip, S. J. Clarkand, M. C. Payne // J. Phys. Condens. Matter. – 2002. – V. 14 – P. 2717-2744.

101. Xu, M. S. Graphene-Like Two-Dimensional Materials / M. S. Xu, T. Liang, M. M. Shi, H. Z. Chen // Chem. Rev. – 2013. – V. 113 – P. 3766-3798.

102. Balendhran, S. Elemental analogues of graphene: silicene, germanene, stanene, and phosphorene / S. Balendhran, S. Walia, H. Nili, S. Sriram, M. Bhaskaran // Small. – 2015. – V. 11 – P. 640-652.

103. Ferrari, A. C. Science and technology roadmap for graphene, related two-dimensional crystals, and hybrid systems / A. C. Ferrari, F. Bonaccorso, V. Fal'ko, K. S. Novoselov, S. Roche, P. Bøggild, S. Borini, F. H. Koppens, V. Palermo, N. Pugno // Nanoscale. – 2015. – V. 7 – P. 4598-4810.

104. Lay, G. L. Synthesis of Silicene / G. L. Lay, D. Solonenko, P. Vogt // Silicene. – 2018. – P. 99-113.

105. Tam, N. M. Fullerene-like boron clusters stabilized by an endohedrally doped iron atom: BnFe with n=14, 16, 18 and 20 / N. M. Tam, H. T. Pham, L. V. Duong, M. P. Pham-Ho, M. T. Nguyen // Phys. Chem. Chem. Phys. – 2015. – V. 17 – P. 3000-3003.

106. Huang, A. J. High intrinsic catalytic activity of boron nanotubes for hydrogen evolution reaction: an ab initio study / A. J. Huang, X. X. Chen, C. Y. Wang, Z. G. Wang // Mater. Res. Express. – 2019. – V. 6 – № 025036.

107. Wang, Z. Q. Review of borophene and its potential applications / Z. Q. Wang, T. Y. Lv, H. Q. Wang, Y. P. Feng, J. C. Zheng // Front. Phys. – 2019. – V. 14 – № 23403.

108. Mannix, A. J. Synthesis of borophenes: Anisotropic, two-dimensional boron polymorphs / A. J. Mannix, X. F. Zhou, B. Kiraly, J. D. Wood, D. Alducin, B. D. Myers, X. Liu, B. L. Fisher, U. Santiago, J. R. Guest // Science. – 2015. – V. 350 – P. 1513-1516.

109. Vogt, P. Silicene: Compelling Experimental Evidence for Graphenelike Two-Dimensional Silicon / P. Vogt, P. D. Padova, C. Quaresima, J. Avila, E. Frantzeskakis, M. C. Asensio, A. Resta, B. Ealet, G. L. Lay // Phys. Rev. Lett. – 2012. – V. 108 – № 155501.

110. Feng, B. Experimental realization of two-dimensional boron sheets / B. Feng, J. Zhang, Q. Zhong, W. Li, S. Li, H. Li, P. Cheng, S. Meng, L. Chen, K. Wu // Nat. Chem. – 2016. – V. 8 – P. 563-568.

111. Buscema, M. Photocurrent generation with two-dimensional van der Waals semiconductors / M. Buscema, J. O. Island, D. J. Groenendijk, S. I. Blanter, G. A. Steele, H. S. J. van der Zant, A. Castellanos-Gomez // Chem. Soc. Rev. – 2015. – V. 44 – P. 3691-3718.

112. Roldán, R. Strain engineering in semiconducting two-dimensional crystals / R. Roldán, A. Castellanos-Gomez, E. Cappelluti, F. Guinea // J. Phys.: Condens. Matter. – 2015. – V. 27 – № 313201.

113. Debbichi, L. Two-Dimensional Indium Selenides Compounds: An Ab Initio Study / L. Debbichi, O. Eriksson, S. Lebègue // J. Phys. Chem. Lett. – 2015. – V. 6 – P. 3098-3103.

114. Bandurin, D. A. High electron mobility, quantum Hall effect and anomalous optical response in atomically thin InSe / D. A. Bandurin, A. V. Tyurnina, G. L. Yu, A. Mishchenko, V. Zólyomi, S. V. Morozov, R. K. Kumar, R. V. Gorbachev, Z. R. Kudrynskyi, S. Pezzini, Z. D. Kovalyuk, U. Zeitler, K. S. Novoselov, A. Patanè, L. Eaves, I. V. Grigorieva, V. I. Fal'ko, A. K. Geim, Y. Cao // Nat. Nanotech. – 2017. – V. 12 – P. 223-227.

115. Miro, P. An atlas of two-dimensional materials / P. Miro, M. Audiffred, T. Heine // Chem. Soc. Rev. – 2014. – V. 43 – P. 6537-6554.

116. Bhimanapati, G. R. Recent Advances in Two-Dimensional Materials beyond Graphene / G. R. Bhimanapati, Z. Lin, V. Meunier, Y. Jung, J. Cha, S. Das, D. Xiao, Y. Son, M. S. Strano, V. R. Cooper // ACS Nano. – 2015. – V. 9 – P. 11509-11539.

117. Magorrian, S. J. Electronic and optical properties of two-dimensional InSe from a DFT-parametrized tight-binding model / S. J. Magorrian, V. Zolyomi, V. I. Fal’ko // Phys. Rev. B. – 2016. – V. 94 – № 245431.

118. Ho, C. H. Bending Photoluminescence and Surface Photovoltaic Effect on Multilayer InSe 2D Microplate Crystals / C. H. Ho, Y. J. Chu // Adv. Optical Mater. – 2015. – V. 3 – P. 1750 -1758.

119. Boukhvalov, D. W. The Advent of Indium Selenide: Synthesis, Electronic Properties, Ambient Stability and Applications / D. W. Boukhvalov, B.

Gürbulak, S. Duman, L. Wang, A. Politano, L. S. Caputi, G. Chiarello, A. Cupolillo // Nanomaterials. – 2017. – V. 7 – № 372.

120. Schedin, F. Detection of individual gas molecules adsorbed on graphene / F. Schedin, A. K. Geim, S. V. Morozov, E. W. Hill, P. Blake, M. I. Katsnelson, K. S. Novoselov // Nat. Mater. – 2007. – V. 6 – P. 652-655.

121. Leenaerts, O. Adsorption of H_2O, NH_3, CO, NO_2, and NO on graphene: A first-principles study / O. Leenaerts, B. Partoens, F. M. Peeters // Phys. Rev. B. – 2008. – V. 77 – № 125416.

122. Zhang, R. A First-Principles Study on Electron Donor and Acceptor Molecules Adsorbed on Phosphorene / R. Zhang, B. Li, J. Yang // J. Phys. Chem. C. – 2015. – V. 119 – P. 2871-2878.

123. Ma, D. W. The role of the intrinsic Se and In vacancies in the interaction of O_2 and H_2O molecules with the InSe monolayer / D. W. Ma, T. X. Li, D. Yuan, C. Z. He, Z. W. Lu, Z. S. Lu, Z. X. Yang, Y. X. Wang // Appl. Surf. Sci. – 2018. – V. 434 – P. 215-227.

124. Politano, A. The influence of chemical reactivity of surface defects on ambient-stable InSe-based nanodevices / A. Politano, G. Chiarello, R. Samnakay, G. Liu, B. Gurbulak, S. Duman, A. A. Balandin, D. W. Boukhvalov // Nanoscale. – 2016. – V. 8 – P. 8474-8479.

125. Stephens, P. J. Ab Initio Calculation of Vibrational Absorption and Circular Dichroism Spectra Using Density Functional Force Fields / P. J. Stephens, F. J. Devlin, C. F. Chabalowski, M. J. Frisch // J. Phys. Chem. – 1994. – V. 98 – P. 11623-11627.

126. Becke, A. D. Density- functional thermochemistry. III. The role of exact exchange // A. D. Becke // J. Chem. Phys. – 1993. – V. 98 – № 5648.

127. Parr, R. G Density-Functional Theory of Atoms and Molecules / R. G Parr, W. Yang // Oxford, New York. – 1989.

128. Koch, W. A Chemist’s Guide to Density Functional Theory / W. Koch, M. C. Holthausen // WILEYVCH. – 2001.

129. Born, M. Zur Quantentheorie der Molekeln / M. Born, R. Oppenheimer // Annalen der Physik. – 1927. – V. 389 – P. 457-484.

130. Slater, J. C. A simplification of the Hartree-Fock method / J. C. Slater // Phys. Rev. – 1951. – V. 81 – P. 538-390.

131. Hohenberg, P. Inhomogeneous Electron Gas / P. Hohenberg, W. Kohn // Phys. Rev. – 1964. – V. 136 – P. B864-B871.

132. Kohn, W. Self Consistent Equations Including Exchange and Correlation Effects / W. Kohn, L. J. Sham // Phys. Rev. – 1965. – V. 140 – P. A1133-A1138.

133. Koopmans, Über die Zuordnung von Wellenfunktionen und Eigenwerten zu den einzelnen Elektronen eines Atoms / Koopmans, Tjalling // Physica. Elsevier. – 1934. – V. 1 – P. 104-113.

134. Jones, R. O. The density functional formalism, its applications and prospects / R. O. Jones, O. Gunnarsson // Rev. Mod. Phys. – 1989. – V. 61 – P. 689-746.

135. Perdew, J. P. Self-interaction correction to density-functional approximations for many-electron systems / J. P. Perdew, A. Zunger // Phys. Rev. B. – 1981. – V. 23 – P. 5048-5079.

136. Troullier, N. Efficient pseudopotentials for plane-wave calculations / N. Troullier, José Luís Martins // Phys. Rev. B. – 1991. – V. 43 – P. 1993-2006.

137. Adachi, S. Properties of Semiconductor Alloys: Group-IV, III-V and II-VI Semiconductors / S. Adachi // Wiley, Chichester. – 2009.

138. Stone, A. J. Theory of Intermolecular Forces Clarendon / A. J. Stone // Oxford. – 1996.

139. Allen, M. J. Helium dimer dispersion forces and correlation potentials in density functional theory / M. J. Allen, D. J. Tozer // J. Chem. Phys. – 2001. – V. 117 – P. 11113-11120.

140. Grimme, S. Accurate Description of van der Waals Complexes by Density Functional Theory Including Empirical Corrections / S. Grimme // J. Comput. Chem. – 2004. – V. 25 – P. 463-1473.

141. Grimme, S. Density functional theory with dispersion corrections for supramolecular structures, aggregates, and complexes of (bio)organic molecules

/ S. Grimme, J. Antony, T. Schwabe, C. Muck-Lichtenfeld // Org. Biomol. Chem. – 2007. – V. 5 – P. 741-758.

142. Perdew, J. P. Generalized gradient approximation made simple / J. P. Perdew, K. Burke, M. Ernzerhof // Phys. Rev. Lett. – 1996. – V. 77 – P. 3865-3868.

143. Monkhorst, H. J. Special points for brillouin-zone integrations / H. J. Monkhorst, J. D. Pack // Phys. Rev. B. – 1976. – V. 13 – P. 5188-5192.

144. Harrison, W. A. Electronic Structure and the Properties of Solids / W. A. Harrison // Dover Pub. New York. – 1989.

145. Pearton, S. J. Recent progress in processing and properties of ZnO / S. J. Pearton, D. P. Norton, K. Ip, Y. W. Heo, T. Steiner // Prog. Mater. Sci. – 2005. – V. 50 – P. 293-340.

146. Khoshman, J. M. Bandgap engineering in amorphous Be_xZn_yO thin films / J. M. Khoshman, D. C. Ingram, M. E. Kordesch // Appl. Phys. Lett. – 2008. – V. 92 – № 091902.

147. Zheng, Y. P. Influence of Be-Doping on Electronic Structure and Optical Properties of ZnO / Y. P. Zheng, Z. G. Chen, Y. Lu // J. Semiconductors. – 2008. – V. 29 – P. 2317-2321.

148. Vegard, L. Vegard’s law: a fundamental relation or an Approximation / L. Vegard // Z. Phys. – 1921. – V. 5 – P. 17-26.

149. Tang, X. Study on the doping stability and electronic structure of wurtzite $Zn_{1-x}Cd_xO$ alloys by first-principle calculations / X. Tang, H. F. Lu, J. J. Zhao, Q. Y. Zhang // Phys. Chem. Solids. – 2010. – V. 71 – P. 336-339.

150. Adachi, S. Properties of Semiconductor Alloys: Group-IV, III-V and II-VI Semiconductors / S. Adachi // – 2009.

151. Kim, D. Y. Ferromagnetism induced by Zn vacancy defect and lattice distortion in ZnO / D. Y. Kim, J. H. Yang, J. S. Hong // J. Appl. Phys. – 2009. – V. 106 – № 013908.

152. Stelmakh, S. Effect of interaction of external surfaces on the symmetry and lattice distortion of CdSe nanocrystals by molecular dynamics simulations / S. Stelmakh, K. Skrobas, S. Gierlotka, B. Palosz // J. Nanopart. Res. – 2017. – V.

19 – № 391.

153. Stelmakh, S. Effect of the surface on the internal structure of CdSe crystal lattice based on molecular dynamics simulations / S. Stelmakh, K. Skrobas, S. Gierlotka, B. Palosz // J. Nanopart. Res. – 2017. – V. 19 – № 170.

154. Qin, W. Lattice distortion and its effects on physical properties of nanostructured materials / W. Qin, T. Nagase, Y. Umakoshi, J. A. Szpunar // J. Phys.: Condens. Matter. – 2007. – V. 19 – № 236217.

155. Sciortino, L. Tailoring the Emission Color of Carbon Dots Through Nitrogen-Induced Changes of Their Crystalline Structure / L. Sciortino, A. Sciortino, R. Popescu, R. Schneider, D. Gerthsen, S. Agnello, M. Cannas, F. Messina // J. Phys. Chem. C. – 2018. – V. 34 – P. 19897-19903.

156. Sciortino, A. β-C_3N_4 Nanocrystals: Carbon Dots with Extraordinary Morphological, Structural, and Optical Homogeneity / A. Sciortino, N. Mauro, G. Buscarino, L. Sciortino, R. Popescu, R. Schneider, G. Giammona, D. Gerthsen, M. Cannas, F. Messina // Chem. Mater. – 2018. – V. 30 – P. 1695-1700.

157. Bao, L. Photoluminescence-Tunable Carbon Nanodots: Surface-State Energy-Gap Tuning / L. Bao, C. Liu, Z. L. Zhang, D. W. Pang // Adv. Mater. – 2015. – V. 27 – P. 1663-1667.

158. Faggio, G. Carbon Dots Dispersed on Graphene/SiO_2/Si: A Morphological Study / G. Faggio, A. Gnisci, G. Messina, N. Lisi, A. Capasso, G. H. Lee, A. Armano, A. Sciortino, F. Messina, M. Cannas // Phys. Status Solidi A. – 2019. – V. 216 – № 1800559.

159. Ahmadivand, B. Ramezani Gated graphene island-enabled tunable charge transfer plasmon terahertz metamodulator / B. Ahmadivand, Z. Gerislioglu // Nanoscale. – 2019. – V. 11 – P. 8091-8095.

160. Piazza, Z. A. Planar hexagonal B(36) as a potential basis for extended single-atom layer boron sheets / Z. A. Piazza, H. Hu, W. L. Li, Y. F. Zhao, J. Li, L. S. Wang // Nat Commun. – 2014. – V. 5 – № 3113.

161. Li, W. B. Experimental realization of honeycomb borophene / W. B. Li, L. J.

Kong, C. Y. Chen, J. Gou, S. X. Sheng, W. F. Zhang, H. Li, L. Chen, P. Cheng, K. H. Wu // Sci. Bull. – 2018. – V. 63 – P. 282-286.

162. Feng, B. Experimental realization of two-dimensional boron sheets / B. Feng, J. Zhang, Q. Zhong, W. Li, S. Li, H. Li, P. Cheng, S. Meng, L. Chen, K. Wu // Nat. Chem. – 2016. – V. 8 – P. 563-568.

163. Gonzalez, S. N. B80 fullerene: An ab initio prediction of geometry, stability, and electronic structure / S. N. Gonzalez, A. Sadrzadeh, B. Yakobson // Phys. Rev. Lett. – 2007. – V. 98 – № 166804.

164. Zhao, J. J. B_{80} and other medium-sized boron clusters: Core-shell structures, not hollow cages / J. J. Zhao, L. Wang, F. Y. Li, Z. F. Chen // J. Phys. Chem. A. – 2010. – V. 114 – P. 9969-9972.

165. Li, F. B_{80} and B101-103 clusters: Remarkable stability of the core-shell structures established by validated density functionals / F. Li, P. Jin, D. E. Jiang, L. Wang, S. B. Zhang, J. Zhao, Z. Chen // J. Chem. Phys. – 2012. – V. 136 – № 074302.

166. Li, H. Icosahedral B12-containing core-shell structures of B80 / H. Li, N. Shao, B. Shang, L. F. Yuan, J. L. Yang, X. C. Zeng // Chem. Commun. – 2010. – V. 46 – P. 3878-3880.

167. De, S. Energy landscape of fullerene materials: A comparison of boron to boron nitride and carbon / S. De, A. Willand, M. Amsler, P. Pochet, L. Genovese, S. Goedecker // Phys. Rev. Lett. – 2011. – V. 106 – № 225502.

168. Peng, B. The electronic, optical, and thermodynamic properties of borophene from first-principles calculations / B. Peng, H. Zhang, H. Z. Shao, Y. F. Xu, R. J. Zhang, H. Y. Zhu // J. Mater. Chem. C. – 2016. – V. 4 – P. 3592-3598.

169. Xiao, R. C. Enhanced superconductivity by strain and carrier-doping in borophene: A first principles prediction / R. C. Xiao, D. F. Shao, W. J. Lu, H. Y. Lv, J. Y. Li, Y. P. Sun // Appl. Phys. Lett. – 2016. – V. 109 – № 122604.

170. Liu, Y. X. Stable and metallic borophene nanoribbons from first-principles calculations / Y. X. Liu, Y. J. Dong, Z. Y. Tang, X. F. Wang, L. Wang, T. J. Hou, H. P. Lin, Y. Y. Li // J. Mater. Chem. C. – 2016. – V. 4 – P. 6380-6385.

171. Zhang, X. M. Borophene as an extremely high capacity electrode material for Li-ion and Na-ion batteries / X. M. Zhang, J. P. Hu, Y. C. Cheng, H. Y. Yang, Y. G.Yao, S. Y. A. Yang // Nanoscale. – 2016. – V. 8 – P. 15340-15347.

172. Wang, V. Lattice Defects and the Mechanical Anisotropy of Borophene / V. Wang, W. T. Geng // J. Phys. Chem. C. – 2017. – V. 121 – P. 10224-10232.

173. Cui, H. Borophene: a promising adsorbent material with strong ability and capacity for SO_2 adsorption / H. Cui, X. X. Zhang, D. C. Chen // Appl. Phys. A. – 2018. – V. 124 – № 636.

174. Zhong, H. X. Electronic and mechanical properties of few-layer borophene / H. X. Zhong, K. X. Huang, G. D. Yu, S. J. Yuan // Phys. Rev. B. – 2018. – V. 98 – № 054104.

175. Tang, X. Atomically thin NiB6 monolayer: a robust Dirac material / X. Tang, W. G. Sun, C. Lu, L. Z. Kou, C. F. Chen // Phys. Chem. Chem. Phys. – 2019. – V. 21 – P. 617-622.

176. Tang, H. Novel precursors for boron nanotubes: The competition of two-center and three-center bonding in boron sheets / H. Tang, S. Ismail-Beigi // Phys. Rev. Lett. – 2007. – V. 99 – № 115501.

177. Tang, H. Self-doping in boron sheets from first principles: A route to structural design of metal boride nanostructures / H. Tang, S. Ismail-Beigi // Phys. Rev. B. – 2009. – V. 80 – № 134113.

178. Yang, X. B. Ab initio prediction of stable boron sheets and boron nanotubes: Structure, stability, and electronic properties / X. B. Yang, Y. Ding, J. Ni // Phys. Rev. B. – 2008. – V. 77 – № 041402.

179. Kunstmann, J. Broad boron sheets and boron nanotubes: An ab initio study of structural, electronic, and mechanical properties / J. Kunstmann, A. Quandt // Phys. Rev. B. – 2006. – V. 74 – № 035413.

180. Cabria, I. Buckling in boron sheets and nanotubes / I. Cabria, J. A. Alonso, M. J. López // Phys. Status Solidi A. – 2006. – V. 203 – P. 1105-1110.

181. Lau, K. C. First-principles study of the stability and electronic properties of sheets and nanotubes of elemental boron / K. C. Lau, R. Pati, R. Pandey, A. C.

Pineda // Chem. Phys. Lett. – 2006. – V. 418 – P. 549-554.

182. Lau, K. C. Stability and electronic properties of atomistically-engineered 2D boron sheets / K. C. Lau, R. Pandey // J. Phys. Chem. C. – 2007. – V. 111 – P. 2906-2912.

183. Galeev, T. R. Deciphering the mystery of hexagon holes in an all-boron graphene alpha-sheet / T. R. Galeev, Q. Chen, J. C. Guo, H. Bai, C. Q. Miao, H. G. Lu, A. P. Sergeeva, S. D. Li, A. I. Boldyrev // Phys. Chem. Chem. Phys. – 2011. – V. 13 – P. 11575-11578.

184. Zope, R. R. Snub boron nanostructures: Chiral fullerenes, nanotubes and planar sheet / R. R. Zope, T. Baruah // Chem. Phys. Lett. – 2011. – V. 501 – P. 193-196.

185. Penev, E. S. Polymorphism of two-dimensional boron / E. S. Penev, S. Bhowmick, A. Sadrzadeh, B. I. Yakobson // Nano Lett. – 2012. – V. 12 – P. 2441-2445.

186. Yu, X. Prediction of two-dimensional boron sheets by particle swarm optimization algorithm / X. Yu, L. Li, X. Xu, C. Tang // J. Phys. Chem. C. – 2012. – V. 116 – P. 20075-20079.

187. Wu, X. Two-dimensional boron monolayer sheets / X. Wu, J. Dai, Y. Zhao, Z. Zhuo, J. Yang, X. C. Zeng // ACS Nano. – 2012. – V. 6 – P. 7443-7453.

188. Ciuparu, D. Synthesis of pure boron single-wall nanotubes / D. Ciuparu, R. F. Klie, Y. Zhu, L. Pfefferle // J. Phys. Chem. B – 2004. – V. 108 – P. 3967-3969.

189. Liu, F. Metal-like single crystalline boron nanotubes: Synthesis and in situ study on electric transport and field emission properties / F. Liu, C. M. Shen, Z. J. Su, X. L. Ding, S Z. Deng, J. Chen, N. S. Xu, H. J. Gao // J. Mater. Chem. – 2010. – V. 20 – P. 2197-2205.

190. Aufray, B. Graphene-like silicon nanoribbons on ag(110): A possible formation of silicone / B. Aufray, A. Kara, S. Vizzini, H. Oughaddou, C. Leandri, B. Ealet, G. L. Lay // Appl. Phys. Lett. – 2010. – V. 96 – № 183102.

191. Feng, B. J. Evidence of silicene in honeycomb structures of silicon on Ag(111) / B. J. Feng, Z. J. Ding, S. Meng, Y. G. Yao, X. Y. He, P. Cheng, L.

Chen, K. H. Wu // Nano Lett. – 2012. – V. 12 – P. 3507-3511.

192. Vogt, P. Silicene: Compelling experimental evidence for graphenelike two-dimensional silicon / P. Vogt, P. D. Padova, C. Quaresima, J. Avila, E. Frantzeskakis // Phys. Rev. Lett. – 2012. – V. 108 – № 155501.

193. Meng, L. Buckled silicene formation on Ir(111) / L. Meng, Y. L. Wang, L. Z. Zhang, S. X. Du, R. T. Wu, L. F. Li, Y. Zhang, G. Li, H. T. Zhou, W. A. Hofer, H. J. Gao // Nano Lett. – 2013. – V. 13 – P. 685-690.

194. Zhai, H. J. Hydrocarbon analogues of boron clusters-planarity, aromaticity and antiaromaticity / H. J. Zhai, B. Kiran, J. Li, L. S. Wang // Nat. Mater. – 2003. – V. 2 – P. 827-833.

195. Kiran, B. Planar-to-tubular structural transition in boron clusters: B20 as the embryo of single-walled boron nanotubes / B. Kiran, S. Bulusu, H. J. Zhai, S. Yoo, X. C. Zeng, L. S. Wang // Proc. Natl. Acad. Sci. – 2005. – V. 102 – P. 961-964.

196. Alexandrova, A. N. All-boron aromatic clusters as potential new inorganic ligands and building blocks in chemistry / A. N. Alexandrova, A. I. Boldyrev, H. J. Zhai, L. S. Wang // Coord. Chem. Rev. – 2006. – V. 250 – P. 2811-2866.

197. Romanescu, C. Probing the structures of neutral boron clusters using infrared/vacuum ultraviolet two color ionization: B11, B16, and B17 / C. Romanescu, D. J. Harding, A. Fielicke, L. S. Wang // J. Chem. Phys. – 2012. – V. 137 – № 014317.

198. Piazza, Z. A. A photoelectron spectroscopy and ab initio study of B21−: Negatively charged boron clusters continue to be planar at 21 / Z. A. Piazza, W. L. Li, C. Romanescu, A. P. Sergeeva, L. S. Wang, A. I. Boldyrev // J. Chem. Phys. – 2012. – V. 136 – № 104310.

199. Sergeeva, A. P. B22- and B23-: All-boron analogues of anthracene and phenanthrene / A. P. Sergeeva, Z. A. Piazza, C. Romanescu, W. L. Li, A. L. Boldyrev, L. S. Wang // J. Am. Chem. Soc. – 2012. – V. 134 – P. 18065-18073.

200. Popok, V. N. Cluster-surface interaction: From soft landing to implantation / V. N. Popok, I. Barke, E. E. B. Campbell, K. H. Meiwes-Broer // Surf. Sci. Rep.

– 2011. – V. 66 – P. 347-377.

201. Boukhvalov, D. W. Chemical modifications and stability of phosphorene with impurities: a first principles study / D. W. Boukhvalov, A. N. Rudenko, D. A. Prishchenko, V. G. Mazurenko, M. I. Katsnelson // Phys. Chem. Chem. Phys. – 2015. – V. 17 – P. 15209-15217.

202. Politano, A. The role of surface chemical reactivity in the stability of electronic nanodevices based on two-dimensional materials "beyond graphene" and topological insulators / A. Politano, M. S. Vitiello, L. Viti, D. W. Boukhvalov, G. Chiarello // FlatChem. – 2017. – V. 1 – P. 60-64.

203. D'Olimpio, G. PdTe2 transition-metal dichalcogenide: chemical reactivity, thermal stability and device implementation / G. D'Olimpio, C. Guo, C. N. Kuo, R. Edla, C. S. Lue, L. Ottaviano, P. Torelli, L. Wang, D. W. Boukhvalov, A. Politano // Adv. Funct. Mat. – 2020. – V. 30 – № 1906556.

204. Boukhvalov, D. W. Oxygen reduction reactions on pure and nitrogen-doped graphene: a first principles modeling / D. W. Boukhvalov, Y. W. Son // Nanoscale. – 2012. – V. 4 – P. 417-419.

205. Cai, Y. Electronic Properties of Phosphorene/Graphene and Phosphorene/Hexagonal Boron Nitride Heterostructures / Y. Cai, G. Zhang, Y. W. Zhang // J. Phys. Chem. C. – 2015. – V. 119 – P. 13929-13936.

206. Boukhvalov, D. W. Chemical functionalization of graphene / D. W. Boukhvalov, M. I. Katsnelson // J. Phys.: Condens. Matter. – 2009. – V. 21 – № 344205.

207. Boukhvalov, D. W. Defect-induced ferromagnetism in fullerenes / D. W. Boukhvalov, M. I. Katsnelson // Eur. Phys. J. B. – 2009. – V. 68 – P. 529-535.

208. Zatsepin, D. A. Electronic structure, charge transfer, and intrinsic luminescence of gadolinium oxide nanoparticles: Experiment and theory / D. A. Zatsepin, D. W. Boukhvalov, A. F. Zatsepin, Yu. A. Kuznetsova, M. A. Mashkovtsev, V. N. Rychkov, V. Ya. Shur, A. A. Esin, E. Z. Kurmaev // Appl. Surf. Sci. – 2018. – V. 436 – P. 697-707.

209. Hu, S. Proton transport through one atom thick crystal / S. Hu, M. Lozada-

Hidaldo, F. C. Wang, A. Mischenko, F. Schedin, R. R. Nair, E. W. Hill, D. W. Boukhvalov, M. I. Katsnelson, R. A. W. Dryfe, I. V. Grigorieva, H. A. Wu, A. K. Geim // Nature. – 2014. – V. 561 – P. 227-230.

210. Hasan, M. Z. Topological insulators / M. Z. Hasan, C. L. Kane // Rev. Mod. Phys. – 2010. – V. 82 – P. 3045-3067.

211. Qi, X. L. Topological insulators and superconductors / X. L. Qi, S. C. Zhang // Rev. Mod. Phys. – 2011. – V. 83 – P. 1057-1110.

212. Ren, Y. F. Topological phases in two-dimensional materials: a review / Y. F. Ren, Z. H. Qiao, Q. Niu // Rep. Prog. Phys. – 2016. – V. 79 – № 066501.

213. Lee, H. S. MoS_2 Nanosheet Phototransistors with Thickness-Modulated Optical Energy Gap / H. S. Lee, S. W. Min, Y. G. Chang, M. K. Park, T. Nam, H. Kim, J. H. Kim, S. Ryu, S. Im // Nano Lett. – 2012. – V. 12 – P. 3695-3700.

214. Castro Neto, A. H. The electronic properties of graphene / A. H. Castro Neto, F. Guinea, N. M. R. Peres, K. S. Novoselov, A. K. Geim // Rev. Mod. Phys. – 2009. – V. 81 – P. 109-162.

215. Li, L. Direct observation of the layer-dependent electronic structure in phosphorene / L. Li, J. Kim, C. Jin, G. J. Ye, D. Y. Qiu, F. H. da Jornada, Z. Shi, L. Chen, Z. Zhang, F. Yang, K. Watanabe, T. Taniguchi, W. Ren, S.G. Louie, X. H. Chen, Y. Zhang, F. Wang // Nat. Nanotech. – 2017. – V. 12 – P. 21-25.

216. Lightcap, I. V. Graphitic Design: Prospects of Graphene-Based Nanocomposites for Solar Energy Conversion, Storage, and Sensing / I. V. Lightcap, P. V. Kamat // Acc. Chem. Res. – 2013. – V. 46 – P. 2235-2243.

217. Varghese, S. Two-Dimensional Materials for Sensing: Graphene and Beyond / S. Varghese, S. Swaminathan, K. Singh, V. Mittal // Electron. – 2015. – V. 4 – P. 651-687.

218. Yang, W. Two-dimensional layered nanomaterials for gas-sensing applications / W. Yang, L. Gan, H. Li, T. Zhai // Inorg. Chem. Front. – 2016. – V. 3 – P. 433-451.

219. Mudd, G. W. The direct-to-indirect band gap crossover in two-dimensional van der Waals Indium Selenide crystals / G. W. Mudd, M. R. Molas, X. Chen, V.

Zólyomi, K. Nogajewski, Z. R. Kudrynskyi, Z. D. Kovalyuk, G. Yusa, O. Makarovsky, L. Eaves, M. Potemski, V. I. Fal’ko and A. Patanè // Sci. Rep. – 2016. – V. 6 – № 39619.

220. Sánchez-Royo, J. F. Electronic structure, optical properties, and lattice dynamics in atomically thin indium selenide flakes / J. F. Sánchez-Royo, G. Muñoz-Matutano, M. Brotons-Gisbert, J. P. Martínez-Pastor, A. Segura, A. Cantarero, R. Mata, J. Canet-Ferrer, G. Tobias, E. Canadell // Nano Res. – 2014. – V. 7 – P. 1556-1568.

221. Niu, X. H. Highly effifffifficient photogenerated electron transfer at a black phosphorus/indium selenide heterostructure interface from ultrafast dynamics / X. H. Niu, Y. H. Li, Y. H. Zhang, Q. J. Zheng, J. Zhao, J. L. Wang // J. Mater. Chem. C. – 2019. – V. 7 – P. 1864-1870.

222. Kistanov, A. A. Atomic-scale mechanisms of defect- and light-induced oxidation and degradation of InSe / A. A. Kistanov, Y. Q. Cai, K. Zhou, S. V. Dmitrievc, Y. W. Zhang // J. Mater. Chem. C. – 2018. – V. 6 – P. 518-525.

223. Cai, Y. Q. Charge Transfer and Functionalization of Monolayer InSe by Physisorption of Small Molecules for Gas Sensing / Y. Q. Cai, G. Zhang, Y. W. Zhang // J. Phys. Chem. C, – 2017. – V. 121 – P. 10182-10193.

224. Feng, W. Back Gated Multilayer InSe Transistors with Enhanced Carrier Mobilities via the Suppression of Carrier Scattering from a Dielectric Interface / W. Feng, W. Zheng, W. Cao, P. Hu // Adv. Mater. – 2014. – V. 26 – P. 6587-6593.

225. Sucharitakul, S. Intrinsic Electron Mobility Exceeding 103 cm2/(V s) in Multilayer InSe FETs / S. Sucharitakul, N. J. Goble, U. R. Kumar, R. Sankar, Z. A. Bogorad, F. C. Chou, Y. T. Chen, X. P. A. Gao // Nano Lett. – 2015. – V. 15 – P. 3815-3819.

226. Brotons-Gisbert, M. Nanotexturing to Enhance Photoluminescent Response of Atomically Thin Indium Selenide with Highly Tunable Band Gap / M. Brotons-Gisbert, D. Andres-Penares, J. Suh, F. Hidalgo, R. Abargues, P. J. Rodríguez-Cantó, A. Segura, A. Cros, G. Tobias, E. Canadell, P. Ordejón, J. Wu,

J. P. Martínez-Pastor, J. F. Sánchez-Royo // Nano Lett. – 2016. – V. 16 – P. 3221-3229.

227. Zólyomi, V. Electrons and phonons in single layers of hexagonal indium chalcogenides from ab initio calculations / V. Zólyomi, N. D. Drummond, V. I. Fal'ko // Phys. Rev. B. – 2014. – V. 89 – № 205416.

228. Mudd, G. W. High Broad-Band Photoresponsivity of Mechanically Formed InSe-Graphene van der Waals Heterostructures / G. W. Mudd, S. A. Svatek, L. Hague, O. Makarovsky, Z. R. Kudrynskyi, C. J. Mellor, P. H. Beton, L. Eaves, K. S. Novoselov, Z. D. Kovalyuk, E. E. Vdovin, A. J. Marsden, N. R. Wilson, A. Patanè // Adv. Mater. – 2015. – V. 27 – P. 3760-3766.

229. Lei, S. Evolution of the Electronic Band Structure and Efficient Photo-Detection in Atomic Layers of InSe / S. Lei, L. Ge, S. Najmaei, A. George, R. Kappera, J. Lou, M. Chhowalla, H. Yamaguchi, G. Gupta, R. Vajtai, A. D. Mohite, P. M. Ajayan // ACS Nano. – 2014. – V. 8 – P. 1263-1272.

230. Lembke, D. Single-Layer MoS2 Electronics / D. Lembke, S. Bertolazzi, A. Kis // Acc. Chem. Res. – 2015. – V. 48 – P. 100-110.

231. Novoselov, K. S. A roadmap for graphene / K. S. Novoselov, V. I. Falko, L. Colombo, P. R. Gellert, M. G. Schwab, K. Kim // Nature. – 2012. – V. 490 – P. 192-200.

232. Tian, W. C. Research Progress of Gas Sensor Based on Graphene and Its Derivatives: A Review/ W. C. Tian, X. H. Liu, W. B.Yu // Appl. Sci. – 2018. – V. 8 – № 1118.

233. Yang, M. Gas Sensors Based on Chemically Reduced Holey Graphene Oxide Thin Films / M. Yang, Y. Y. Wang, L. Dong, Z. Y. Xu, Y. H. Liu, N. T. Hu, W. S. W. Kong, J. Zhao, C. S. Peng // Nanoscale Res Lett. – 2019. – V. 14 – № 218.

234. Kou, L. Z. Phosphorene as a Superior Gas Sensor: Selective Adsorption and Distinct I−V Response / L. Z. Kou, T. Frauenheim, C. F. Chen // J. Phys. Chem. Lett. – 2014. – V. 5 – P. 2675-2681.

235. Ma, D. W. First-principles study of the small molecule adsorption on the InSe monolayer / D. W. Ma, W. W. Ju, Y. N. Tang, Y. Yue // Appl. Surf. Sci. – 2017. –

V. 426 – P. 244-252.

236. Shi, L. Oxidation mechanism and protection strategy of ultrathin Indium Selenide: Insight from Theory / L. Shi, Q. Zhou, Y. Zhao, Y. Ouyang, C. Ling, Q. Li, J. Wang // J. Phys. Chem. Lett. – 2017. – V. 8 – P. 4368-4373.

237. Petroni, E. Liquid-phase exfoliated indium-selenide flakes as suitable catalysts for hydrogen evolution reaction / E. Petroni, E. Lago, S. Bellani, D. W. Boukhvalov, A. Politano, B. Gürbulak, S. Duman, M. Prato, S. Gentiluomo, R. Oropeza-Nuñez, J. K. Panda, P. S. Toth, A. E. Del Rio Castillo, V. Pellegrini, F. Bonaccorso // Small. – 2018. – V. 14 – № 1800749.

238. Fasolino, A. Intrinsic ripples in graphene / A. Fasolino, J. H. Los, M. I. Katsnelson // Nat. Mater. – 2007. – V. 6 – P. 858-861.

239. Boukhvalov, D.W. Tuneable molecular doping of corrugated graphene / D.W. Boukhvalov // Surf. Sci. – 2010. – V. 604 – P. 2190-2193.